Studies of Pyrite FeS_2 Nanocrystals and Plasmonic Nanostructures for Low Cost and High Efficiency Inverted Bulk Heterojunction Photovoltaic Cells

Beau J. Richardson

A dissertation submitted in partial fulfillment of the

requirements for the degree of

Doctor of Philosophy

University of Washington

2015

Reading Committee:

Qiuming Yu, Chair

Samson A. Jenekhe

Christine K. Luscombe

Karl F. Böhringer

Program Authorized to Offer Degree:

Department of Chemical Engineering

University of Washington

Abstract

Studies of Pyrite FeS_2 Nanocrystals and Plasmonic Nanostructures for Low Cost and High Efficiency Inverted Bulk Heterojunction Photovoltaic Cells

Beau Richardson

Chair of the Supervisory Committee:
Prof. Qiuming Yu
Department of Chemical Engineering

Solar energy is our most abundant and clean natural energy source which has made photovoltaics (PV) of great interest as a renewable and sustainable energy technology. Organic photovoltaics (OPVs) offer great potential for lower fabrication and materials costs as they are solution processable, compatible with high throughput roll-to-roll printing processes, flexible, lightweight and have tunable material properties. The encompassing goal of this work is to explore new materials, nanostructures and device designs that may aid the development of OPVs towards large scale, low cost and more efficient PV technologies.

In the search for new PV materials, pyrite iron disulfide (FeS_2) is noticeable as an earth abundant and environmentally benign semiconductor with low procurement costs and advantageous optoelectronic properties. Here, pyrite FeS_2 nanocrystals (NCs) were synthesized and deployed in ternary organic-inorganic hybrid bulk-heterojunction (BHJ) solar cells with an inverted architecture. Three device performance regimes are observed when the pyrite NC concentration is varied from 0 to 4 wt% that appear linked to microstructure transitions in the

active layer. The addition of FeS_2 NCs consistently increased photocurrent and exposure in air actually rectified current leakage resulting in an average 28% increase in power conversion efficiency (PCE) of hybrid devices compared to control devices. The photocurrent enhancement and air-stability demonstrated by this inverted design offer a promising architecture for future pyrite FeS_2 NC-based devices. Furthermore, the NC characterizations presented here provide insight to advance pyrite's development as a PV material.

Nanostructures of various types can be used to enhance OPV performance. The effects of nanostructured ZnO electron transport layers (ETLs) were studied in high efficiency inverted OPVs on ITO substrates. Nano-ridged and planar ZnO ETLs were formed and consistently high FFs exceeding 70% and PCEs reaching 8.32% were achieved on both types of nanostructures when maintaining optimal active layer thickness. ITO is the most common transparent electrode used in OPVs, yet limited indium reserves and poor mechanical properties of ITO on flexible substrates make it non-ideal for large-scale OPV production. To replace ITO, plasmonic nanostructured electrodes were designed, fabricated and deployed as electrodes in inverted OPV devices. ZnO thickness was found to significantly impact active layer absorption due to resonant cavity effects with the plasmonic nanostructured electrodes. Devices with thinner ZnO ETLs showed PCEs as high as 5.70% and higher J_{SC}'s than devices on thicker ZnO. ITO-free, flexible devices on PET showed a PCE of 1.82% and those fabricated on ultrathin and conformable Parylene substrates yielded an initial PCE over 1%. To our knowledge, this is the first time nanopatterned plasmonic electrodes have been applied to highly flexible, ITO-free OPVs. With further fabrication development to improve nanopattern quality on flexible substrates, these designs show promise for highly functioning conformable devices that can be applied to numerous needs for lightweight, ubiquitous power generation.

TABLE OF CONTENTS

LIST OF FIGURES

LIST OF TABLES

ACKNOWLEDGEMENTS

I am truly grateful to Professor Qiuming Yu, my PhD advisor, for all of the guidance, support and encouragement that she has provided throughout my graduate studies. I am thankful to have had the opportunity to work in her research group on interesting projects and for all of the knowledge she has shared and learning she has inspired. I also appreciate the positive and supportive group culture that she has created which added to my fulfillment and enjoyment through this experience.

I would like to thank Professors Samson A. Jenekhe, Christine Luscombe and Karl F. Böhringer for giving their time to serve on my supervisory committee and for the valuable comments, suggestions and feedback they have provided. I would also like to thank Professors Samson Jenekhe, Shaoyi Jiang, Alex Jen, Lilo Pozzo and their research groups for providing access to and training for several pieces of equipment that were crucial to the success of various experiments.

I am also very grateful for the friendship, comradery, support and teamwork of all current and past Yu Group members who have made this experience all the better. These include Leize Zhu, David Galvan, Monica Esopi, Yu-Han Ho, Fang Sun, John Bae, Abdulrahman Almutairi, Xuezhen Wang, Daqian Wang, Max Calcagno, Kevin Fu, Nadia Lucas and the rest of our group.

I also would like to acknowledge the Department of Chemical Engineering at UW, UW CoMotion, the American Chemical Society Petroleum Research Fund and the National Science Foundation for financial support. In addition, I acknowledge the UW Department of Chemistry's Photonics Research Center, the UW Washington Nanofabrication Facility and the UW Molecular

Analysis Facility for access to the necessary fabrication and characterization tools and equipment.

I would also like to thank Forest Bohrer, Deborah Alterman and Brain Howe at UW's CoMotion for the all of the opportunities, support, learning and advising they provided. Working with CoMotion has helped me grow professionally, given me valuable experience and exposed me to new and exciting opportunities.

I am extremely grateful to my friends and classmates made through UW ChemE and around Seattle for all of the good times had at ACES happy hours, social events, surf trips, mountain adventures and beyond. I also thank my closest friends from childhood and from UT who have always and will always be there for me.

Finally, I would like to thank my wife Taryn for her constant love and support that got me through the really hard times and for making the good times the best of my life. She inspires me to live life to the fullest and sharing my life with her gives me profound joy. I would like to thank my mother, Kellee, for being the most loving mother a son could ask for and a beautiful person who sacrificed so much throughout her life to provide for her children. I would also like to thank my father, Michael, my step-father, Greg, my grandmothers, Carol and Charlotte, my grandparents, Dorothy and Terry, my brothers, Cole and Blue, my sister, Amy, my parents-in-law, Mariano and Kelli, my aunts, uncles, cousins and the rest of my family. I would not be where I am or who I am today without all of your love and support. I love you all more than words can express. Lastly, I would like to dedicate this in loving memory to my grandfathers, James R. Clark and James C. Richardson.

CHAPTER 1. INTRODUCTION

1.1 Introduction

Global energy consumption is growing and is predicted to increase by up to 56% over the next 30 years.[1] Power generation from fossil fuel energy resources has dominated the energy landscape of the industrialized world. These exhaustible energy sources emit greenhouse gases and other pollutants that have led to anthropogenic climate change which, unabated, could result in potentially devastating consequences.[2] Additionally, the finite supply of fossil fuels has led to rising energy costs and national energy security concerns. These problems have created great interest in pursuing renewable and sustainable energy sources. Conversion of solar energy into usable electrical power is of particular interest. The amount of the sun's energy hitting the Earth every hour is enough to power human civilization for a year.[3] Harnessing just a small fraction of the constant 120,000 terawatts the sun provides could help solve the world's greatest energy challenges with no need to emit greenhouse gases or other pollutants.

One way solar energy can be harnessed is by using solar thermal collectors that receive solar radiation and convert it to thermal energy which can be stored or used to create electricity. Photovoltaic (PV) cells, on the other hand, convert incident light directly into electricity. PV cells are semiconductor devices that work under diffuse light and offer scalable installation making them potentially advantageous over solar thermal systems. PVs are a promising clean and sustainable energy source; however, the cost of PV technologies currently prohibits them from competing with conventional energy sources. Research and development is vital to reduce costs and increase the efficiency of PV technologies to help them reach the U.S. Department of Energy's cost target of $0.06 per kilowatt-hour (kWh) for utility scale PV.[4]

1.2 Basic Principles of Photovoltaic Cells

A photovoltaic cell is a device that generates electrical energy directly from light energy. When photons of light are absorbed by matter, their energy is transferred to electrons bound in the material which are then excited to higher energy states where they are more free to move. Normally, the excited electrons quickly relax back to their ground state and the absorbed energy is dissipated thermally in the material. However, a PV cell is a two-terminal electrical diode where the built-in asymmetric conductance pulls the excited electrons away before they relax and feeds them to an external circuit. A potential difference known as a photovoltage is generated by the extra energy of the excited electrons which drives the charges through the external circuit to perform electrical work.[5]

PV cells use semiconductors as the photoactive layers which only absorb photons of light with an energy larger than their bandgap (E_g). When an electron is excited from the valence band above the bandgap to the conduction band, it leaves behind an oppositely charged hole. The bandgap is necessary to make the potential energy gained by electrons from photon absorption available as electrical energy.

The basic operation of a PV cell consists of three primary steps. First, light is absorbed by the active layer to create electron-hole pairs. Second, the electrons and holes are spatially separated. Third, the free charge carriers are collected by their respective electrodes to flow through the external circuit to perform work.

The solar spectrum changes throughout the day and with location so standard reference spectra are used to allow device performance comparisons across the field of study. PV cells are usually tested under simulated sunlight at standard conditions corresponding to an incident light

intensity of 1000 W/m^2 perpendicular to the device surface under the air mass 1.5 global (AM 1.5G) spectrum at a cell temperature of 25˚C. Figure 1-1 shows the standard AM 1.5G spectrum (blue line) which is the standard solar spectrum that hits the earth's surface at a zenith angle of 48˚ at sea level. The dips in the spectrum reflect the absorption of molecules in the atmosphere including oxygen species and water. For reference, Fig. 1-1 also shows the AM0 (black) spectrum for just outside the earth's atmosphere.

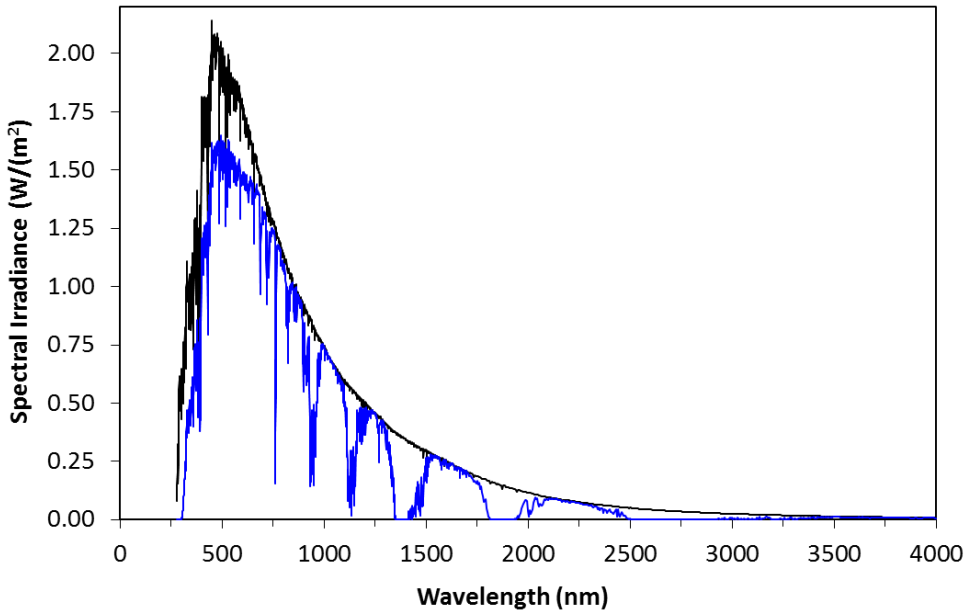

Figure 1-1. Standard solar spectral irradiance data for AM0 (black) and AM1.5G (blue).

Several important parameters are used to characterize PV cells including the short-circuit current (I_{SC}), the open-circuit voltage (V_{OC}), the fill factor (FF), and the power conversion efficiency (PCE). Figure 1-2 shows an I-V curve for a typical device. These curves are generated under standard conditions to measure I_{SC}, V_{OC}, and FF which are used to calculate the PCE. The PCE is the ratio of the maximum output power that the cell could achieve divided by the input power from the sun and is calculated by the following equation[5]:

$$\eta_{PCE} = \frac{P_{max}}{P_{in}} = \frac{V_{MPP} \cdot I_{MPP}}{P_{in}} = \frac{FF \cdot V_{OC} \cdot I_{SC}}{P_{in}}$$

P_{max} is the maximum output power which is equal to the product of V_{MPP} and I_{MPP}, i.e. the voltage and current at the maximum power point, respectively. P_{in} is the power shining on the cell and is 1000 W/m^2 under standard conditions. Under illumination, the photovoltage developed is called the V_{OC} when the terminals of the cell are isolated (i.e. infinite load resistance or open circuit). The I_{SC} is the current measured when the terminals of the cell are connected together (i.e. zero resistance or short circuit). The current is roughly proportional to the illuminated area so the short circuit current density, J_{SC}, is typically used. The FF relates V_{OC} and I_{SC} to V_{MPP} and I_{MPP} and describes the "squareness" of the current-voltage (I-V) curve.

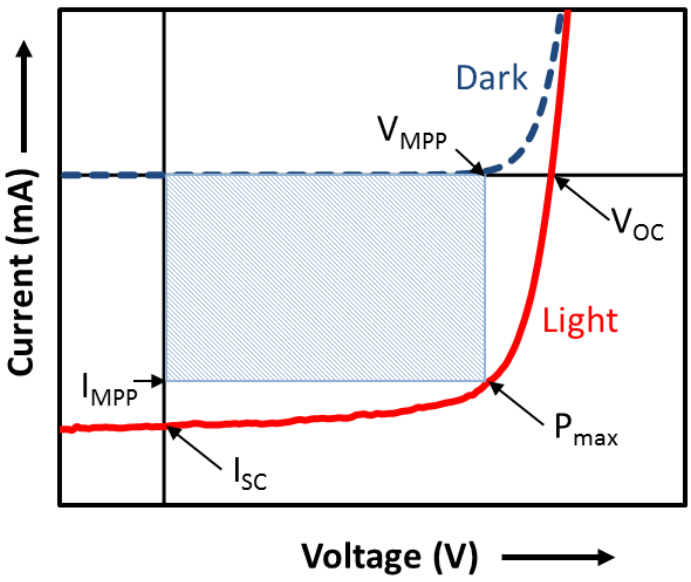

Figure 1-2. Dark (blue) and illuminated (red) I-V curves and the PV parameters of a typical PV device.

1.3 Organic Photovoltaic Cells

In order for renewable and sustainable solar energy production to compete with fossil fuels, advances in materials and device design are required to increase power conversion efficiency and

reduce the cost of manufacturing, installation, and operation of photovoltaic systems. Currently, the PV market relies heavily on wafer-based polycrystalline silicon solar cells which have relatively high manufacturing costs.[6-8] Thin film PV technologies, such as organic photovoltaics (OPVs), offer great potential for lower fabrication and materials costs to become competitive with conventional energy sources.[7-9]

The photoactive layer in OPVs is comprised of organic semiconductors which are carbon-based materials (e.g. polymers and small molecules) whose conjugated backbones primarily consist of alternating C-C and C=C bonds. This conjugation allows electron delocalization along the backbone giving these materials their semiconducting properties.[7] Organic semiconductors readily dissolve in typical organic solvents to make "solar inks" that are solution processable. This ability for solution processing is a primary advantage of OPVs making them compatible with high throughput and large area fabrication techniques such as roll-to-roll printing (R2R).[10] This also allows OPVs to be fabricated at low temperatures on mechanically flexible substrates which can further lower costs via production energy savings and structural savings as lightweight devices require less reinforcement to support modules and panels.[6] Flexible solar cells could also lead to unique and broadly applicable possibilities for ubiquitous power generation on both large and small scales. OPV's use of organic semiconductors also means that they are made from abundant materials with low specific weight and tunable material properties.[7]

A primary difference between OPVs compared to inorganic PVs is that free charge carriers are not generated upon photo-excitation in organic semiconductors. In OPVs, an absorbed photon creates an exciton (electron-hole pair) that is tightly bound by the strong Coulomb interaction between the electron and hole due to the low dielectric permittivity in organic semiconductors.[7, 9] Excitons in OPV systems have a typical binding energy of ~0.2-1 eV

[7, 11] and must be dissociated into free charge carriers that can be collected to do electrical work. Exciton dissociation requires a strong local electric field which can be supplied externally or by material interfaces that provide a sufficient energy level offset. OPV active layers typically consist of an electron donor (i.e. p-type) and an electron acceptor (i.e. n-type) where the lowest unoccupied molecular orbital (LUMO) and the highest occupied molecular orbital (HOMO) of the acceptor are both lower in energy than those of the donor. Figure 1-3 shows a simple energy level diagram depicting the donor-acceptor energy level offset required to separate an exciton in an OPV system allowing the free charges to be transported to the electrodes.

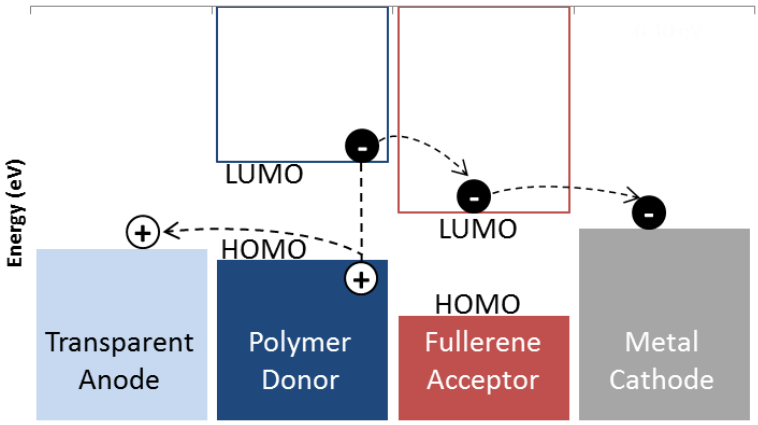

Figure 1-3. Simple energy level diagram depicting the energy level offset required to separate an exciton in an OPV system.

These staggered energy levels provide the driving force for exciton dissociation at the donor-acceptor interface. Also, the V_{OC} is limited by the difference in the HOMO of the donor and the LUMO of the acceptor, i.e. the energy level difference of the separated charges. Once the exciton is dissociated, the electrons and holes can travel through the acceptor and donor materials to the cathode and anode, respectively, and into an external circuit to perform electrical work.[7]

Efficient charge separation and transport in the active layer are key components required for maximizing PCE in OPVs. The earlier OPV devices used a donor-acceptor heterojunction in the form of a planar bilayer for charge separation. The photo-generated excitons must reach the donor-acceptor interface within their lifetime before they decay, i.e. geminate recombination via radiative or non-radiative pathways, and their energy for power conversion is lost. This planar heterojunction has a small donor-acceptor interface area, so excitons are less likely to reach it for charge separation, and requires long carrier lifetimes to ensure the separated charges reach the electrodes.[7] The bulk heterojunction (BHJ), i.e. a mixture of the donor and acceptor materials to form a bicontinuous interpenetrating network, was formed to address this problem by increasing donor-acceptor interface area for exciton separation. For efficient charge separation, the BHJ should be well mixed so that the width of the donor and acceptor domains is approximately twice the size of the exciton diffusion length, i.e. the average distance an exciton can move from the point of generation until it recombines (~10 nm).[7] For efficient charge transport, both phases should form continuous percolating networks to connect the bulk of the film to the electrodes. Therefore, control of the blend microstructure and morphology is very important and control strategies include using processing additives and thermal annealing to control the BHJ solidification dynamics.[9] A large amount of research effort has been put into this subject, especially using the poly(3-hexylthiophene-2,5-diyl)(P3HT):phenyl-c61-butyric acid methyl ester (PCBM) BHJ.[7, 9, 12] Figure 1-4 shows a schematic of a simple OPV device (left) with the active layer sandwiched between two electrodes and a zoomed-in depiction of a BHJ (right) showing the idea of exciton generation, exciton diffusion to the donor (polymer)-acceptor (fullerene) interface, and charge dissociation at the interface allowing charge transport through the respective materials to the electrodes.

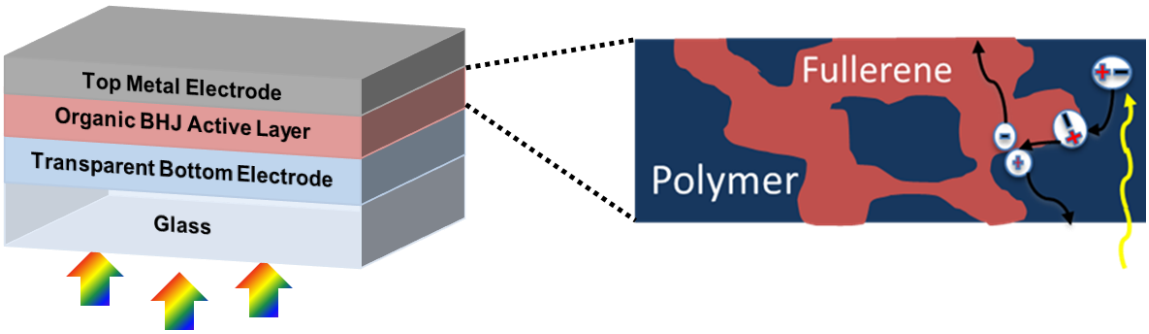

Figure 1-4. Schematic of a simple OPV device (left) with the active layer sandwiched between two electrodes and a zoomed-in depiction of a BHJ (right) showing the idea of exciton generation, exciton diffusion to the donor (polymer)-acceptor (fullerene) interface, and charge dissociation at the interface allowing charge transport through the respective materials to the electrodes.

Charge collection efficiency is also important for reaching high PCE. The electrodes in an OPV device should be selective so that electrons are preferentially collected at one and holes at the other. One way to create this selectivity is to choose electronically different electrodes, i.e. one high and one low work function electrode. OPVs typically use a conventional architecture where the BHJ layer is sandwiched between a high-work function transparent conducting oxide (e.g. indium tin oxide (ITO)) as the bottom hole-collecting anode and a low-work function metal (e.g. Al) for the top electron-collecting cathode. In addition to the chosen electrode material, the interfacial layers between the electrodes and the active layer have a significant impact on the selectivity and charge collection efficiency. A doped conducting polymer like poly(3,4-ethylenedioxythiophene):poly(styrene sulfonate) (PEDOT:PSS) is usually placed on top of the ITO to raise the work function for improved hole collection. Likewise, a cathode interfacial layer, such as Ca or LiF, is used to lower the work function of the top electrode to accept

electrons.[9] Poor energetic matching and high resistance of the combined interfacial layer/electrode structures can create imperfect contacts that can limit the device V_{OC} and FF.[9]

Materials research is active in the OPV field. New, rationally designed semiconducting polymers with low optical band gaps (to increase J_{SC}) and increased ionization potentials (to increase V_{OC}) have led to large performance improvements. The combination of materials design, morphology control, and interface engineering has led to PCEs as high as ~9-10.7% for OPVs.[7, 13, 14] The substantial progress of OPVs to reach such high PCEs highlights their promise in helping solar energy become a competitive and prevalent renewable power source.

1.4 Organic-Inorganic Hybrid Photovoltaic Cells

Searching for new materials to reduce manufacturing costs and increase the PCE of solar cells can reduce the cost per kilowatt-hour ($/kWh) of energy produced from these devices bringing them closer to and beyond grid parity. Research in this field has led to the synthesis of various organic conjugated polymers and inorganic semiconducting nanocrystals (NCs) with advantageous properties for use in PVs. These materials both offer compatibility with well-established solution processing techniques allowing low-cost, large area production. Conjugated polymers have high light absorption coefficients compared to silicon and can be used with mechanically flexible substrates.[15] Semiconducting NCs have high carrier mobilities, a tunable band gap allowing optimizable light harvesting, and higher light absorption coefficients than fullerenes commonly used in OSCs.[16] In recent years, hybrid organic-inorganic NC solar cells have garnered much attention aiming to exploit the potential advantages of each class of materials.[16, 17]

Several different polymer-NC blends have been deployed to make hybrid solar cells. P3HT is a highly studied conjugated polymer used commonly in OSCs and has been mixed with CdSe and CdS nanocrystals yielding PCEs as high as 2.6%.[18] Dayal *et al.* fabricated a hybrid device exhibiting a PCE of 3.1% using CdSe tetrapods and a low band gap polymer, poly[2,6-(4,4-bis-(2-ethylhexyl)-4H-cyclopenta[2,1-b;3,4-b′]dithiophene)-alt-4,7-(2,1,3-benzothiadiazole)] (PCPDTBT).[19] More recently, Seo *et al.* used PbS nanocrystals along with a low band gap polymer, poly(2,6-(N-(1-octylnonyl)dithieno[3,2-b :20,30- d]pyrrole)- alt -4,7-(2,1,3-benzothiadiazole)) (PDTPBT), and solid-state ligand treatment to make a device with a PCE of 3.8% [20].

However, these semiconductor nanomaterials contain toxic elements like Cd and Pb making them less desirable for large-scale application due to potential health and environmental hazards. Alternately, pyrite iron disulfide FeS_2 is an earth-abundant and environmentally benign material with low procurement costs, a large optical absorption coefficient ($>10^5$ cm^{-1}), and increased light absorption in the near infrared (NIR) region due to an indirect band gap of ~0.95eV [21-23]. The hybrid devices fabricated in this report focus on the use of pyrite FeS_2 nanocrystals.

1.5 Inverted Structure for Organic Photovoltaic Cells

OPV devices with the conventional structure are not stable in ambient conditions as prolonged exposure in air can cause oxidation of the top electrode and degradation of the active layer.[24] Conventional devices typically use PEDOT:PSS as the hole-collecting layer on ITO. However, long-term stability of this layer on ITO is also a problem as PEDOT:PSS is hygroscopic, acidic and can etch the ITO leading to indium contamination in the polymer

thereby degrading performance.[25, 26] Also, the deposition of metal directly onto the active layer may lead to metal diffusion into the film adversely affecting its semiconducting properties.[24]

Alternatively, an inverted configuration can alleviate these issues by using a high-work function metal (e.g. Ag, Au, or Pt) as the top anode and ITO as the bottom cathode thereby eliminating the ITO/PEDOT:PSS interface. These high-work function metals are more stable in air and act as a self-encapsulating layer improving device lifetime and stability.[24] They are also compatible with coating and printing techniques which can simplify and lower the cost of large-scale manufacturing.[26] Depending on the active layer design, the inverted architecture may also take advantage of the inherent vertical phase separation observed in some organic blends.[27] Figure 1-5 (a) and (b) show schematics of a conventional and an inverted OPV device.

In inverted devices, it is important to prepare a selective bottom cathode to effectively reverse the device polarity from a conventional to an inverted structure.[25, 26] This is typically achieved by forming an electron transport layer (ETL) on ITO. This ETL should have good optical transparency, low resistivity for electron conduction, and an appropriate conduction band (CB) level and bandgap (E_g) for high selectivity of electrons while also blocking holes. Various wide bandgap, n-type metal oxides, such as TiO_2, ZnO, Cs_2CO_3, and certain polyelectrolytes with a large dipole moment have been successfully deployed as interfacial ETLs in inverted devices.[14, 24, 26, 28, 29] Additionally, varied forms of layer nanostructuring, surface treatment, and processing additives have been explored to improve charge collection efficiency, transport and selectivity.[30-33]

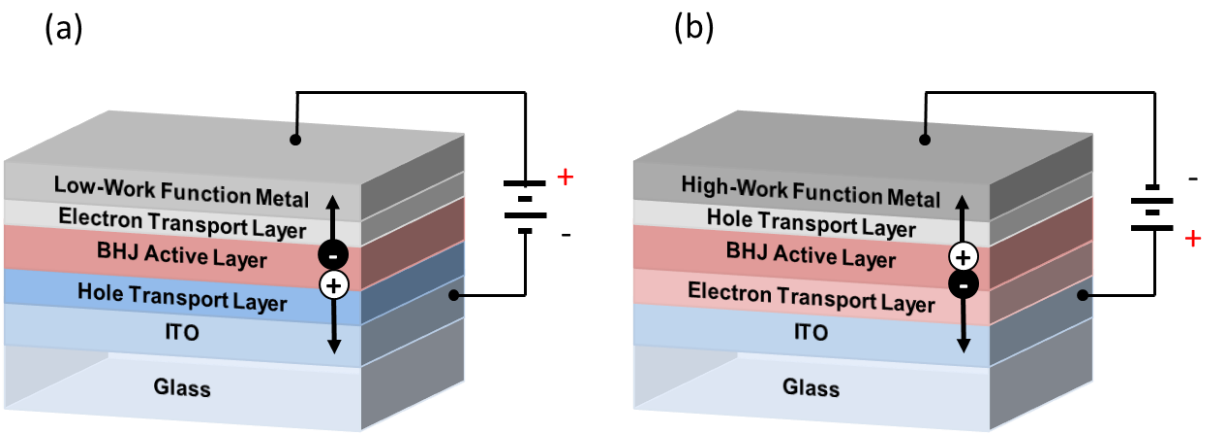

Figure 1-5. Schematic of (a) a conventional and (b) an inverted OPV device.

Inverted devices with the structure ITO/ZnO/P3HT:$PC_{60}BM$/PEDOT:PSS/Ag have reached PCEs ranging from 1.8% to 3.8%.[24, 34] By inserting a C_{60}-SAM on top of the ZnO layer in devices with this structure, the PCEs were increased further to an average of 4.5% due to enhanced electronic coupling of the inorganic/organic interface.[27, 31] Other interfacial layers and additives have been explored to improve the PCE of inverted devices as well.[35-37] For example, C-PCBSD was used in the device of ITO/ZnO/C-PCBSD/ P3HT:PCBM/PEDOT:PSS/Ag to achieve a PCE of 4.4%.[36] The interfacial layer of Cs_2O_3 and hole collection layer of MoO_x were used in the device of ITO/ZnO/Cs_2O_3/P3HT:PCBM/MoO_x/Al to give a PCE of 4.26%.[37]

This inverted architecture is also well-suited for implementation with new low-band gap polymer BHJs, such as the high efficiency blend of the semiconducting polymer thieno[3,4-b]thiophene/benzodithiophene (PTB7) and [6,6]-phenyl C71-butyric acid methyl ester ($PC_{71}BM$). Conventional devices using PTB7 reached as high as 7.4% PCE when the additive diiodooctane (DIO) was added to the chlorobenzene solvent to enhance polymer packing.[38] Inverted devices using PTB7 with a ZnO ETL showed higher PCEs reaching 8.07%.[30] This PCE

was pushed even further to 9.15% when used in inverted devices where a conjugated polymer, poly [(9,9-bis(3′-(N,N-dimethylamino)propyl)-2,7-fluorene)-alt-2,7-(9,9–dioctylfluorene)] (PFN), was used as an ITO surface modifier.[14]

1.6 Plasmonically Enhanced Organic Photovoltaic Cells

The critical price point for PV to break even with conventional energy sources is much less than $1/W while the production cost of current silicon PV technology is approximately $1-2/W.[6] As discussed previously, OPV's advantages allow it to potentially provide electrical power at overall costs lower than silicon or thin-film PV.[6] However, it is generally accepted that OPVs need to achieve PCEs greater than 10% on an industrial scale to be competitive with other technologies. Despite their advantages, OPVs tend to have lower exciton diffusion lengths and smaller charge carrier mobilities compared to their inorganic counterparts.[8] These factors limit the thickness of OPV active layers which inherently limits light absorption and PCE. Thus, a central challenge for OPVs is the trade-off between an active layer of sufficient film thickness to absorb as much light as possible while minimizing charge recombination. This balance between absorption and recombination typically results in using thin active layers that do not take full advantage of the incident light. Light trapping and manipulation techniques offer an attractive approach to maximizing the absorption of sunlight which is key to pushing OPVs beyond 10% PCE.

Integrating PV devices with novel metallic nanostructures that produce surface plasmon polaritons (SPPs) upon interaction with light is one promising way to enhance light trapping and absorption.[8, 39] A plasmon is a quasiparticle arising from the quantization of electron density oscillations in a conductor and it can couple with a photon at the interface of a metal and a dielectric material, for example, to create an SPP. In this coupling interaction between a

plasmon and photon, the free electrons of the metal respond collectively by oscillating in resonance with the light wave. This resonant interaction between the surface charge oscillation and the electromagnetic field of the light constitutes the SPP.[40] Figure 1-6(a) depicts the combined electromagnetic (EM) wave and surface charge character of SPPs. Most of an SPP's properties can be derived directly from Maxwell's equations. The momentum of an SPP mode ($\hbar k_{SP}$) is greater than that of a free space photon ($\hbar k_0$) of the same frequency and this momentum increase is associated with the binding of the SPP to the metal surface.[40] This momentum mismatch must be overcome in order for SPP modes and light to couple together. The missing momentum can be provided by use of a prism to enhance the momentum of incident light, scattering from a subwavelength feature (e.g. nanohole or protrusion), or periodic corrugation of the metal surface. Once the SPP is formed, it is strongly bound to the surface of the metal at the interface with the dielectric material and can propagate along the surface for relatively large distances (e.g. 10-100 μm with Ag).[40] Formation of SPPs creates strong local electric fields that decay exponentially with distance perpendicular to the surface as shown in Fig. 1-6(b). The decay length of the fields in the dielectric material is on the order of half the wavelength of the coupled light.[40]

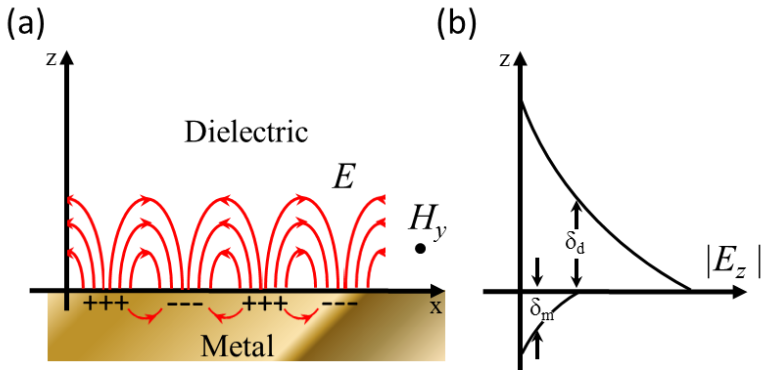

Figure 1-6. (a) Schematic showing the combined EM wave and surface charge character of SPPs at a metal and dielectric interface. (b) The electric field is enhanced near the surface and decays exponentially with decay lengths δ_d into the dielectric and δ_m into the metal.

The plasmonic and optical properties of SPPs, including the wavelength at which resonance occurs (i.e. where maximum photon coupling occurs) and the intensity of the electromagnetic fields produced, strongly depend on the materials and nanostructures present.[41] The resonant frequency of an SPP is very sensitive to the refractive index of the environment. Thus, the properties of an SPP can be tuned by varying the metal thickness and the choice of metal and dielectric materials themselves. Localized surface plasmon polaritons (LSPPs) result when an SPP is confined to a subwavelength feature and exhibit greatly enhanced local electric fields. In addition to the choice of metal, dielectric, and metal thickness, the properties of LSPPs can be tuned by varying the size, shape, and spatial arrangement of the subwavelength constituents. For example, by adding nanoholes into a metal surface, propagating SPPs and LSPPs are generated at the metal surface. The size and spacing of the nanoholes can be changed to tune the resonance frequency and electric field intensity of the LSPPs.[41]

The properties of plasmonic nanostructures can be engineered to exploit SPPs in order to concentrate and trap light inside a device, broaden the absorption band for the active layer, and achieve omnidirectional absorption enhancement (i.e. large tolerance to angle of incident light). The most extensively studied approach is by integrating plasmonic nanoparticles (NPs), typically Au or Ag NPs, into the various layers of an OPV device.[42, 43] The SPPs confined in nanometer sized structures like NPs creates localized surface plasmon resonance (LSPR). These metallic NPs can be placed outside the active layer, inside the active layer, or both to achieve enhancements. One way metallic NPs can enhance performance is by acting as subwavelength scattering elements that couple and trap freely propagating sunlight into the device. When the NPs are placed close to the interface between two dielectrics, the light will scatter preferentially into the dielectric with the larger permittivity.[39] Additionally, most OPVs have a reflecting metal

back electrode that will reflect transmitted light back through the device which then couples to the NPs and is partly reradiated again into the device by the same scattering mechanism just mentioned which increases the effective path length of light.[39] In addition to plasmonic NPs, 1D and 2D metallic nanostructures can be integrated into devices to provide similar light absorption enhancements.[44-47] It could be highly beneficial to integrate these nanostructures as the electrodes themselves to take advantage of plasmon-induced optical enhancements while also replacing ITO with a cheaper and more mechanically robust material.[48]

1.7 Objectives and Goals

The encompassing goal of this work is to explore new materials, nanostructures, and device designs that add to the collective knowledge of the PV community and provide insight, ideas and inspiration towards developing lower cost and more efficient PV technologies. The objectives of this research include:

1. Synthesize and characterize semiconducting pyrite FeS_2 NCs and study their role in inverted hybrid BHJ devices as a highly abundant and non-toxic PV material;
2. Synthesize ZnO electron transport layers of varied nanostructure, characterize their morphological and optical properties, and understand the relationship of these properties to device performance in high efficiency inverted OPVs;
3. Design and develop plasmonic nanostructured electrodes, characterize their optical and electrical properties, and understand their effect on device performance for high efficiency, ITO-free inverted OPVs on rigid and flexible substrates.

CHAPTER 2. INVERTED HYBRID SOLAR CELLS BASED ON PYRITE FeS_2 NANOCRYSTALS IN P3HT:PCBM WITH ENHANCED PHOTOCURRENT AND AIR-STABILITY

2.1 Introduction

Significant scientific effort has been put into developing new materials to reduce manufacturing costs and increase power conversion efficiency (PCE) of solar cells. Organic conjugated polymers and inorganic semiconductor nanocrystals (NC) are two such materials that each have unique and advantages properties. Hybrid organic-inorganic nanocrystal (NC) solar cells have garnered much attention aiming to exploit the potential advantages of each class of materials [16, 17]. However, many of the semiconductor NCs developed contain toxic elements like Cd and Pb making them less desirable for large-scale application due to potential health and environmental hazards.

Pyrite iron disulfide FeS_2 is an earth-abundant and environmentally benign material with low procurement costs, a large optical absorption coefficient ($>10^5$ cm^{-1}), and increased light absorption in the near infrared (NIR) region due to an indirect band gap of ~0.95eV [21-23]. It was first investigated for use in photovoltaics (PV) over 25 years ago and has seen renewed interest over the past few years due to its great potential as a sustainable PV material [22, 23, 49-54]. Several recent publications exhibited successful and robust synthesis of pyrite nanocrystals and many efforts have been directed towards exploring their optoelectronic applications [50-58]. In 2009, a conventional hybrid BHJ solar cell was reported with an indium tin oxide (ITO)/ Poly(3,4-ethylenedioxythiophene) :poly(styrenesulfonate) (PEDOT:PSS)/P3HT:FeS_2 NC/Al structure that

showed extended red light harvesting up to 900 nm resulting from the pyrite NCs [50]. However, the PCE of this device was only 0.16%, no further optimization was done, and no other work has reproduced or improved upon those results. In 2010, conventional BHJ devices embedded with small amounts of FeS_2 NCs (0.1-0.4 wt%) using an ITO/PEDOT:PSS/P3HT: phenyl-c61-butyric acid methyl ester (PCBM):FeS_2/Al structure were reported showing a 14% photocurrent enhancement with up to 0.3 wt% NC loading [52]. In 2012, one report exhibited FeS_2 NC-based solar cells with varying architectures, including Schottky barrier, depleted heterojunction, and conventional hybrid BHJ structures, but observed no photoresponse and no rectification in any of the devices [57]. Most recently, an all-inorganic solar cell with an ITO/PEDOT:PSS/poly[(9,9-dioctylfluorenyl-2,7-diyl)-co-(4,4'-(N-(4-s butylphenyl)) diphenylamine)](TFB)/FeS_2:CdS/Al structure showed more promising results with a PCE of 1.1% [58]. Another group synthesized FeS_2 NCs with improved stability in air and observed a photoresponse in an ITO/FeS_2 NC/Al device [53]. Not surprisingly, no rectification behavior was shown as the pyrite formed ohmic contacts at the ITO and Al interfaces. Trioctylphosphine oxide (TOPO) was used as a ligand in this work and it was hypothesized that TOPO stabilizes the pyrite FeS_2 NC surface in air by passivating both Fe and S sites. Additionally, a photodiode with a ITO/ZnO/FeS_2 NC/MoO_3/Au structure was reported that exhibited rectification, a strong photoresponse, and spectral response from visible to NIR wavelengths [54]. Despite these recent works and renewed interest in pyrite FeS_2 over the past several years, no high performance device has been made based on this material. Further investigation into the fundamental properties of pyrite FeS_2 and deployment in alternative device architectures are required to fully explore the potential of pyrite FeS_2 for use in PV.

In this work, pyrite FeS_2 NCs synthesized with TOPO additives were deployed in hybrid BHJ devices with an inverted architecture to mitigate leakage current and to enhance the efficiency and stability of pyrite-based hybrid solar cells. The chemical states of iron and sulfur elements in the "bulk" and at the surface of as-synthesized pyrite NCs were investigated using X-ray photoelectron spectroscopy (XPS). A dramatic increase in the content of oxidized iron species was exhibited, which could be due to the oxygen alloying of FeS_2 NCs or the capping of surface Fe(II) species with TOPO ligands. The valence (E_{VB}) and conduction (E_{CB}) band edges and the band gap were determined using UV-Vis-NIR absorption and cyclic voltammetry (CV). A larger band gap (E_g ~ 1.7eV) of the NCs may possibly be due to oxygen alloying, resulting in an increased E_{CB} without introducing interband trap states [59]. Inverted ternary hybrid BHJ solar cells were fabricated with the pyrite FeS_2 concentration varying from 0 to ~ 4 wt% in a P3HT:PCBM active layer and three distinct performance regimes were observed that appear linked to microstructure transitions. By adding FeS_2 NCs up to ~0.5 wt% in the films, photocurrent enhancements of up to 20% were consistently obtained as the FeS_2 NCs served to enhance the film morphology increasing charge generation and transport. After exposure to air for 28 days, these hybrid devices showed a large improvement in fill factor (FF) and open-circuit voltage (V_{OC}) and a PCE enhancement of up to 28% compared to the control device with no FeS_2. The external quantum efficiency (EQE) was measured for the inverted ternary devices and the photoluminescence (PL) and UV-Vis-NIR spectra were measured for various blend films. The possible charge generation, separation and transport mechanisms are discussed.

2.2 Experimental

2.2.1 Pyrite NC Synthesis

Pyrite FeS_2 NCs were synthesized based on the method developed by Puthussery *et al.* [51], which was modified by doubling the molar concentration of iron and sulfur reagents and by adding TOPO. Specifically, 200 mg of iron(II) chloride tetrahydrate ($FeCl_2 \cdot 4H_2O$) (Aldrich), 10 g of octadecylamine (ODA) (Acros) and 1159.89 mg of TOPO (Aldrich) were mixed in a three-neck flask under nitrogen atmosphere and stirred at 120°C under nitrogen flow for one hour. In a separate flask, 192 mg of sulfur (Aldrich) and 5 mL of diphenyl ether (DPE) (Acros) were combined under nitrogen atmosphere and stirred at 70°C under nitrogen flow for one hour. The contents of the sulfur pot were rapidly injected into the iron pot at 120°C and the temperature was quickly raised to 220°C where the reaction was held for two hours under nitrogen flow. At the end of the reaction, the heating mantle was removed and the flask was allowed to cool to ~100°C when the reaction mixture was transferred to a glass bottle and stored in a nitrogen filled glove box. The NCs were washed at least three times by solvent/antisolvent precipitation with degassed chloroform (Sigma Aldrich) and methanol (Sigma Aldrich) inside the glove box and redispersed in chloroform.

2.2.2 Pyrite NC Characterization

Pyrite crystalline phase purity was confirmed with powder X-ray diffraction (XRD) using a GADDS D8 Discover diffractometer (Bruker) using Cu-Kα radiation ($\lambda = 1.5419$ Å). Transmission electron microscopy (TEM) images were taken using an FEI Tecnai TEM to view the shape and size of NCs and dynamic light scattering (DLS) (Malvern Zetasizer Nano-ZS) was used to further quantify the NC size in chloroform. UV-Vis-NIR absorption spectra of pyrite NCs in chloroform were gathered with a Perkin Elmer Lambda 900 UV-Vis-NIR absorption

spectrometer. X-ray photoelectron spectroscopy (XPS) was used to probe the elemental composition and the chemical state of the NCs. XPS measurements were conducted using a Surface Science Instrument S-Probe spectrometer equipped with a monochromatic Al Kα source (KE = 1486.6 eV), a hemispherical analyzer, and a multichannel detector. The elemental composition was determined from spectra acquired at a pass energy of 150 eV. All XPS data were acquired at a nominal photoelectron takeoff angle of 55°. SSI data analysis software was used to calculate the elemental compositions from the peak areas [60].

2.2.3 Cyclic Voltammetry Measurements

Cyclic voltammetry (CV) was used to determine the valence and conduction band edges of the pyrite FeS_2 NCs. Acetonitrile (Sigma Aldrich) and tetrabutylammonium hexafluorophosphate ($TBAPF_6$) (Sigma Aldrich) were used as received to prepare an electrolyte solution of 0.1 M $TBAPF_6$ in acetonitrile for the CV cell. To prepare the working electrodes, solutions of pyrite NCs in chloroform were spray coated onto platinum (Pt) wires using an air brush and nitrogen. The counter electrode (Pt) and a silver/silver ion reference electrode (Ag in 0.1 M $AgNO_3$ solution) were placed into a cell containing the electrolyte solution which was then purged with nitrogen for >10 minutes before measurements were gathered. After purging, the working electrode was placed into the cell and a blanket of nitrogen was flowed over the headspace during the experiment. All CV scans were taken with an EG&G Princeton Applied Research Potentiostat/Galvanostat Model 273A and data were collected and analyzed using PowerSuite Electrochemistry Software. The reference electrode was calibrated by running CV on ferrocene (Aldrich) as an internal standard with a bare Pt working electrode. During the experiment, the potential values were obtained in reference to the Ag/Ag^+ electrode and were later converted in reference to the internal standard of ferrocenium/ferrocene (Fc^+/Fc). Next, the

potential values referenced to the Fc^+/Fc redox couple were converted to reference a saturated calomel electrode (SCE) and used along with empirical correlations to estimate E_{VB} and E_{CB}[61]. The average E_{VB} and E_{CB} based on several CV measurements was ~-5.6 eV and ~-3.9 eV, respectively. These estimates suggest the band gap (E_g) is ~1.7 eV.

2.2.4 Device Fabrication

Inverted hybrid BHJ devices were fabricated with fixed concentration and ratio of P3HT (Rieke 4002-E) and PCBM (Nano-C PCBM-BF) but varied pyrite NC concentrations. The pyrite FeS_2 NCs were washed at least three times, redispersed in chloroform, and filtered through a 0.2 μm polytetrafluoroethylene (PTFE) syringe filter to make a base stock solution. Various dilutions of the base stock solution were prepared with concentrations ranging from 0.1 to 4.5 mg/mL. Each of the individual solutions of FeS_2 NCs, P3HT (30.5 mg/mL), and PCBM (24.5 mg/mL) in chloroform were stirred overnight at 600 rpm and 45°C. Note that our pyrite FeS_2 NCs were more soluble in chloroform versus others solvents, including chlorobenzene. Therefore, we chose chloroform to maximize the uniform dispersion of the NCs in the blend films while attempting to minimize aggregation. After stirring, the P3HT and PCBM solutions were filtered with a 0.2 μm PTFE syringe filter and mixed with FeS_2 NC solutions with different concentrations for at least one hour to form the solutions for making the active BHJ layers. The final blend solutions for all devices and films had constant concentrations of P3HT (12.2 mg/mL) and PCBM (9.8 mg/mL) and a constant P3HT:PCBM weight ratio of 1:0.8, where applicable. The pyrite NC concentration in the ternary BHJ layer, for example, 0.5 wt%, means that the mass of the NCs makes up 0.5 wt% of the combined mass of P3HT, PCBM, and pyrite FeS2 in the film. ITO-coated glass substrates were used for all devices and were first cleaned by

several ultrasonication steps in soapy deionized (DI) water, DI water, acetone, and isopropanol. The substrates were treated with oxygen plasma prior to depositing any films.

A procedure based on Hau et al. was used to fabricate the inverted BHJ devices [24]. ZnO nanoparticles (Sigma-Aldrich) were spin-coated at 3000 rpm onto the cleaned ITO substrate to form a ~50 nm electron selective layer and baked at 140°C for 10 minutes. Next, the active layer was spin-coated at 1000 rpm and annealed at 150°C for 10 minutes in a glove box under a nitrogen atmosphere. A dilute PEDOT:PSS (Clevios P VP AI4083) solution was prepared and spin-coated at 5000 rpm in air on top of the active layer to form a ~40 nm thick hole conducting layer which was baked at 120°C for 10 minutes. Finally, four silver electrodes with thicknesses of 100 nm and areas of 10 mm^2 were thermally evaporated on each chip through a shadow mask at the background pressure < 10^{-6} torr.

2.2.5 Device Characterization

Current-voltage measurements for all inverted devices were conducted in a glove box under nitrogen atmosphere using a Keithley 2400 Source Meter and a solar simulator with a Solar Light Co. Xenon lamp (16S-300W) and an AM 1.5 filter. The light intensity was calibrated to 100 mW/cm^2 using a calibrated silicon solar cell that had been previously standardized at the National Renewable Energy Laboratory. EQE measurements were gathered in air using an Oriel Xenon lamp (450 W) with an AM 1.5 filter, a monochromator (Oriel Cornerstone 130 1/8m), and a lock-in amplifier (Stanford Research Systems).

2.2.6 Active Layer Characterization

Various binary and ternary films were fabricated per above for further characterization. Scanning electron microscopy (SEM) and tapping mode atomic force microscopy (TM-AFM)

were used to study the film morphology and microstructures using an FEI Sirion SEM and a DI Multimode AFM, respectively. PL measurements were taken with a Horiba Fluorolog FL-3 spectrofluorometer. UV-Vis-NIR absorption spectra were obtained using Perkin Elmer Lambda 900 UV-Vis-NIR absorption spectrometer.

2.3 Results and Discussion

The morphology, size and crystalline phase of synthesized pyrite FeS_2 NCs were characterized using TEM, DLS and XRD, respectively. Figure 2-1(a) shows a TEM image of the pyrite FeS_2 NCs with slightly elongated shapes and a relatively monodisperse size distribution. A high resolution TEM image in Figure 2-1(b) shows the clear lattice fringes with a *d* spacing of 2.7 Å corresponding to the (002) plane of pyrite. DLS measurements in Figure 2-1(c) also show a relatively monodisperse size distribution of pyrite NCs with a polydispersity index (PDI) of 0.17 and an average radius of ~27 nm. Pyrite crystalline phase purity was confirmed with the XRD pattern, shown in Figure 2-1(d), which is consistent with that of standard pyrite FeS_2 (JSPDS File No. 42-1340).

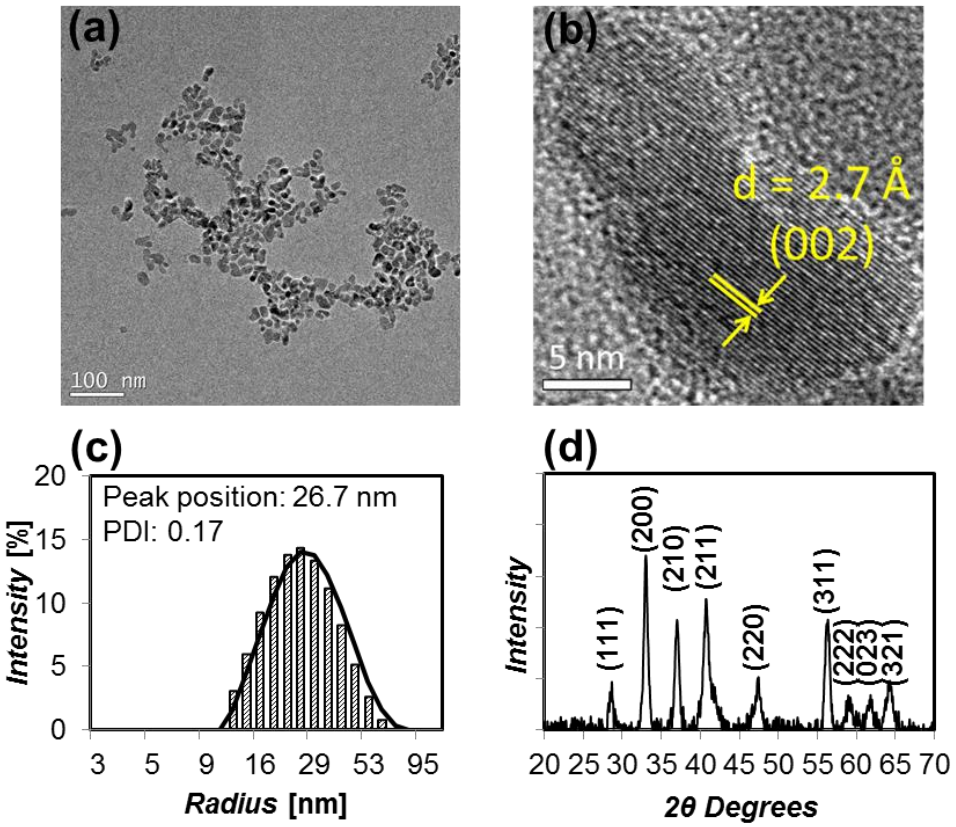

Figure 2-1. (a) TEM image and (b) high resolution TEM image of synthesized FeS_2 NCs. (c) Size distribution of the pyrite NCs in chloroform determined by DLS. (d) Powder XRD pattern of the pyrite FeS_2 NCs.

Although pure pyrite phase of synthesized NCs was confirmed by XRD, the chemical states of Fe and S elements and their chemical environments at the surface and in the "bulk" could significantly affect the electronic structures of the valence and conduction bands. XPS measurements were performed to investigate the local chemical states of Fe and S elements of synthesized pyrite FeS_2 NCs. XPS as a surface characterization tool has been extensively used in studying the local chemical states of elements in the near surface regions (~ 10 nm) of solids by measuring the kinetic energy of emitted photoelectrons upon excitation with an X-ray beam [62]. Semiconductor NCs have a small size ranging from several nanometers to several tens of nanometers and thus a relatively large surface-to-bulk ratio. Therefore, using XPS to study NCs,

one can consider that both surface and some "bulk" chemical states of elements in NCs can be probed. The high-resolution S 2p and Fe $2p_{3/2}$ XPS spectra of pyrite FeS_2 NCs synthesized with the TOPO additive and 2 hour reaction times are shown in Figure 2-2. The possible near surface species detected and their corresponding binding energy, full width at half-maximum (FWHM), and area percentage are summarized in Table 2-1. The S 2p and Fe $2p_{3/2}$ spectra showed that S_2^{2-} and Fe(II)S_2, respectively, are the dominant species which correspond to the bulk pyrite structure. Species such as S^{2-}, polysulfides, and Fe(III)S can result from bonds breaking on the NC surface. For instance, if a S-S bond breaks, the resulting S^- ion could be stabilized by the transfer of one electron from an adjacent Fe(II) surface site resulting in the formation of S^{2-} and Fe(III) [62]. Another means to form the S^{2-} species at the surface occurs if an electron transfers from one S^- to another S^- producing an S^{2-} and S^0 species. The latter may form near-surface polysulfides by reaction with adjacent disulfide ions [62]. The presence of SO_4^{2-} is indicated in the S 2p spectrum by a small peak at 168 eV. The Fe $2p_{3/2}$ spectrum in Figure 2-2 shows a large peak between 710 and 712 eV arising from the presence of various oxidized species as listed in Table 2-1. For comparison, XPS spectra were also taken for pyrite FeS_2 NCs synthesized using the same conditions but without TOPO additive (see Table 2-1). A dramatic increase in the content of oxidized iron species was observed in the Fe $2p_{3/2}$ spectrum of the product synthesized with TOPO additive, especially the Fe(II)-O species. This could be due to the oxygen alloying of FeS_2 NCs caused by an "oxygen rich" environment from the TOPO additive during synthesis or by the surface capping of Fe(II) with TOPO ligands. Octadecylamine (ODA) can coordinate with the iron atoms of the NCs through its nitrogen atom while TOPO is expected to coordinate with both iron and sulfur atoms through its oxygen and phosphorous atoms, respectively [53]. It is suggested that TOPO will preferentially bind to iron atoms over ODA because phosphine oxides

are slightly stronger bases than amines [53]. The survey scan (Figure 2-3) showed that the pyrite NCs synthesized with TOPO additive have almost equal amounts of P and N, indicating that both ODA and TOPO are the capping ligands at the NC surfaces. These results demonstrate that the local chemical states of Fe and S in the pyrite NCs could be significantly influenced by the reaction conditions. As discussed next, this could also affect the electronic structure of the pyrite NCs.

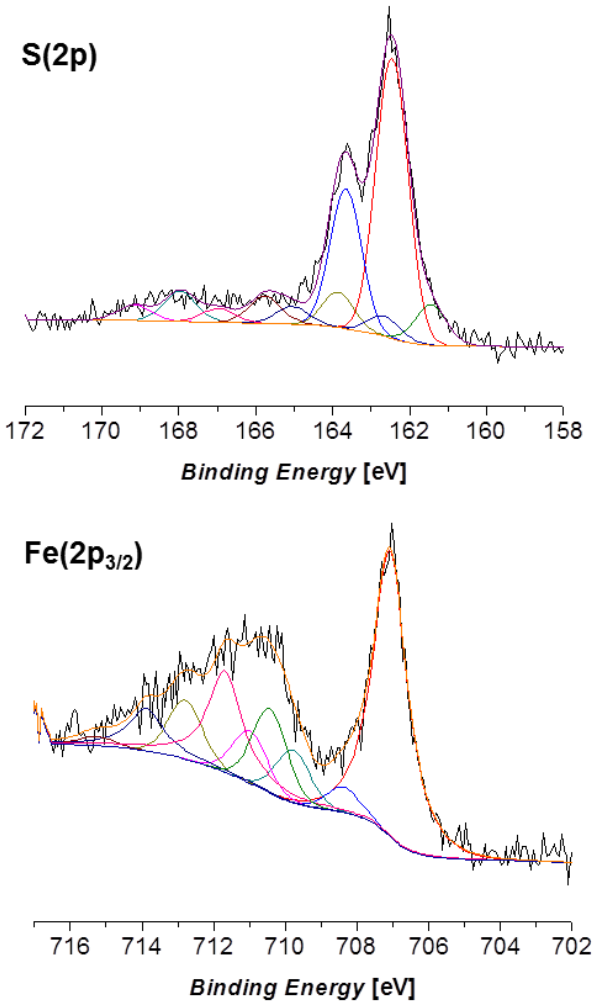

Figure 2-2. High-resolution S 2p and Fe $2p_{3/2}$ XPS spectra of pyrite NCs synthesized with ODA and DPE as solvents to dissolve the iron and sulfur reagents, respectively. TOPO was added as an additive and the reaction took place for 2 hours.

Table 2-1. Binding energies, full width at half-maximum (FWHM), and area percentages of various sulfur and iron species detected in the near surface region of pyrite FeS_2 NCs synthesized with and without the TOPO additive.

Near Surface Species – Sulfur:	**Binding Energy (eV):**	**FWHM (eV):**	**NCs with TOPO - Area (%)**	**NCs without TOPO - Area (%)**
S^{2-}	161.2	1.03	9.9	6.3
S_2^{2-}	**162.4**	**1.03**	**67.4**	**76.0**
Polysulfide	163.8	1.03	8.5	7.2
Polysulfide	165.7	1.03	6.7	6.2
SO_4^{2-}	168.0	1.03	7.5	4.3
Near Surface Species – Iron:				
Fe(Ⅱ)S_2	**707.1**	**1.11**	**44.1**	**59.0**
Fe(Ⅱ)S	708.4	0.97	3.3	6.7
Fe(Ⅲ)S	709.8	1.11	7.0	9.7
Fe(Ⅱ)O	*710.4*	*0.96*	*11.2*	*3.7*
Fe(Ⅱ) SO_4	711.0	1.11	6.9	6.7
Fe(Ⅲ)OH	711.1	0.96	19.7	7.2
Fe(Ⅲ)SO_4	712.4	1.11	7.8	7.1

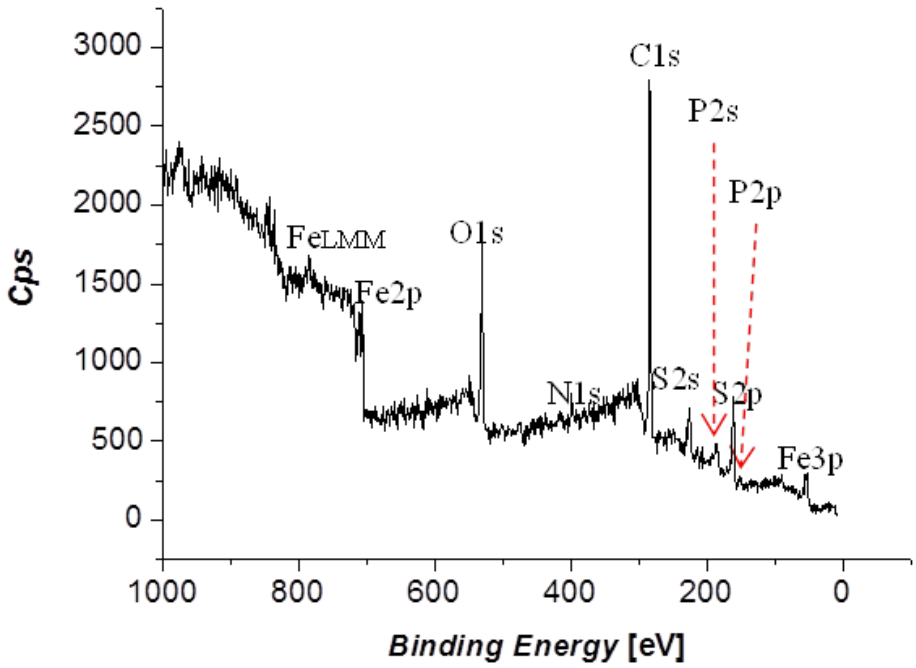

Figure 2-3. The XPS survey scan of FeS_2 NCs synthesized with TOPO additive.

The energy of the valence and conduction band edges and the band gap are critical properties in designing PV device architectures. Here, we used UV-Vis-NIR spectroscopy and CV methods to estimate these parameters. Figure 2-4(a) shows the UV-Vis-NIR absorption spectrum of the synthesized pyrite NCs in chloroform displaying the characteristic pyrite FeS_2 curve reported in the literature [51, 54, 63, 64]. Figure 2-4(b) shows a plot of $(\alpha h\nu)^n$ versus incident photon energy with n = ½ and n = 2 for indirect and direct transitions, respectively. Linear behavior of the curve for n = ½ indicates an indirect E_g of ~1.3 eV, which is higher than the typically reported values of ~0.9-1.1 eV [23, 50, 51, 54, 55, 58, 64]. Direct transitions at ~1.9 eV and ~3.0 eV can be tentatively indexed as interband transitions and agree with approximations in the literature [64]. In order to determine the valence and conduction band edges, E_{VB} and E_{CB}, CV measurements were conducted. An average E_{VB} of -5.6 eV and E_{CB} of -3.9 eV were obtained

and are shown for FeS_2 in the energy diagram in Figure 2-5(a). This E_{VB} agrees with other estimates (-5.4 eV) but the E_{CB} is higher than the value (-4.5 eV) reported in the literature resulting in a larger band gap of ~1.7 eV, which is consistent with the absorption estimate in showing an elevated E_g [50]. The variation in the band gap from the absorption spectra versus the CV data may stem from the fundamental differences in optical versus electrochemical methods. In UV-Vis-NIR absorption measurements, photons with energies greater than or equal to the band gap are absorbed allowing the E_g to be estimated by the onset of absorption. In CV, the onset of oxidation (*i.e.* extraction of electrons from the valence band) and reduction (*i.e.* injection of electrons into the conduction band) are measured to deduce E_{VB} and E_{CB}, respectively, and, thus, E_g. A recent density functional theory (DFT) study showed that alloying pyrite with oxygen can increase its E_g without introducing electronic states within the band gap [59]. This study showed that the E_g of pyrite increased to ~1.2-1.5 eV with a substitutional oxygen concentration of ~10%. Further, in an $FeS_{2-x}O_x$ alloy with x = 1.0, the E_g increased all the way up to 1.88 eV. Based on this DFT study along with the aforementioned XPS results, it is possible that the elevated band gap we observed with absorption and CV measurements may be caused by surface capping of Fe(II) with TOPO ligands or by oxygen alloying.

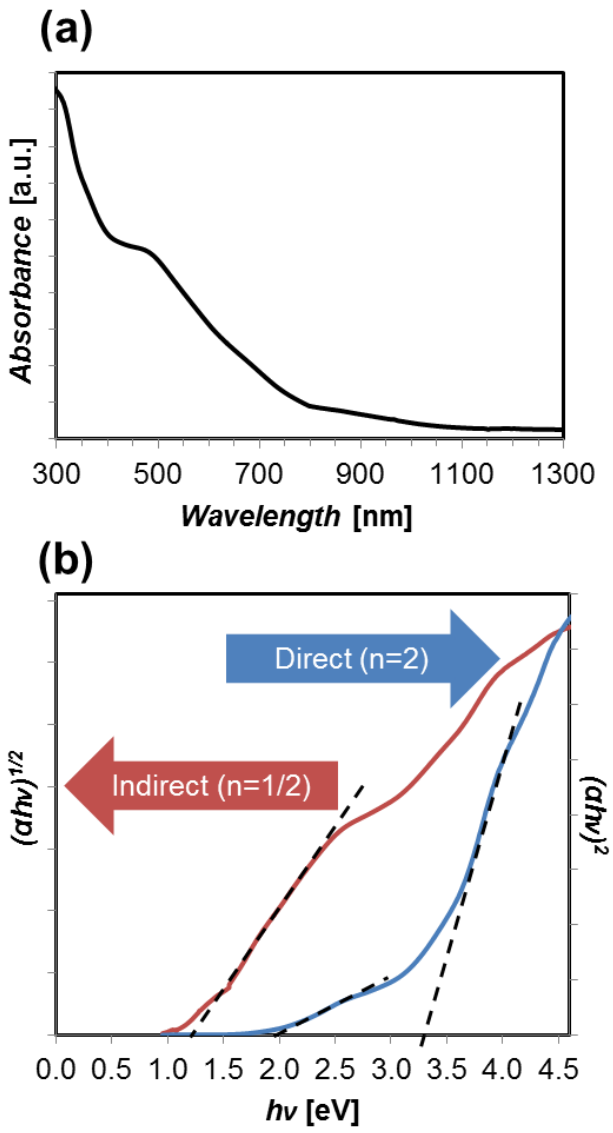

Figure 2-4. a) UV-Vis-NIR absorption spectrum of the pyrite FeS_2 NCs in chloroform. b) Tauc plot showing $(\alpha h\nu)^n$ versus incident photon energy with n = ½ and n = 2 for indirect and direct transitions, respectively. An indirect E_g of ~1.3 eV is estimated from the absorption curve for n = 1/2.

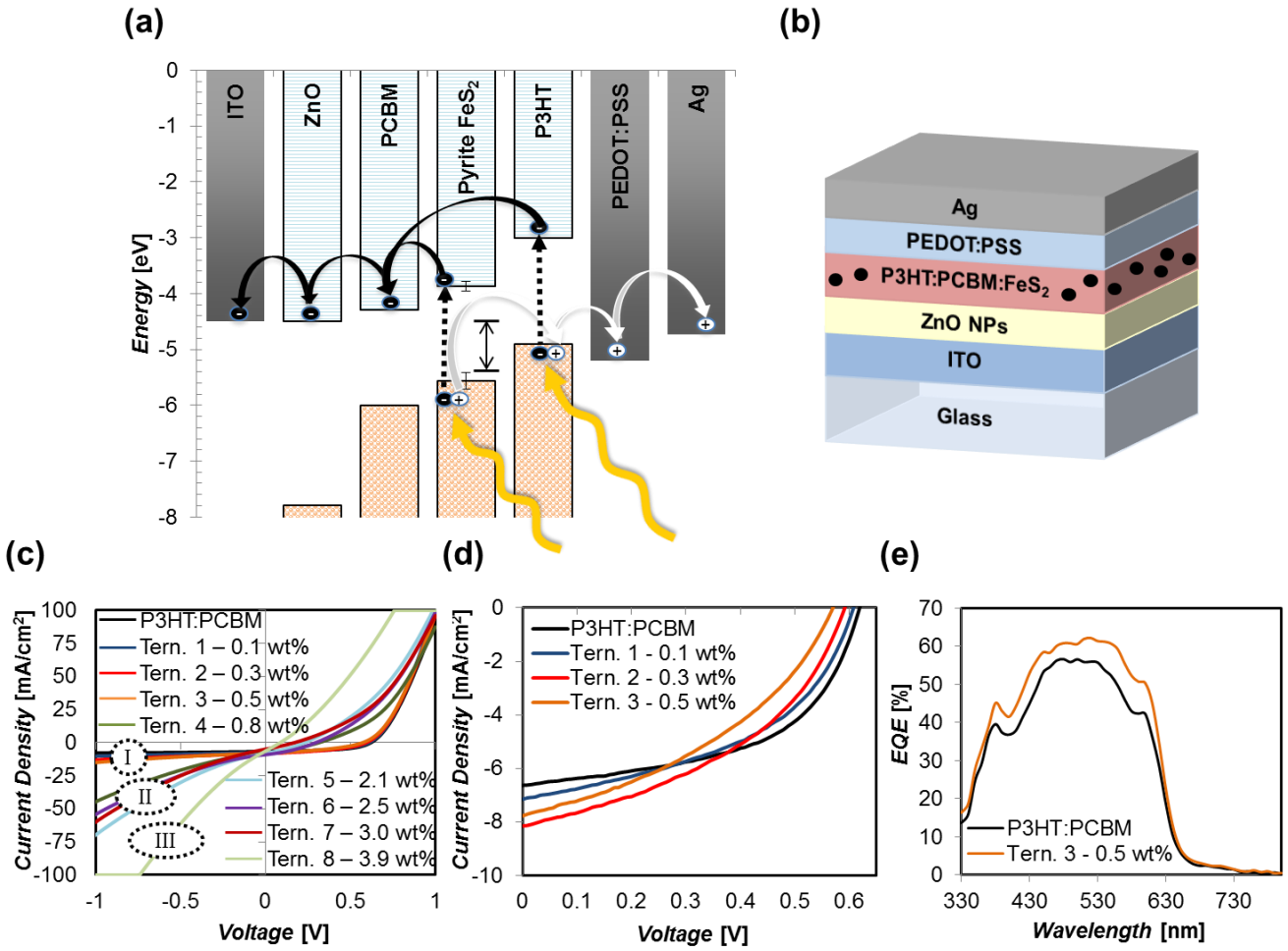

Figure 2-5. a) Energy band diagram of the materials used in the inverted ternary hybrid BHJ solar cell. The average E_{VB} (-5.6 eV) and E_{CB} (-3.9 eV) measured from CV are shown along with error bars. In comparison, the literature values of E_{VB} (-5.4 eV) and E_{CB} (-4.5 eV) are also shown as the short horizontal black lines. b) Schematic of an inverted ternary hybrid BHJ solar cell incorporating pyrite FeS_2 NCs. c) The J-V curves in the voltage range of -1 to +1 V for all ternary devices showing three distinct performance regimes. d) The J-V curves in the voltage range of 0 to +0.6 V for the devices exhibiting "regime I" behavior showing enhanced photocurrents upon addition of FeS_2 NCs. e) EQE spectra of a control P3HT:PCBM device compared to a ternary device with 0.5 wt% FeS_2 NCs**.**

Figure 2-5(b) depicts the architecture of an inverted hybrid ternary BHJ solar cell with the active layer composed of P3HT, PCBM and FeS_2 NCs. The energy band diagram of the layers involved in this device design is shown in Figure 2-5(a). The FeS_2 energy levels estimated from our CV results are indicated in Figure 2-5(a). For comparison, the FeS_2 energy levels corresponding to a smaller E_g as typically reported in the literature are also displayed in the energy band diagram. In addition to estimating the band edges with CV, the reversibility of the oxidation and reduction processes could also be used to indicate whether the semiconductor is p- or n-type [61]. Our CV measurements revealed that oxidation of the FeS_2 NCs was reversible while reduction was irreversible, indicating that the pyrite NCs exhibit p-type behavior [61]. Previous studies also observed p-type character in pyrite FeS_2 NCs [53, 54, 58], differing from the n-type character typically observed in pyrite thin films [23]. In the ternary BHJ active layer, P3HT absorbs light with energy greater than its E_g (*i.e.* 1.9 eV or ~650 nm) [15] which excites an electron from the HOMO to the LUMO creating a coulombically-bound electron-hole pair, or exciton. Pyrite FeS_2 NCs should also absorb light greater than their E_g creating additional charge pairs. Based on the energy band diagram, the excitons from P3HT and FeS_2 could be separated at their interfaces with PCBM to produce free charge carriers. The p-type FeS_2 NCs should act as hole transport pathways, along with P3HT, while PCBM transports electrons. The PEDOT:PSS layer aids in hole collection and the ZnO layer aids in electron collection while also serving to block holes. Both of these buffer layers can help to reduce leakage current through the device. The maximum open circuit voltage (V_{OC}) generated by such a device can be estimated by the difference between the E_{CB} of the electron acceptor and the E_{VB} of the electron donor. The typical V_{OC} of the binary BHJ with P3HT and PCBM is ~0.6 V. According to our CV results, the FeS_2 NCs have a lower E_{VB} than the HOMO of P3HT and could potentially form a $V_{OC} > 1$

V with PCBM. However, the V_{OC} in ternary systems could be pinned to the smallest V_{OC} formed in the blend because the dominant hole transport and collection occurs through the donor component with the highest E_{VB}, i.e. P3HT in this system [65]. Based on this, we would not expect to see the addition of FeS_2 increase the V_{OC} in the ternary devices fabricated here. If the FeS_2 NCs have an E_g congruent with the literature (*i.e.* 0.9-1.1 eV), then they should enhance absorption of the device by capturing lower energy near-infrared (NIR) light that the P3HT cannot absorb. However, as indicated by the short horizontal black bars in Figure 2-5(a), this case would allow FeS_2 to have Type-II band alignment with P3HT but not with PCBM. As a result, only n-type NCs could be expected to enhance performance in that band alignment scenario. According to the E_{VB} and E_{CB} estimated here, these NCs should have Type-II band alignment with P3HT and PCBM. The larger E_g estimated for the NCs in this work would not enhance absorption of NIR light significantly but should still create additional charge carriers. The p-type FeS_2 NCs have been shown to have a much higher carrier mobility than organic or metal oxide semiconductors [53]. Therefore, according to Figure 2-5(a), forming a ternary BHJ by adding p-type pyrite NCs to a P3HT:PCBM blend could enhance photocurrent by increasing charge carrier generation from FeS_2 and could lower series resistance providing additional high-mobility hole-conducting pathways to reach the anode.

We systematically studied the effect of adding FeS_2 NCs in an inverted ternary BHJ on film morphology, charge transport, and the overall device performance. By varying the concentration from 0 to ~4 wt% FeS_2 in the P3HT:PCBM matrix, device performance exhibited three distinct regimes as shown in Figure 2-5(c). The average device performance data of a P3HT:PCBM control device and eight ternary devices with different FeS_2 NC concentrations are summarized in Table 2-2. As mentioned previously, the state-of-the-art inverted devices with

P3HT:PCBM show an average PCE of 4.5% [27, 31]. Note that our PCEs are not optimized to values this high, which is likely due to the choice of chloroform as a solvent, commercially available ZnO NPs, and no interfacial layer modification (e.g. C_{60}-SAMs). Our pyrite FeS_2 NCs were more soluble in chloroform versus others solvents, including chlorobenzene. Therefore, we chose chloroform to maximize the uniform dispersion of the NCs in the blend films while attempting to minimize aggregation. To negate the effects of using this low-boiling point solvent, we thermally annealed all devices to help improve P3HT:PCBM morphology.

Table 2-2. Average device performance of a control binary device and eight ternary devices, with different FeS_2 NC concentrations, tested initially after fabrication (unbolded) and retested after 28 days exposed in air (**bolded**).

Device:	wt% FeS_2:	V_{OC} (V):	J_{SC} (mA/cm^2):	FF (%):	PCE (%):	Max PCE (%):
P3HT:PCBM	0	0.61 +/- 0.00	6.35 +/- 0.24	52.0 +/- 1.1	2.03 +/- 0.11	2.19
P3HT:PCBM - Retest	**0**	**0.59 +/- 0.01**	**7.19 +/- 0.44**	**51.5 +/- 3.7**	**2.18 +/- 0.10**	**2.37**
Tern. 1	0.1	0.60 +/- 0.01	6.84 +/- 0.28	46.1 +/- 0.8	1.90 +/- 0.11	2.02
Tern. 1 – Retest	**0.1**	**0.60 +/- 0.00**	**8.56 +/- 0.04**	**51.7 +/- 0.3**	**2.64 +/- 0.01**	**2.64**
Tern. 2	0.3	0.59 +/- 0.00	7.65 +/- 0.34	42.6 +/- 0.2	1.93 +/- 0.09	2.05
Tern. 2 – Retest	**0.3**	**0.60 +/- 0.01**	**8.65 +/- 0.11**	**53.6 +/- 1.4**	**2.79 +/- 0.11**	**2.89**
Tern. 3	0.5	0.56 +/- 0.01	7.63 +/- 0.26	38.4 +/- 1.0	1.64 +/- 0.08	1.74
Tern. 3 – Retest	**0.5**	**0.60 +/- 0.00**	**8.49 +/- 0.15**	**52.9 +/- 0.3**	**2.71 +/- 0.05**	**2.79**
Tern. 4	0.8	0.29 +/- 0.04	7.31 +/- 0.40	31.3 +/- 1.0	0.66 +/- 0.10	0.78
Tern. 4 – Retest	**0.8**	**0.59 +/- 0.01**	**8.34 +/- 0.07**	**49.2 +/- 0.6**	**2.44 +/- 0.08**	**2.57**
Tern. 5	2.1	0.19 +/- 0.02	7.83 +/- 0.35	29.7 +/- 0.7	0.44 +/- 0.07	0.57
Tern. 5 – Retest	**2.1**	**0.58 +/- 0.00**	**8.44 +/- 0.17**	**47.7 +/- 0.5**	**2.35 +/- 0.05**	**2.44**
Tern. 6	2.5	0.26 +/- 0.02	8.65 +/- 0.40	32.1 +/- 0.9	0.73 +/- 0.12	0.89
Tern. 6 – Retest	**2.5**	**0.58 +/- 0.01**	**8.94 +/- 0.18**	**47.9 +/- 0.7**	**2.48 +/- 0.10**	**2.63**
Tern. 7	3.0	0.15 +/- 0.01	4.88 +/- 0.21	26.7 +/- 0.4	0.19 +/- 0.03	0.23
Tern. 7 – Retest	**3.0**	**0.57 +/- 0.00**	**6.22 +/- 0.21**	**41.2 +/- 0.3**	**1.47 +/- 0.04**	**1.54**
Tern. 8	3.9	0.08 +/- 0.00	6.30 +/- 0.30	25.4 +/- 0.1	0.12 +/- 0.01	0.14
Tern. 8 - Retest	**3.9**	**0.55 +/- 0.01**	**7.71 +/- 0.30**	**42.3 +/- 0.1**	**1.80 +/- 0.10**	**1.92**

In "regime I", FeS_2 NCs were added from 0 to 0.5 wt% and the short-circuit current density (J_{SC}) consistently increased by ~10-20% as shown in Figure 2-5(d) and Table 2-2. However, the photocurrent increase was accompanied by a similar percentage drop in fill factor

(FF) and a small drop in V_{OC} yielding a comparable PCE of ~2% to the control binary device. Increased photocurrent in the devices containing FeS_2 NCs was also observed in the EQE measurements but only in the range of ~370-630 nm (Figure 2-5(e)). It is possible that some of the absorption in this range is from the pyrite NCs but the relatively low NC loading suggests the photocurrent is primarily due to P3HT. An E_g of 1.7 eV could allow photocurrent enhancement up to 730 nm but this was not observed. The normalized UV-Vis-NIR absorption spectra in Figure 2-6 show no significant difference in the range of absorption of the control film versus the ternary films. The J-V curves of the ternary devices were also measured in the dark and with a 720 nm long pass filter (results are not shown here). With the long pass filter in place, the light that reaches the sample does not have enough energy to excite electron-hole pairs in P3HT so any photocurrent coming from the devices under this condition would be due to the charge generated by the FeS_2 NCs. In all cases, the dark curves and long pass filter curves were very similar and no photoactivity of pyrite NCs could be detected in the NIR region. All of these results agree with the larger E_g of the synthesized pyrite NCs obtained from our CV measurements. In regime I, the almost constant V_{OC} indicates that the P3HT:PCBM interfaces still dominate the active BHJ layer. The increased photocurrent with a small addition of FeS_2 suggests that new charge transport pathways could be created due to the improved microstructures of P3HT and PCBM domains or *via* pyrite NCs. Increased photocurrent was observed previously in a conventional P3HT:PCBM:FeS_2 NC solar cell [52]. The pyrite NCs could serve as a medium to improve the interpenetration of PCBM and P3HT domains in the BHJ film leading to enhanced exciton dissociation. Moreover, the well-interpenetrated domains may effectively reduce the series resistance and enhance charge transport. Figure 2-7(a) depicts a possible scenario for a P3HT:PCBM BHJ where charge separation occurs at the P3HT:PCBM

interfaces and the separated charges flow through their respective p-type or n-type materials to the electrodes, travelling most easily through the more crystalline domains of each material. Figure 2-7(b) depicts the idea that a small amount of pyrite NCs in the active BHJ film could improve the microstructures of P3HT and PCBM domains enhancing the P3HT:PCBM interfaces creating increased charge separation and add additional pathways for charge transport, which could reduce the series resistance of the BHJ film and lead to increased photocurrent.

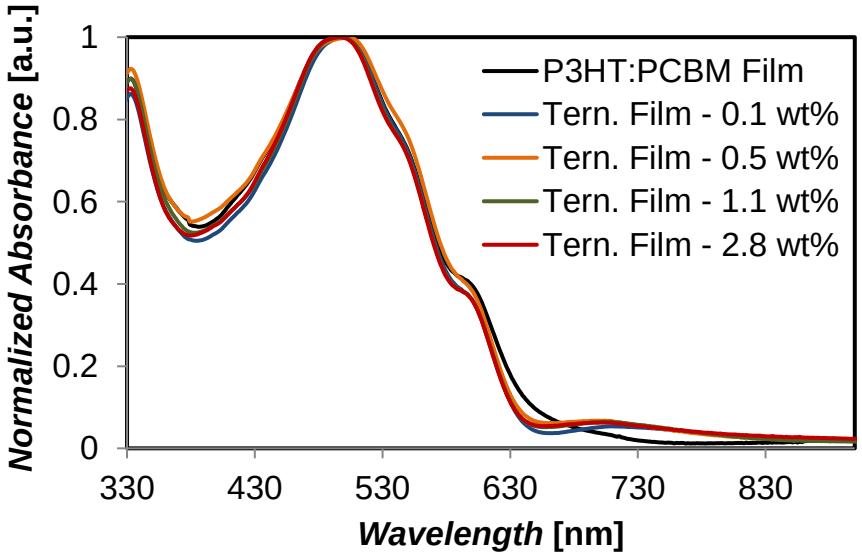

Figure 2-6. UV-Vis-NIR absorption spectra of a control film and various ternary films.

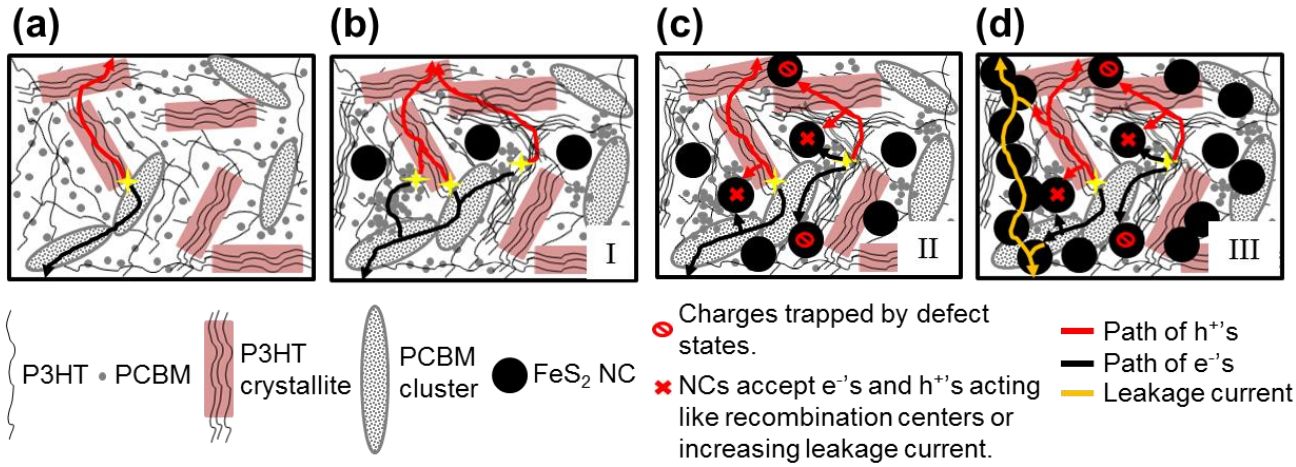

Figure 2-7. Schematics of the microstructures of active BHJ layers and the possible charge transport pathways. a) The control binary P3HT:PCBM layer. b) A ternary BHJ layer in "regime I" with a low loading of FeS_2 NCs. More densely packed P3HT and PCBM domains might be formed, resulting in an enhanced charge separation at P3HT:PCBM interfaces and possibly enhanced charge transport through these domains. c) A ternary BHJ layer in "regime II" where an increased NC loading could adversely affect the device performance likely by a combination of increased leakage current, charge recombination, and/or charge trapping in defect states. d) A ternary BHJ layer in "regime III" where a high NC loading may completely diminish V_{OC} and FF with large leakage current and possible shorting due to NC aggregation.

As the pyrite FeS_2 NC loading was increased from 0.8 to 3 wt%, the J-V curves exhibited an obvious difference in behavior compared to those in regime I. In this "regime II", the photocurrent enhancement continues to be seen, as shown Table 2-2. However, the sharp loss of V_{OC} and FF diminishes the device PCE to less than 1%. The increased photocurrent indicates that charge separation still effectively took place at the P3HT:PCBM and possibly FeS_2:PCBM interfaces and that charge transport was still promoted by the low series resistance via the mechanisms discussed for regime I. The large decrease in both FF and V_{OC} could be due to a high leakage current brought on by the added FeS_2 NCs which leads to a low shunt resistance and loss of rectification. From the band alignment perspective, as shown in Figure 2-5(a), it is possible that excited electrons from P3HT could transfer to FeS_2. Photoluminescence (PL)

spectra taken for various blends are shown in Figure 2-8. A binary film of P3HT:FeS_2 shows obvious quenching over a film of pristine P3HT. This suggests that the excitons formed in P3HT are separated at P3HT:FeS_2 interfaces indicating charge separation or possible charge trapping. While charge separation appears to occur between P3HT and FeS_2, increasing these interfaces appears to be a possible source of lowered shunt resistance. Electron transfer from P3HT to FeS_2 would not be a beneficial occurrence if both materials are p-type, as expected in this system, and could be a source of increased recombination or leakage current. In "regime II", it is possible that the FeS_2 content has increased to where the P3HT:FeS_2 interfacial area emerges to play a more noticeable role. Figure 2-7(c) depicts a possible "regime II" scenario where the slightly increased NC loading still provides enhanced charge transport pathways stemming from morphology enhancement but adversely effects performance likely by a combination of increased leakage current, recombination, and/or some possible charge trapping in defect states.

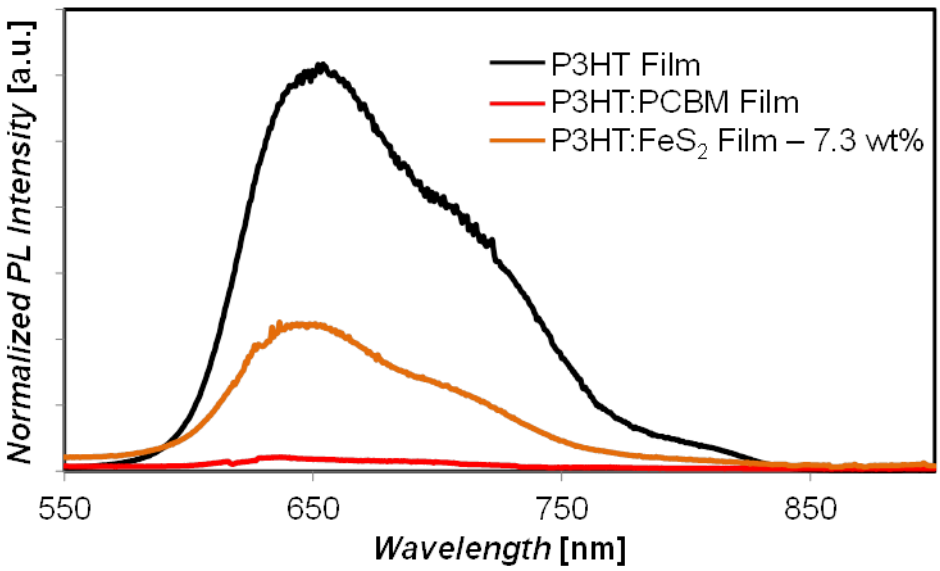

Figure 2-8. PL spectra of pristine P3HT, P3HT:PCBM, and P3HT:FeS_2 NC films.

As the FeS_2 NC concentration was increased above 3 wt%, *i.e.* "regime III", rectification was almost totally lost and the V_{OC} shrank to less than 0.1 V. Even though the P3HT and PCBM concentrations made up more than 96 wt% of the film, the presence of increased amounts of FeS_2 NCs could introduce large enough leakage current to negate the voltage built by charge separation at the P3HT:PCBM interfaces. Large aggregations of FeS_2 NCs were observed all over the surface of this device and even in the electrode areas. These large aggregates could effectively short the active layer through the pyrite networks allowing charges to flow freely to both electrodes under forward and reverse bias. To further investigate whether the aggregation was introduced by post annealing, the ternary active layer with 3.9 wt% pyrite NCs on ITO coated glass was made and SEM images of before and after annealing at 150°C for 10 min were taken. These images (Figure 2-9 (a) and (b)) show the NC aggregates exist both before and after annealing. At high NC loading, these aggregates appear to be sufficiently large to create shorting between the electrodes. Future work should be undertaken to reduce and eliminate the NC aggregates. Nonetheless, the possible microstructure and charge transport pathways in this regime are depicted in Figure 2-7(d).

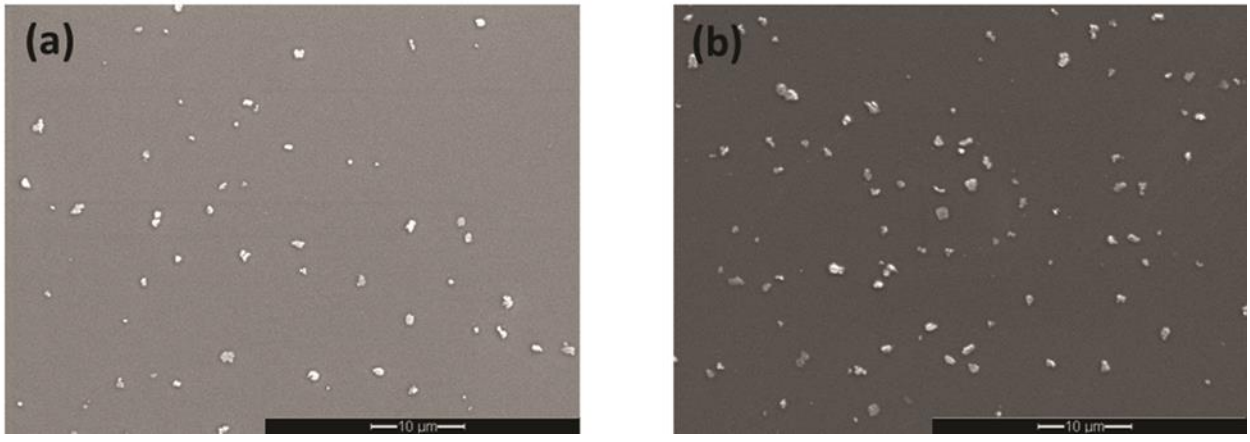

Figure 2-9. SEM images of a ternary thin film with 3.9 wt% FeS_2 loadings with annealing (a) and without annealing (b). Aggregation does not appear to be caused by annealing.

The micro-morphologies of the active layers were investigated further with AFM in tapping mode to reveal the effects from the addition of FeS_2 NCs. The phase and height images of a pristine P3HT:PCBM film and two ternary films with 0.5 and 3.9 wt% NCs are shown in Figure 2-10. Clearly, the films are smoother with the addition of pyrite NCs, suggesting that the P3HT and PCBM domains could intermix more efficiently in the films with FeS_2 NCs. As a result, more P3HT:PCBM interfaces could produce more separated charges and thus more photocurrent. Note that the ternary films show some particles with diameters on the order of 50-100 nm spread around the surfaces. The particles on the surface of the film with 3.9 wt% pyrite NCs are larger and more numerous than those in the film of 0.5 wt% NCs. The micro-morphologies observed in the AFM images support the scenarios proposed for three distinct regimes of device performance with different NC loadings, that is, the addition of pyrite NCs enhances the intermixing of P3HT and PCBM domains but this positive effect could be diminished when the presence of FeS_2 particles or aggregates becomes more dominating.

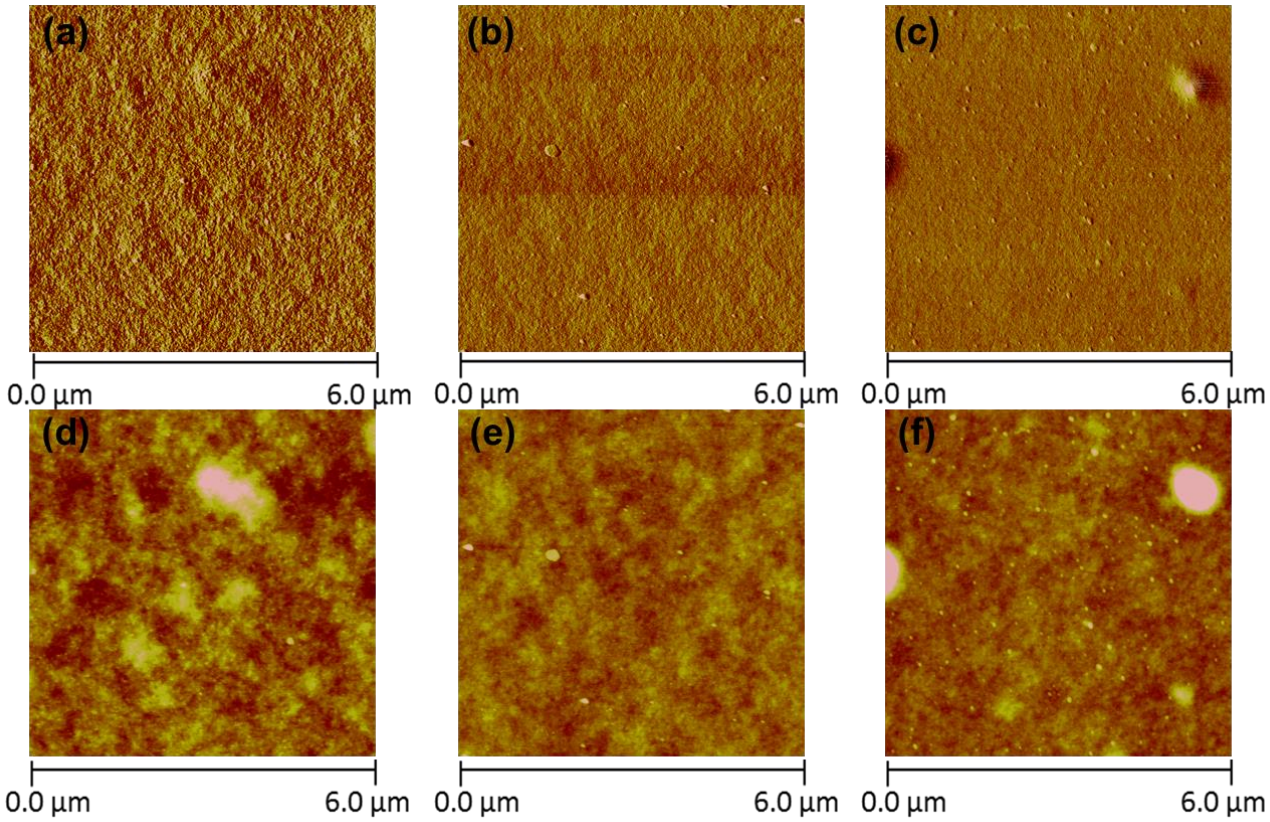

Figure 2-10. AFM phase (a,b,c) and height (d,e,f) images of a P3HT:PCBM film (a,d) and two ternary P3HT:PCBM:FeS_2 NC BHJ films with 0.5 wt% NCs (b,e) and 3.9 wt% NCs (c,f) on ITO coated glass substrates. The vertical scale is 30° in the phase images and 20 nm in the height images.

Lifetime and air-stability are critical to solar cells. As mentioned previously, the inverted architecture is expected to make these devices more stable in air. To test the air-stability of these inverted ternary and binary devices, after taking the initial J-V curve measurements, we left the devices in the glove box with intermittent exposure to air (*i.e.* ~8 hours total) during the first 73 days and then left them completely in air during the next 28 days. The J-V curves measured after intermittent exposure to air (not shown here) showed increased FFs and a V_{OC} back up to the expected 0.6 V for the "regime I" devices only while the control device and all other ternary devices showed no significant change. After an additional 28 days aging in air, all devices not

only showed remarkable stability but also dramatically improved device performance. The bolded values in Table 2-2 and the J-V curves in Figure 2-11(a) show the device performance data of all devices taken after 28 days exposure in air. In contrast to the dramatically decreased V_{OC} and FF initially exhibited by the devices with high pyrite NC loadings, i.e. the "regime II" and "regime III" devices shown in Figure 2-5(c), the V_{OC} and FF of these devices were rejuvenated and the shunt resistance was increased. Figure 2-11(b) shows the J-V curves of the devices with low pyrite NC loadings, *i.e.* the "regime I" devices, before and after air exposure. The PCE of the control device increased from an average 2.03% to an average 2.18% due to the increase of J_{SC} (Table 2-2). This improvement has been attributed to better electronic coherence at the interface of the silver electrode and the PEDOT:PSS layer because of the formation of silver oxide which increases the effective work function of the Ag electrode to -5.0 eV which matches well with the HOMO of PEDOT:PSS [24]. However, no increase in the V_{OC} or FF was observed for the control device. In contrast, all the inverted ternary devices showed increases in V_{OC}, J_{SC}, and FF. The "regime I" devices showed an average percent increase of 3%, 17%, and 25% in their V_{OC}, J_{SC}, and FF, respectively. The PCE of the device with 0.3 wt% FeS_2 NCs increased from an average of 1.93% to 2.79% (Table 2-2). Figure 2-11(b) shows that the initial J_{SC} enhancement due to the addition of FeS_2 NCs is increased further after ageing in air. The restored V_{OC} and improved FF of the "regime II" and "regime III" devices may indicate that the current leakage caused by larger FeS_2 NC particles or aggregates is suppressed as a silver oxide layer forms between the anode and the hole collecting layer. After ageing in air, the best PCE of 2.89% was demonstrated by the inverted ternary device with 0.3 wt% FeS_2 NCs compared to a maximum PCE of 2.37% exhibited by the control device.

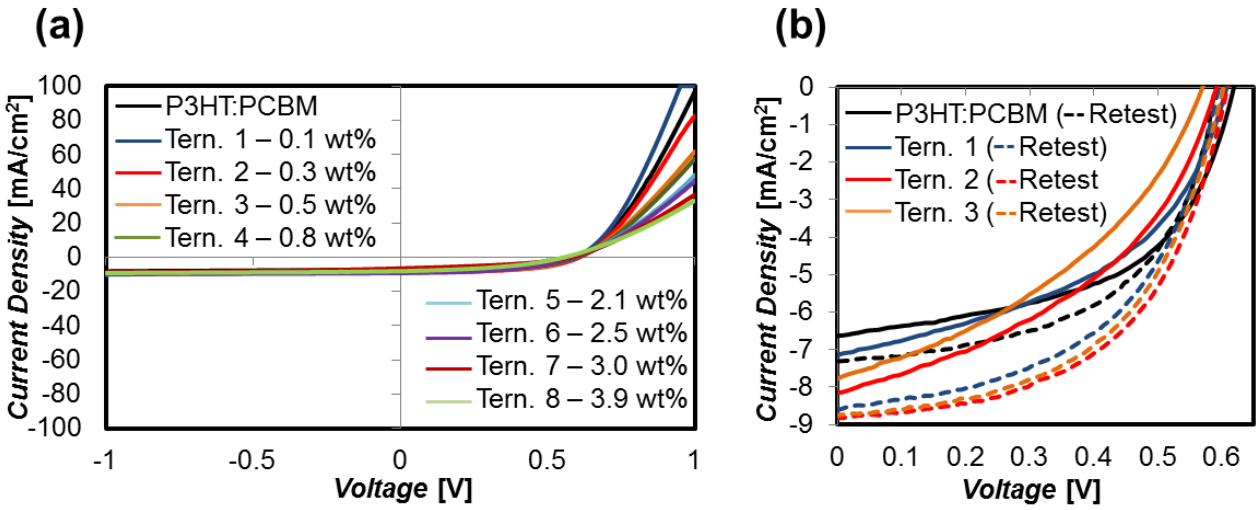

Figure 2-11. (a) The J-V curves in the voltage range of -1 to +1 V from retesting all inverted devices after 28 days exposed in air. (b) Comparison of the J-V curves of the binary control device and the ternary "regime I" devices taken directly after fabrication (solid lines) versus retesting after 28 days exposed in air (dashed lines).

2.4 Conclusions

In conclusion, inverted hybrid ternary BHJ solar cells incorporating pyrite FeS_2 NCs synthesized with TOPO additive demonstrated enhanced short-circuit currents and air-stability with even higher device performance exhibited after 28 days exposure to air. The highest PCE of 2.89% was shown by the inverted ternary device with 0.3 wt% FeS_2 NCs after aging in air compared to a maximum PCE of 2.37% exhibited by the control P3HT:PCBM device. The larger E_g of the pyrite FeS_2 NCs resulted mainly from a raised conduction band edge as shown by the CV measurements which could be due to the capping of surface Fe(II) with TOPO ligands via forming Fe-O bonds or by oxygen alloying of bulk iron atoms in the NCs. This speculation was partly supported by our XPS measurements of the as-synthesized pyrite NCs which showed a much greater presence of oxygen species on the NC surfaces and in the "bulk" versus NCs synthesized without the TOPO additive. The increased photocurrent observed in the inverted ternary devices with low concentrations of pyrite NCs was consistently obtained as the NCs

enhanced the molecular packing and morphology of the film increasing charge generation and transport in the organic phases or via pyrite NCs. The improved J_{SC}, FF and V_{OC} of the inverted ternary BHJ devices after aging in air is attributed to the inverted structure and likely stems from the formation of silver oxide at the interface between the top electrode and the PEDOT:PSS layer which improves the electronic coherence between these two layers and reduces the leakage current caused by pyrite NC aggregates. Further work is required to optimize ligand preference while preventing aggregation in polymer blends and to explore oxygen alloying to control the E_g and trap state formation. The photocurrent enhancement and air-stability demonstrated by this inverted design offer a promising architecture for future FeS_2 NC-based devices. Furthermore, the investigation of the NC structure, chemical state and band edges presented here provides insight to advance the development of pyrite FeS_2 NCs as a cheap, non-toxic PV material for sustainable energy. While pyrite FeS_2-based solar cells have not demonstrated high PCEs, its potential advantages as a low-cost, earth abundant and non-toxic material for solar energy warrants continued research efforts.

CHAPTER 3. HIGH EFFICIENCY PTB7-BASED INVERTED ORGANIC PHOTOVOLTAICS ON NANO-RIDGED AND PLANAR ZINC OXIDE ELECTRON TRANSPORT LAYERS

3.1 Introduction

Organic photovoltaic cells (OPVs) with the inverted structure have been of peak interest in recent years due, in part, to better ambient stability and device processing advantages. In inverted devices, it is important to prepare a selective bottom cathode to effectively reverse the device polarity from a conventional to an inverted structure.[25, 26] This is typically achieved by forming an electron transport layer (ETL) on indium tin oxide (ITO). This ETL should have good optical transparency, low resistivity for electron conduction, and an appropriate conduction band (CB) level and bandgap (E_g) for high selectivity of electrons while also blocking holes. Various wide bandgap, n-type metal oxides, such as TiO_2, ZnO, Cs_2CO_3, and certain polyelectrolytes with a large dipole moment have been successfully deployed as interfacial ETLs in inverted devices.[14, 24, 26, 28, 29] Additionally, varied forms of layer nanostructuring, surface treatment, and processing additives have been explored to improve charge collection efficiency, transport and selectivity.[30-33]

ZnO has drawn much attention as an ETL as it has high transparency in the visible region (E_g = ~3.3 eV)[26, 66-68], good electron mobility, proper energy level alignment with fullerene acceptors[68], environmental stability, low cost and is easily deposited via various solution processes.[25] This ease of processing and relative material abundance also makes ZnO a good candidate for large scale manufacturing. Good operational stability of inverted OPVs with ZnO

ETLs has also been noted and attributed to the fact that ZnO blocks UV light resulting in negligible UV-light-induced photodegradation of organic materials.[25]

Inverted devices can use ZnO films processed by various methods including atomic layer deposition (ALD) [69], sputtering [70], depositing pre-synthesized nanoparticles [24, 71] and sol gel techniques [24, 28, 33, 69]. Sol gel techniques can be advantageous because they are solution based, unlike ALD or sputtering, and do not involve the more complex synthesis steps required with nanoparticles. Additionally, metal oxide nanoparticles may form more porous and poorly interconnected particulate films at low processing temperatures.[28] Sol gel techniques are often used with widely ranging baking conditions to create dense and pin-hole free ZnO films with varying degrees of crystallinity.[26, 67, 72] For sol gel methods, the choice of precursor materials, concentration, spin coating speed, drying and baking steps all affect the optical, electrical, and structural properties of the films.[67] Interestingly, the morphology of sol-gel derived ZnO ETLs can be controlled to form a planar or a nano-ridged structure simply by static or dynamic (i.e. ramped-up) baking conditions, respectively.[28, 33]

Nano-ridged and planar ZnO structures were deployed in inverted devices using the P3HT:$PC_{61}BM$ BHJ active layer exhibiting a PCE as high as 4.0% for the dynamically baked devices versus 3.2% for the statically baked ones.[33] A high FF increase was observed while V_{OC} and J_{SC} stayed almost the same. This was attributed, in part, to lower current leakage and better charge selectivity due to a more densely packed ZnO film for the nano-ridged versus the planar morphologies stemming from the slower heating process. By comparing P3HT:ZnO bilayer devices, a large J_{SC} increase was observed with the nano-ridged structure indicating more interfacial area for charge separation also plays a role in the improvement. Both the dynamically and statically baked ZnO films were prepared using a precursor concentration of 0.75 M, spin

speed of 2000 rpm, and a baking temperature of 275°C. The dynamically baked films used a ramp rate of 50°C/min to make ZnO nano-ridges.

In another study, sol gel-derived ZnO films were dynamically and statically baked at a lower temperature (200˚C) and the spin coating time was varied to analyze both morphology and internal nanocrystal (NC) orientation.[28] A precursor concentration of 0.45 M and spin speed of 4000 rpm were used. Static baking was observed to create higher (002) plane NC orientation which is known to enhance lateral charge transport parallel to the device substrate. Dynamic baking created a more random crystal orientation that tended to support charge transport perpendicular to the substrate benefitting overall charge transport. Due to the experimental conditions, the formation of nano-ridges was only observed with dynamic baking (ramp rate of 50˚C/min) and a short 15s spin coat duration. Dynamically baked films spun for 60 seconds showed a more planar and granular morphology. Similar to the previous work, the dynamically baked nano-ridged structure showed the best performance due primarily to an increased FF and shunt resistance (R_{SH}). The best P3HT:PC_{61}BM device showed a PCE of 3.59% and the device based on a BHJ containing a low band gap polymer (PTB7-F20) blended with PC_{71}BM achieved a PCE as high as 6.42%.[28]

It is apparent from the works referenced above that ETL morphology and properties are highly dependent on the specific combination of conditions used for the sol gel method. Significant changes in ZnO morphology can also affect the overlying active layer coating quality. This is often overlooked as the active layer conditions are held constant for different ETL morphologies and conditions in the previous studies. Thus, it is important to check the optical field distribution throughout the device as the ETL changes and to actively optimize the

BHJ layer conditions in order to achieve the optimal device performance as the underlying morphology changes.

Large leaps in OPV efficiency have been realized in recent years through the development of low band gap semiconducting polymers, such as PTB7.[38] High efficiency inverted devices using a BHJ of PTB7:$PC_{71}BM$ have shown improvement with fine control and treatment of the bottom ETL and the top hole collecting layers reaching PCEs exceeding 8%.[14, 30] However, it is often seen in the literature that the control devices using sol gel ZnO and PTB7:$PC_{71}BM$ active layers only achieve PCEs in the 5-7% range.[68, 73] Experimental conditions may vary widely leading to a broad range in performance between very similar devices in the literature. Therefore, in high efficiency systems, it is especially important to ensure that control devices are fully optimized in order to illuminate the full benefits that newly engineered modifications (e.g. surface treatments, additives, nanostructuring, etc.) can provide.

In this chapter, the ZnO ETL morphology was controlled and studied for optimization in high efficiency inverted OPVs based on the PTB7:$PC_{71}BM$ BHJ. The sol gel precursor concentration, spin coating speed and baking conditions were used to simultaneously control the film thickness and morphology of ZnO films. The optical properties for each condition were measured and used in transfer matrix method (TMM) calculations to evaluate their effect on device performance. The calculated optical field distributions for completed devices are discussed in conjunction with the measured ZnO morphology and thicknesses and active layer conditions. The average PCE for planar and nano-ridged ZnO films of varied thickness was consistently high at 7.65-8.01% for all conditions, in contrast to other studies, with a maximum PCE reaching 8.32%. This insensitivity of device performance to ZnO variations is discussed in the context of the small domain microstructures of the PTB7:$PC_{71}BM$ active layer as well as the

rapid intramolecular charge separation and highly efficient photovoltaic function of PTB7. In addition, the need for fine control of the active layer thickness as underlying ZnO layer morphology changes is highlighted as the primary variable for achieving high performance.

3.2 Experimental

3.2.1 Film and Device Fabrication

The ZnO sol-gel solution was prepared by dissolving zinc acetate dihydrate ($Zn(CH_3COO)_2 \cdot 2H_2O$, Sigma-Aldrich, >99.0%, 1 g for 0.44 M, 0.5 g for 0.54 M) and ethanolamine ($NH_2CH_2CH_2OH$, Sigma-Aldrich, >99.5%, 0.277 mL for 0.44 M, 0.1375 mL for 0.54 M) in 2-methoxyethanol ($CH_3OCH_2CH_2OH$, Sigma-Aldrich, 99.8%, anhydrous, 10 mL for 0.4 4M, 4.1 mL for 0.54 M) under vigorous stirring for greater than 12 h. ITO-coated glass substrates were used for all films and devices and were first cleaned by ultrasonication in soapy deionized (DI) water, DI water, acetone, and isopropanol. The substrates were treated with oxygen plasma prior to depositing any films. The ZnO solutions were then spin-cast on top of the pre-cleaned ITO-glass substrates at either 2000 or 4000 rpm for 60 s. These samples were then annealed at 200°C for 1 hour under dynamic or static conditions. For static baking, the substrates were placed directly on a hot plate at 200°C and baked for 1 hour. For dynamic baking, the substrates sat at room temperature for 10-15 minutes and were then placed on a hot plate at room temperature which was ramped to 200°C over 1 minute, after which the substrates were baked for 1 hour. A PTB7 solution (1-Material, Inc.; 20.7 mg/mL) and a $PC_{71}BM$ solution (Nano-C; 31.0 mg/mL) in chlorobenzene were each made in a N_2-filled glovebox and stirred overnight at 60°C. Then these solutions were mixed with a polymer:fullerene ratio of 1.5:1 with 3.0 vol% 1,8-diiodooctane and allowed to stir for >1 hour. The mixed solution was then cooled to room temperature and filtered with a 0.2 μm PTFE filter. The cooled filtered solution was

spincast on top of the ZnO films at varied rpms for 60 s. Then, the active layer coated substrates were loaded in a vacuum chamber (<10^{-6} Torr) where a 10 nm film of MoO_3 and 100 nm film of Ag was deposited through a shadow mask by thermal evaporation. Each substrate had 4 pixels with defined areas of 10 mm^2 each.

3.2.2 Film and Device Characterization

Morphology images of the ZnO films and on top of the MoO_3 layer but outside the electrode area of the finished devices were taken by AFM in tapping mode (Bruker/Veeco/DI Multimode AFM-2). The thickness of the active layers on bare ITO glass was measured by profilometry (KLA Tencor Alpha-Step 500). UV-Vis-NIR absorption spectra of ZnO films were obtained using a Perkin Elmer Lambda 900 UV-Vis-NIR absorption spectrometer.

The refractive index, extinction coefficients, and thicknesses of the various ZnO films and of the other layers in the devices were measured with spectroscopic ellipsometry (J.A. Woollam Co., Inc. α-SE Spectroscopic Ellipsometer, CompleteEASE software). All ZnO films of the various conditions were made on glass/ITO substrates for characterization with ellipsometry, AFM, and absorption spectroscopy. Ellipsometry measurements were first made on bare glass (Corning XG) and then on bare glass/ITO substrates in order to build the optical models for these substrates. The Cauchy dispersion relation was used to model the optical parameters of the bare glass substrates. An index-graded layer was used to model the optical properties of the ITO layers, which is typical, along with the known ITO thickness from the substrate manufacturer. The parameters for the glass and ITO layers were held constant as the parameters were calculated for the overlying ZnO layers. Black tape was applied to the backside of the glass for all samples to eliminate errors from backside reflections. The depolarization was ensured to be near zero for all measurements indicating that little light is reflected from the

backside into the detector. The ZnO optical parameters were found using a B-Spline fit which works well for materials that are partially transparent and partially absorbing. The fit parameters were ensured to be physical by ensuring that k was greater than or equal to zero, assuming a transparent region and band gap of 3.3 eV (i.e. the band gap of ZnO), and maintaining Kramers-Kronig consistency between the e1 and e2 spline curves. An effective roughness layer was added to the models to account for non-idealities due to surface roughness features. The root mean squared error values were ensured to be less than 20 which is reasonable for samples with much structure and oscillation in the measured data.

Current-voltage measurements for all inverted devices were conducted in a glove box under nitrogen atmosphere using a Keithley 2400 Source Meter and a solar simulator with a Solar Light Co. Xenon lamp (16S-300W) and an AM 1.5 filter. The light intensity was calibrated to 100 mW/cm^2 using a calibrated silicon solar cell that had been previously standardized at the National Renewable Energy Laboratory. EQE measurements were gathered in air using an Oriel Xenon lamp (450W) with an AM1.5 filter, a monochromator (Oriel Cornerstone 130 1/8 m), and a lock-in amplifier (Stanford Research Systems).

3.2.3 Optical Modeling

The transfer matrix method (TMM) was used to calculate the optical field distribution within devices and to estimate the potential photocurrent produced in the active layer.[74] TMM calculates the interference of reflected and transmitted light waves at each interface in the stack based on each materials optical properties as represented by their complex refractive index ($\tilde{n} = n + ik$). The refractive indices (n) and extinction coefficients (k) of the various layers used in the models were measured with spectroscopic ellipsometry. The TMM calculations were run based on the device architectures discussed using the film thickness, n, and k that were measured for

each ZnO film. The TMM calculations assume planar layer interfaces and isotropy for all the films. The interference is assumed incoherent within the glass substrates because their thicknesses (1.1 mm) are much higher than the wavelengths of the simulated incident light.

3.3 Results and Discussion

3.3.1 Morphology and Optical Properties of ZnO Films with Varied Processing Conditions

ZnO films were prepared using the sol gel method with different precursor concentrations, spin coating speeds and baking conditions. As seen in Table 3-1, ZnO film thickness was steadily increased as the precursor concentration was increased while fixing the spin coating speed or as the spin coating speed was decreased while fixing the precursor concentration. ZnO nano-ridges are clearly observed when using the dynamic baking condition. For each combination, the average film thickness of the nano-ridged and planar ZnO films is approximately the same while the roughness of the nano-ridged samples is expectedly higher. The average film thickness varies from 40-64 nm for all the conditions used here. For dynamically baked ZnO thin films, the spin coating speed and precursor concentration not only alter the film thickness but also the height and density of the nano-ridges themselves as shown in the AFM topography images in Fig. 3-1(a) and (b). For films from the 0.54 M precursor solution, the nano-ridges spin coated at 2000 rpm are significantly taller (e.g. peaks up to ~70 nm) than those spin coated at 4000 rpm (e.g. peaks up to ~38 nm). This is clearly shown in the cross-sectional topography graphs in Fig. 1(e) and (f) and reflected in the measured root mean square (RMS) roughness values of 12.80 nm vs. 8.83 nm (Table 3-1). The valley-to-valley distance between the nano-ridges averaged ~650 nm for the films spun at 2000 rpm and ~370 nm for those spun at 4000 rpm. The same trend was observed for dynamically baked films made from the 0.44 M precursor solution. Conversely, the statically baked films show similar planar

morphologies (Fig. 3-1(c) and (d)) for all precursor concentrations and spin coating speeds but vary primarily in film thickness (Table 3-1). Film surface roughness varies with the precursor concentration even at the same spin speed. RMS roughness values varied with solution concentration by up to ~0.8 nm for the static films and ~1.1 nm for the dynamic films.

Table 3-1. The film number, ZnO precursor solution concentration, spin coating speed and baking condition with the resulting film thickness as determined by spectroscopic ellipsometry and root mean square (RMS) roughness (Rq) from AFM.

Film #	ZnO Precursor Concentration (M)	Spin Speed (rpm)	Bake Condition	Film Thickness (nm)	R_q (nm)
1S	0.44	4000	Static	42	4.16
1D	0.44	4000	Dynamic	40	7.76
2S	0.54	4000	Static	48	3.40
2D	0.54	4000	Dynamic	47	8.83
3S	0.44	2000	Static	52	3.00
3D	0.44	2000	Dynamic	55	13.30
4S	0.54	2000	Static	62	2.59
4D	0.54	2000	Dynamic	64	12.80

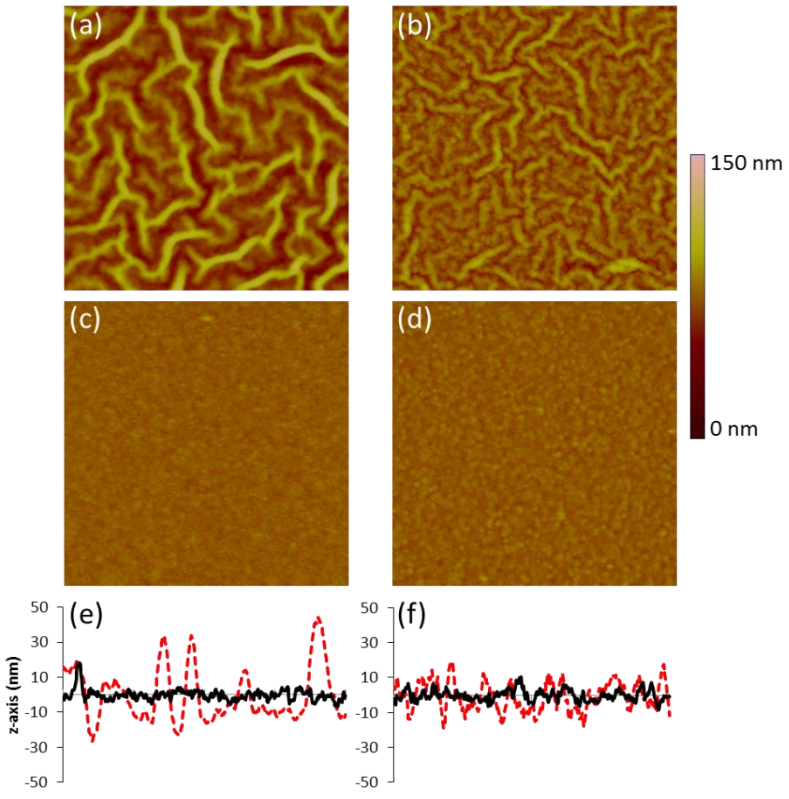

Figure 3-1. Tapping mode AFM topography images (5 µm x 5 µm) of ZnO sol gel films with processing conditions (a) 2000 rpm, dynamic bake; (b) 4000 rpm, dynamic bake; (c) 2000 rpm, static bake; (d) 4000 rpm, static bake. Height scale for all is 150 nm. All images are for films made with a precursor sol gel solution concentration of 0.54 M. (e) and (f) Line profile of a 4 µm trace measured across (a, c) and (b, d), respectively. The red dotted lines are the cross sections of (a) and (b), respectively. The solid black lines are the cross sections of (c) and (d), respectively.

The optical properties of the ZnO thin films were investigated using UV-Vis-NIR absorption spectroscopy and spectroscopic ellipsometry. The films are highly transparent in the visible region above 400 nm and an onset of absorption is near the band gap of ZnO at ~370 nm, as seen in Fig. 3-2.[26] Additional light scattering is apparent for the nano-ridged film due to increased surface roughness.

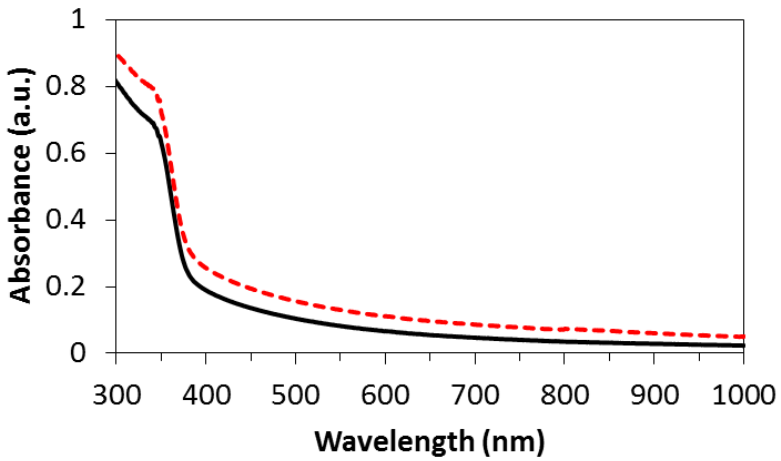

Figure 3-2. Absorbance of statically baked (black solid line) and dynamically baked (red dotted line) ZnO films on glass (i.e. films #2S and 2D, respectively).

Figure 3-3 shows the refractive indices (n) of the ZnO films prepared under the different conditions listed in Table 3-1. The refractive index of these films varies from approximately 1.6-1.85 in the visible region. For statically baked films, those spun at 4000 rpm (i.e. films #1S and 2S) show a very similar refractive index of ~1.66 at 600 nm, as do those spun at 2000 rpm (i.e. films #3S and 4S) with ~1.63 at 600 nm. Although a higher precursor concentration can result in a thicker film under the same spin coating speed, the refractive indices of these films are similar. The slightly higher refractive indices of films produced at the higher spin coating speed could be due to the high packing density of the film caused by the higher compacting force during the spin process. For the dynamically baked films, a similar trend of spin coating speed on the refractive index was observed. The ZnO films with smaller nano-ridges produced by spin coating at 4000 rpm (i.e. films #1D and 2D) show higher refractive indices of 1.74-1.77 at 600 nm compared to those with larger nano-ridges produced by spin coating at 2000 rpm (i.e. films #3D and 4D) with 1.66-1.72 at 600 nm. Unlike the insensitivity to the precursor concentration for films prepared under the static baking conditions, the refractive indices of these nano-ridged films changes

significantly with the precursor concentration at the same spin coating speed. The presence of residual solvent molecules in the precursor films and a slower solvent drying rate facilitate the formation of nano-ridges.[28] The slower drying rate caused by the dynamic baking process amplifies the effects of varied solution concentration on the film morphology and packing and thereby the refractive index. The crystallinity of thin films can also affect their refractive indices. The crystallization of ZnO in the films prepared by this sol gel method begins at 200-300°C.[67] Formation of highly crystalline ZnO films requires baking at high temperatures of 450-800°C.[66, 67, 72, 75] Yang et al. observed the X-ray diffraction (XRD) peaks corresponding to the (100), (002) and (101) crystal planes of ZnO with sol-gel derived films baked at 500°C on SiO_2 substrates.[25] However, these peaks were not observed for the same films baked at 200°C and the films were ascribed to having composite amorphous character. Park et al. also made sol-gel derived ZnO films baked at 200°C on silicon (100) substrates and only faintly observed these crystalline peaks.[28] Since all the films produced in this work were baked at 200°C for 1 hour, the crystallinity should be similar. Therefore, the refractive index variations could mainly be due to the difference in morphology and packing density of each film.

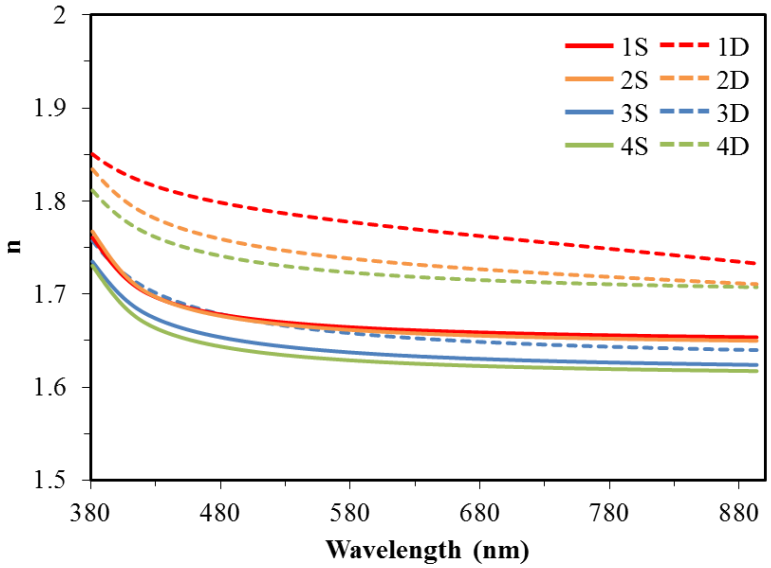

Figure 3-3. The refractive indices for various statically baked (solid lines) and dynamically baked (dotted lines) ZnO films with different thicknesses and morphologies. The film numbers in the legend correspond to the films listed in Table 3-1.

With the sol gel method, the heat treatment conditions affect the vaporization of the solvents, the decomposition of zinc acetate and the crystallization of ZnO which in turn affect the structural relaxation of the gel film and the optical properties of the film. Therefore, the refractive index of ZnO films varies with both the baking conditions and the chosen solvents and precursors.[67] The index of refraction of a material is related to its density and may be lowered by non-scattering porosity.[76] Based on the measured refractive indices, calculation of the relative density of these films showed that, for both static and dynamic baking, the 4000 rpm condition provides denser films (see Table 3-2).[67, 76] Additionally, the dynamically baked films show higher relative densities than the statically baked ones suggesting that the slower drying condition leads to structural relaxation and more densely packed ZnO films.

Table 3-2. Refractive indices (at 600 nm) and calculated relative densities of the various ZnO films.

Film #	Spin Speed (rpm)	Conc. (M)	n	Rel. Dens. (%)
1S	4k	0.44	1.663	58.9
2S	4k	0.54	1.660	58.5
3S	2k	0.44	1.635	55.8
4S	2k	0.54	1.627	54.9
1D	4k	0.44	1.774	71.6
2D	4k	0.54	1.735	67.0
3D	2k	0.44	1.656	58.1
4D	2k	0.54	1.721	65.4

3.3.2 Characterization and Optical Modeling for Devices with Statically Baked ZnO ETL

The ZnO films prepared by varied conditions listed in Table 3-1 were deployed in inverted OPVs using the PTB7:$PC_{71}BM$ active layer. Figure 3-4 shows a schematic of the OPV device structure and the current-voltage curves for such devices with statically baked (i.e. planar) ZnO films made with 0.44 and 0.54 M concentrations at 2000 and 4000 rpm. The film thickness and RMS roughness of films prepared under these conditions are listed in Table 3-1. The surface roughness increases slightly as the film thickness decreases. The performance parameters of these devices are summarized in Table 3-3. The average active layer film thickness for these devices is ~94 nm. The devices with planar ZnO films all behaved very similarly even as the ZnO thickness increased from ~42 to ~62 nm. The J_{SC} for these devices was approximately the same with averages ranging from 14.17 to 14.50 mA/cm^2. The V_{OC}'s and FF's were also very consistent for these devices averaging 0.75 V and 72.3-73.4%, respectively, resulting in repeatably high PCE's averaging 7.65-8.01% with a maximum of 8.32% observed. The consistently high performance is shown in Fig. 3-4 as the curves of the best devices for each statically baked ZnO condition are essentially the same. This consistently high performance

occurs in spite of the small drop in refractive index between the 1S and 2S versus the 3S and 4S ZnO films mentioned earlier. Thus, the thickness and small roughness variations in these planar ZnO films do not significantly affect the performance of these inverted OPV devices.

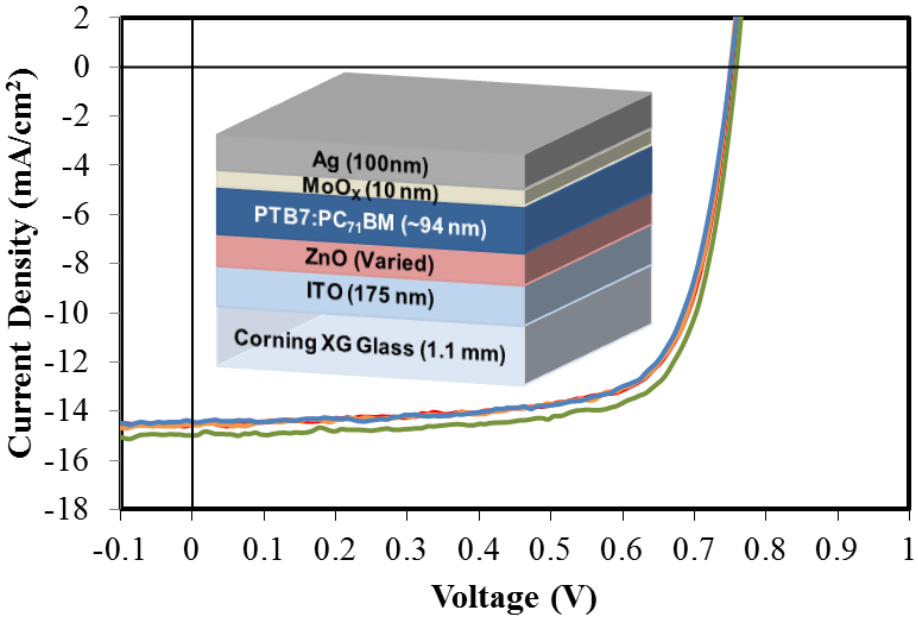

Figure 3-4. J-V curves for organic solar cells with statically baked ZnO layers corresponding to films # 1S (red), 2S (orange), 3S (blue), and 4S (green) in Table 3-1. The inset shows a schematic of the device.

Table 3-3. Average parameters of the inverted OPV devices with statically baked ZnO films indicated by the film numbers listed in Table 3-1.

ZnO Film	V_{OC} (V)	FF (%)	J_{SC} (mA/cm^2)	PCE (%)	PCE_{max} (%)
1S	0.75 +/- 0.00	72.7 +/- 0.5	14.44 +/- 0.25	7.83 +/- 0.15	7.99
2S	0.75 +/- 0.01	72.6 +/- 0.5	14.19 +/- 0.39	7.70 +/- 0.23	7.96
3S	0.75 +/- 0.00	72.3 +/- 0.4	14.17 +/- 0.44	7.65 +/- 0.26	7.92
4S	0.75 +/- 0.00	73.4 +/- 0.6	14.50 +/- 0.28	8.01 +/- 0.19	8.32

TMM calculations were performed to explore the effect of different ZnO films prepared under statically baked conditions on the optical distribution and charge generation in devices. Figure 3-5 shows the TMM calculations of the device J_{SC} as a function of the ZnO film thickness for films made under static baking as well as a function of the active layer thickness. The refractive index of each ZnO film was experimentally measured, shown in Fig. 3-3, and used in the TMM simulations. The difference in ZnO films makes a relatively larger impact on J_{SC} for devices with thinner active layers but is still within ~0.5 mA/cm^2. The thickness of the planar ZnO films in the devices is in the range of approximately 42 to 62 nm. Within this range, Figure 3-5 shows the calculated J_{SC} varies from 14.7 to 15.1 mA/cm^2 for a 94 nm active layer (i.e. the approximate PTB7:$PC_{71}BM$ thickness of devices in Fig. 3-4), which is close to the experimental J_{SC}. Figure 3-5 shows that both the ZnO and the active layer thicknesses require simultaneous optimization to achieve maximum photocurrent.

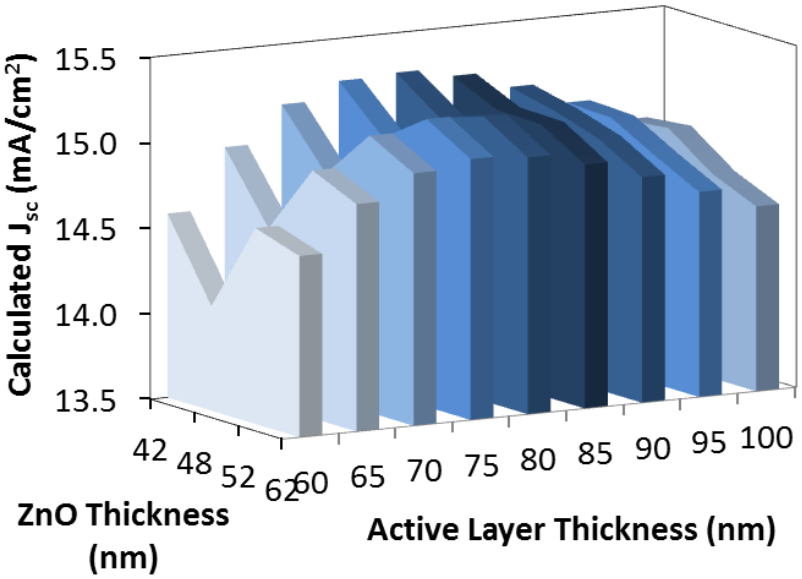

Figure 3-5. TMM calculations showing the change in J_{SC} versus thickness of statically baked ZnO and active layers.

Device performance independent of film thickness for planar ZnO films was also observed in the study of inverted BHJ devices with the P3HT:$PC_{61}BM$ active layer.[69] As an ETL, the ZnO film should completely cover the ITO electrode to prevent current leakage. Once complete coverage is achieved, the thickness of the film has little effect on performance regardless of whether the active layer is P3HT:$PC_{61}BM$ or PTB7:$PC_{71}BM$. However, the surface roughness of ZnO films affects the device performance in different ways when the active layer is P3HT:$PC_{61}BM$ versus PTB7:$PC_{71}BM$. For P3HT:$PC_{61}BM$ BHJ devices, the increase of surface roughness from 2.86 to 4.02 nm resulted in the decrease of FF from 56 to 44%, accompanied by the increase of series resistance (R_S) from 10.7 to 31.7 Ω cm^2.[69] It was suggested that a rougher ZnO film surface could induce more small voids between the P3HT:$PC_{61}BM$ active layer and the ZnO layer. In contrast, a consistently high FF of 72.3-73.4% was displayed in our devices regardless of the roughness variation from 2.59 to 4.16 nm among the four statically baked ZnO films. This may be due to differences in the microstructure and other properties of the PTB7:$PC_{71}BM$ system compared to the P3HT:$PC_{61}BM$ system. For example, the P3HT:$PC_{61}BM$ system has optimal performance with a microstructure consisting of large and highly crystalline polymer domains that have distinct phase separation with PCBM. This type of BHJ relies on increased carrier mobility within the crystalline polymer domains and higher order for better connected charge transport pathways to counterbalance its less efficient photovoltaic function.[77] The PTB7:$PC_{71}BM$ BHJ, on the other hand, is a largely amorphous film with single polymer strands connecting multiple small separate crystalline domains and a relatively high PCBM content to ensure a continuous acceptor network for efficient charge collection.[77] This morphology combined with significant intramolecular charge separation due to PTB7's in-chain donor-acceptor copolymer structure creates rapid charge separation and highly efficient

photovoltaic function.[77] Thus, these smaller domains and the higher intrinsic PV function of the PTB7-based system appear to desensitize these devices to small roughness variations in the underlying ZnO films.

3.3.3 Characterization of Devices with Dynamically Baked ZnO ETL

We also fabricated devices using the four dynamically baked ZnO films to observe the effect of the extreme morphology change from the planar films to those with the smaller and larger nano-ridges. Figure 3-6 shows the current-voltage curves of devices made on the four dynamically baked ZnO films. The 1D and 2D films are spun at 4000 rpm with thicknesses of ~40 nm and ~47 nm, respectively, while the 3D and 4D films are spun at 2000 rpm with thicknesses of ~55 nm and ~64 nm, respectively. The inset of Fig. 3-6 shows the AFM image of the device top surface area outside the electrode, i.e. on MoO_3 of the stack of glass/ITO/ZnO (3D)/PTB7:$PC_{71}BM$/MoO_3, for a device with the large ZnO nano-ridges. The underlying texture of the ZnO nano-ridges can be seen protruding through the subsequent layers. The protrusion of the ZnO nano-ridges through the active layer suggests that these structures may affect the coating of the active layer on top. Thus, for a given ZnO film condition, it is important to ensure that the active layer coating conditions are adjusted to maintain the optimum thickness. At the similar BHJ thickness of ~94 nm, the J-V curves for the 1D, 2D, 3D and 4D ZnO conditions are all very similar and these devices showed high performance with average PCEs ranging from 7.68-7.79% and a maximum PCE of 8.14% (see Table 3-4). Congruent to the devices with the planar ZnO films, these PTB7-based devices with ZnO nano-ridges are not sensitive to the overall effective ZnO thickness or roughness as long as the thickness of the active layer is maintained.

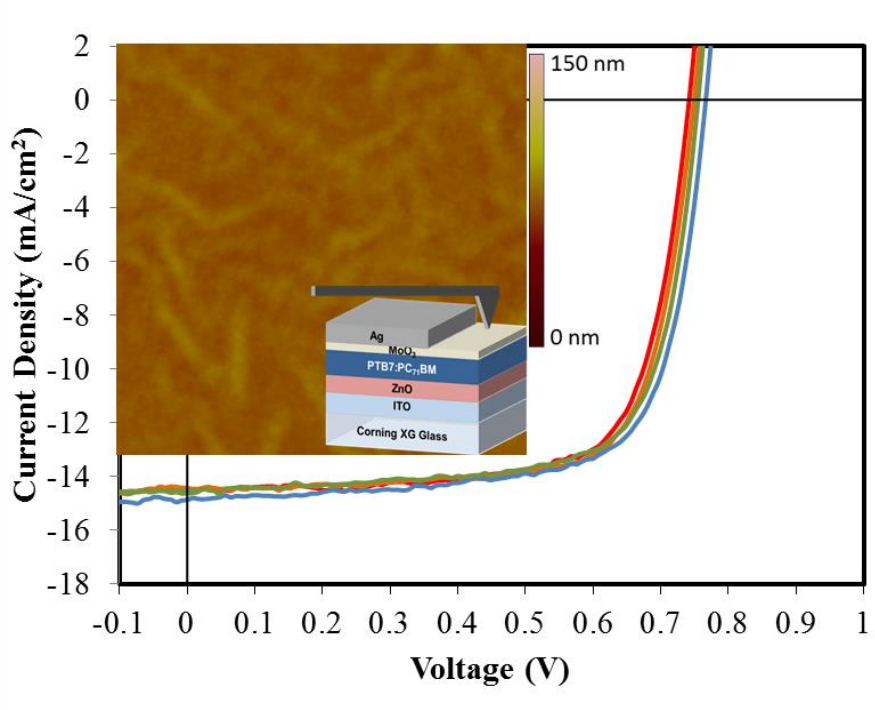

Figure 3-6. The J-V curves for devices with dynamically baked ZnO films of 1D (red), 2D (orange), 3D (blue) and 4D (green). The inset shows the AFM height image of a device on the MoO_3 layer outside the electrode area (i.e. ITO/ZnO (3D)/PTB7:$PC_{71}BM$ /MoO_3). The AFM images are 5µm x 5µm.

Table 3-4. Parameters of the inverted OPV devices with dynamically baked ZnO films indicated by the film numbers in Table 3-1.

ZnO Film	V_{OC} (V)	FF (%)	J_{SC} (mA/cm^2)	PCE (%)	PCE_{Max} (%)
1D	0.74 +/- 0.00	72.9 +/- 0.3	14.22 +/- 0.29	7.68 +/- 0.14	7.83
2D	0.74 +/- 0.00	72.9 +/- 0.7	14.27 +/- 0.33	7.74 +/- 0.18	7.99
3D	0.75 +/- 0.01	72.4 +/- 0.7	14.32 +/- 0.43	7.79 +/- 0.28	8.14
4D	0.76 +/- 0.00	70.7 +/- 1.1	14.51 +/- 0.18	7.78 +/- 0.16	7.90

We observed that there is no significant difference in the performance of the devices with the ZnO nano-ridges versus the planar films for similar PTB7:$PC_{71}BM$ layer thickness. Comparing devices with ZnO films 3S versus 3D (see Tables 3-3 and 3-4), for example, the FF's

are practically equal at 72.3% and 72.4%, respectively, and the J_{SC}'s are very close at 14.17 and 14.32 mA/cm^2, respectively, allowing both to exhibit high average PCE's near 8%. Additionally, the EQE spectra for these devices show no significant difference between those using planar and nano-ridged ZnO layers (see Figure 3-7). However, for P3HT:$PC_{61}BM$ based devices, different device performance was observed using nano-ridged versus planar ZnO films.[33] The increased FF observed in those P3HT:$PC_{61}BM$ devices was attributed to higher electron selectivity and more efficient charge collection due to the nano-ridged structure. Larger nano-ridges were formed in those ZnO films (~120 nm in height) with the condition of a higher precursor concentration (0.75 M). Also, the electronic properties of those ZnO films may differ from ours due to higher crystallinity created by the increased baking temperature of 275˚C. Another study baked ZnO films at the lower temperature of 200˚C, which is the same as is used in this work, but also observed the nano-ridged devices performed better with the P3HT:$PC_{61}BM$ BHJ.[28] Similar to the discussion of planar devices in the previous section, our observations of the PTB7-based devices versus those for P3HT-based ones can be explained by the differences in microstructure and inherent PV function between these two systems. The rapid charge separation and highly efficient photovoltaic function of the PTB7:$PC_{71}BM$ BHJ provide high FF's consistently exceeding 70% when the active layer thickness is optimized. This effectively desensitizes this OPV system to the ZnO conditions probed here. Park et al. also compared planar and nano-ridged ZnO films in a PTB7-F20:$PC_{71}BM$ BHJ, similar to the devices presented in this work.[28] They observed slight increases in all performance parameters to reach a PCE of 6.42% with the nano-ridges versus 5.12% with the planar films. However, this relatively low PCE and FF of 65% for the nano-ridged device suggest the active layer thickness was not fully

optimized. Additionally, differences between PTB7 and PTB7-F20 as well as between their ZnO film conditions versus ours may also contribute to these observations.

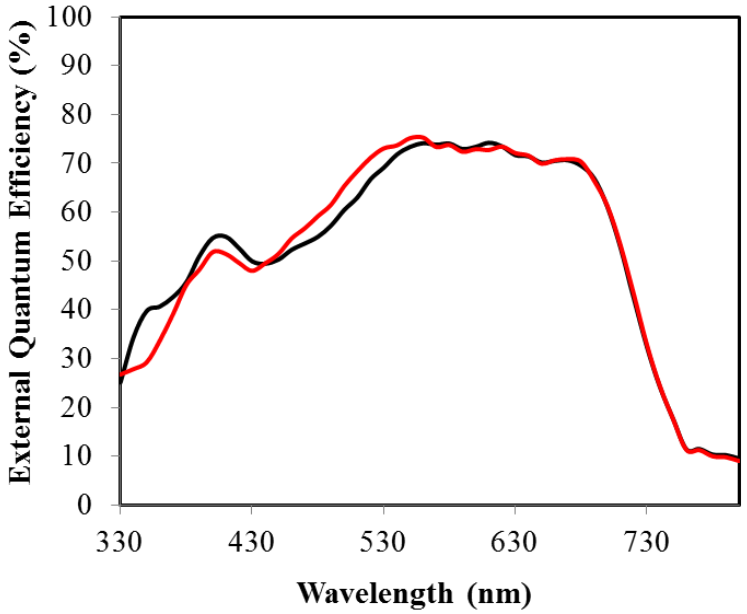

Figure 3-7. External quantum efficiency (EQE) spectra of devices with ZnO films 3S (red) and 3D (black).

3.3.4 Optimization of Active Layer for Different ZnO ETL Morphologies

It is well known that active layer film thickness is crucial to optimizing performance in OPV devices. Organic semiconductors have relatively low charge carrier mobilities which limits the active layer thickness in most OPV devices to less than ~100 nm.[7, 9, 78] The optimum thickness reflects a balance between maximizing light absorption and minimizing charge recombination. Additionally, overall light harvesting in OPVs is closely related to the electric field distribution and intensity within the completed device architecture which is tied to the thickness and optical properties of each layer.

We performed TMM calculations to investigate how the optimum active layer thickness changes for the ZnO films prepared under different conditions. The experimentally measured

refractive indices of each ZnO film (see Fig. 3-3) were used in the TMM calculations. Figure 3-8(a) shows the calculated J_{SC} versus active layer thickness for each of the ZnO films. According to the TMM results, the active layer film thickness dominates the behavior of the J_{SC}. Varying the ZnO film thickness and morphology do not significantly change the optimum active layer film thickness for these inverted devices. The J_{SC} maxima of 15.0-15.3 mA/cm^2 for the various ZnO films are predicted with the active layer thickness primarily centered between ~75-95 nm. As we have observed for devices made on different ZnO films (Tables 3-3 and 3-4), similar J_{SC}'s (14.17-14.51 mA/cm^2) and FF's (70.7-73.4%) were obtained as long as the active layers had similar thickness (~94 nm). The model assumes 100% internal quantum efficiency (IQE) and does not take recombination or parasitic resistances into account. Thus, the model predicts in general that thicker active layers would generate higher J_{SC}'s.

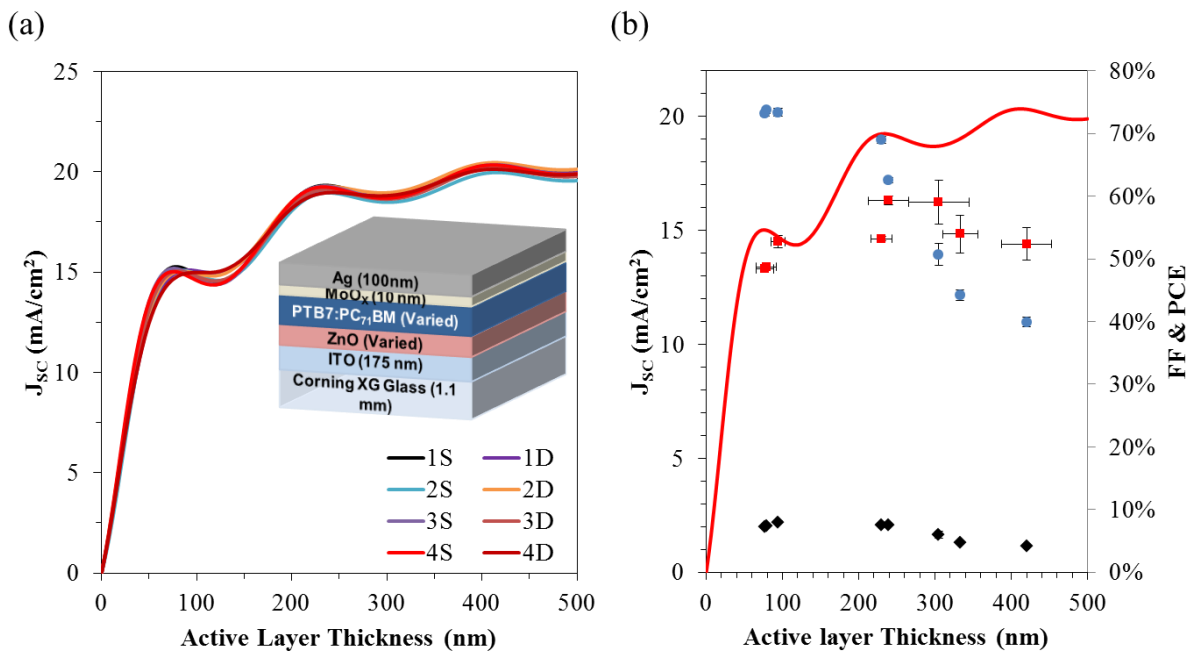

Figure 3-8. (a) The calculated J_{SC} versus active layer thickness for each of the ZnO films, as labeled in Table 3-1, using their respective optical properties. The inset shows a schematic of the device structure modeled. (b) The calculated (red line) versus experimental (red squares) J_{SC} for devices of varied active layer thickness with a statically baked ZnO film (4S). The experimental FF (blue circles) and PCE (black triangles) of the devices are also included.

Devices with varied active layer thicknesses were fabricated on top of statically baked ZnO films for comparison. The ZnO films were prepared with the same condition for 4S in Table 3-1. Figure 3-8(b) shows the experimental J_{SC}'s (red squares) of these devices compared to the calculated J_{SC}'s (red line). The J-V curves and the performance parameters for these devices are provided in Figure 3-9 and Table 3-5. The average J_{SC} for the actual devices was 14.50 mA/cm^2 (Table 3-3) versus the calculated J_{SC} of 14.70 mA/cm^2 at an optimal active layer thickness of ~94 nm. The experimental value is expected to be slightly lower than the calculated value as real devices do not operate at 100% IQE and suffer losses due to recombination and parasitic resistances. Variation may also be introduced due to any error in the measured experimental film thicknesses and refractive indices. When the active layer was increased to ~240 nm, the experimental J_{SC} did increase to 16.31 mA/cm^2 but at the cost of a diminished FF which dropped from 73.4% to 62.6%. This drop in FF is due to the thicker active layer requiring charges to travel further to reach their respective electrodes which increases the recombination probability. Even though the thicker active layer generated an increased J_{SC}, the large FF decrease resulted in a drop of the average PCE from 8.01% to 7.54%. The lower experimental J_{SC} compared to the calculated Jsc for the thicker active layer is also a direct result of high recombination rates. Further increasing the active layer thickness to ~305 nm, ~333 nm, and ~420 nm resulted in declining FF's of 50.7%, 44.2%, and 39.9% resulting in PCEs of 5.98%, 4.74%, and 4.15%, respectively. The J_{SC}'s also dropped to 16.24 mA/cm^2, 14.84 mA/cm^2, and 14.40 mA/cm^2, respectively. Figure 3-8 shows that the TMM calculations predict a sharp variation of J_{SC} in either direction near the optimum active layer thickness (i.e. ~75-95 nm). Moving the opposite direction and decreasing the active layer to ~79 nm maintained a high FF at 73.7% but showed the J_{SC} drop to 13.40 mA/cm^2 resulting in an average PCE of 7.39%. This

highlights the sensitivity of these devices to small changes in active layer thickness. Large changes in ZnO morphology may affect the thickness of the active layer spun on top. Thus, it is important to ensure that the active layer coating conditions are adjusted to maintain the optimum thickness when changing the underlying ZnO conditions.

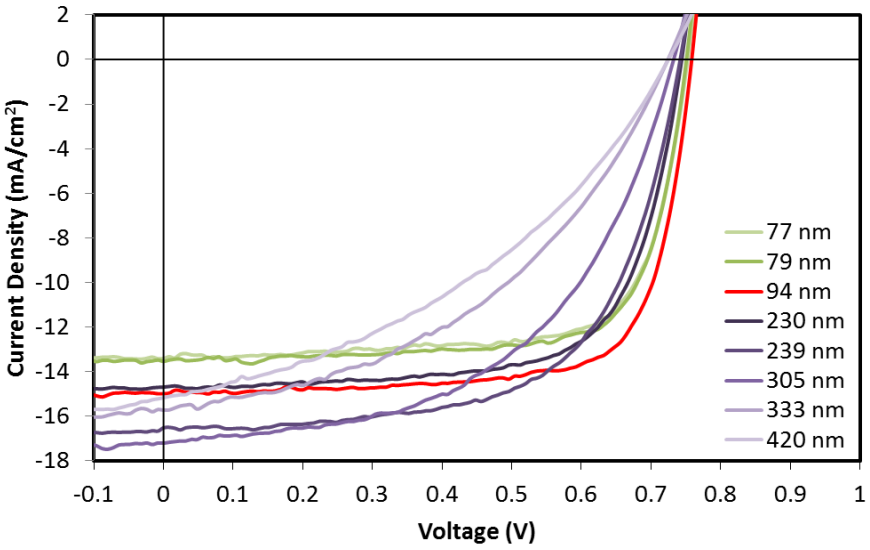

Figure 3-9. J-V curves of devices using the 4S ZnO films with varied active layer film.

Table 3-5. Average performance parameters of inverted devices on 4S ZnO with varied active layer thickness.

Active Layer Thickness (nm)	V_{OC} (V)	FF (%)	J_{SC} (mA/cm^2)	PCE (%)
77 +/- 11	0.75 +/- 0.00	73.2 +/- 0.4	13.32 +/- 0.10	7.27 +/- 0.06
79 +/- 13	0.75 +/- 0.00	73.7 +/- 0.5	13.40 +/- 0.09	7.39 +/- 0.08
94 +/- 9	0.75 +/- 0.00	73.4 +/- 0.6	14.50 +/- 0.28	8.01 +/- 0.19
230 +/- 14	0.74 +/- 0.00	69.0 +/- 0.6	14.63 +/- 0.09	7.51 +/- 0.02
239 +/- 26	0.74 +/- 0.00	62.6 +/- 0.4	16.31 +/- 0.18	7.54 +/- 0.09
305 +/- 40	0.73 +/- 0.01	50.7 +/- 1.7	16.24 +/- 0.97	5.98 +/- 0.59
333 +/- 23	0.72 +/- 0.00	44.2 +/- 0.8	14.84 +/- 0.83	4.74 +/- 0.23
420 +/- 33	0.72 +/- 0.00	39.9 +/- 0.8	14.40 +/- 0.71	4.15 +/- 0.17

Figures 3-10(a) and (c) show the electric field distributions versus wavelength through the inverted device structure with a statically baked ZnO layer (2S) with thinner and thicker active layer thicknesses (i.e. 62 nm vs. 85 nm). For the PTB7:$PC_{71}BM$ system, many references in the literature cite an optimum active layer film thickness of ~80-90 nm.[14, 30] In agreement, the TMM modeling shows a maximum J_{SC} centered near this value, as seen in Fig. 3-8. The calculated J_{SC} was 14.0 mA/cm^2 for a thinner 62 nm active layer compared to 15.1 mA/cm^2 for one at 85 nm. This photocurrent increase not only stems from more absorbing material being present to create photogenerated charges but also from an electric field distribution which has its maximum intensity optimally aligned within the active layer (see Fig. 3-10(a) vs (c)). Figure 3-10(b) and (d) show the resulting charge generation profile in the active layer for each case. The J_{SC} strongly depends on the charge generation rate and the diffusion length of electrons and holes.[5] Alignment of the peak electric field intensity in the center of the active layer (see Fig. 3-10(c)) correlates to alignment of the peak charge generation rate in the center of the active layer. This, in turn, maximizes the sum of the charge generation rate across the active layer resulting in a larger J_{SC} for the 85 nm versus the 62 nm BHJ layer. Even when assuming 100% IQE, further increase of the active layer thickness actually decreases the calculated J_{SC} as the peak charge generation rate is not optimally aligned. For example, the sum of the charge generation rate for a thicker 125 nm active layer actually decreases compared to the 85 nm case due to the altered optical field distribution resulting in a lower J_{SC} of 14.6 mA/cm^2, as seen in the J_{SC} dip at ~125 nm in Fig. 3-8. Thus, the active layer thickness is critical to device performance which is why it should be actively optimized if the underlying ETL morphology changes significantly.

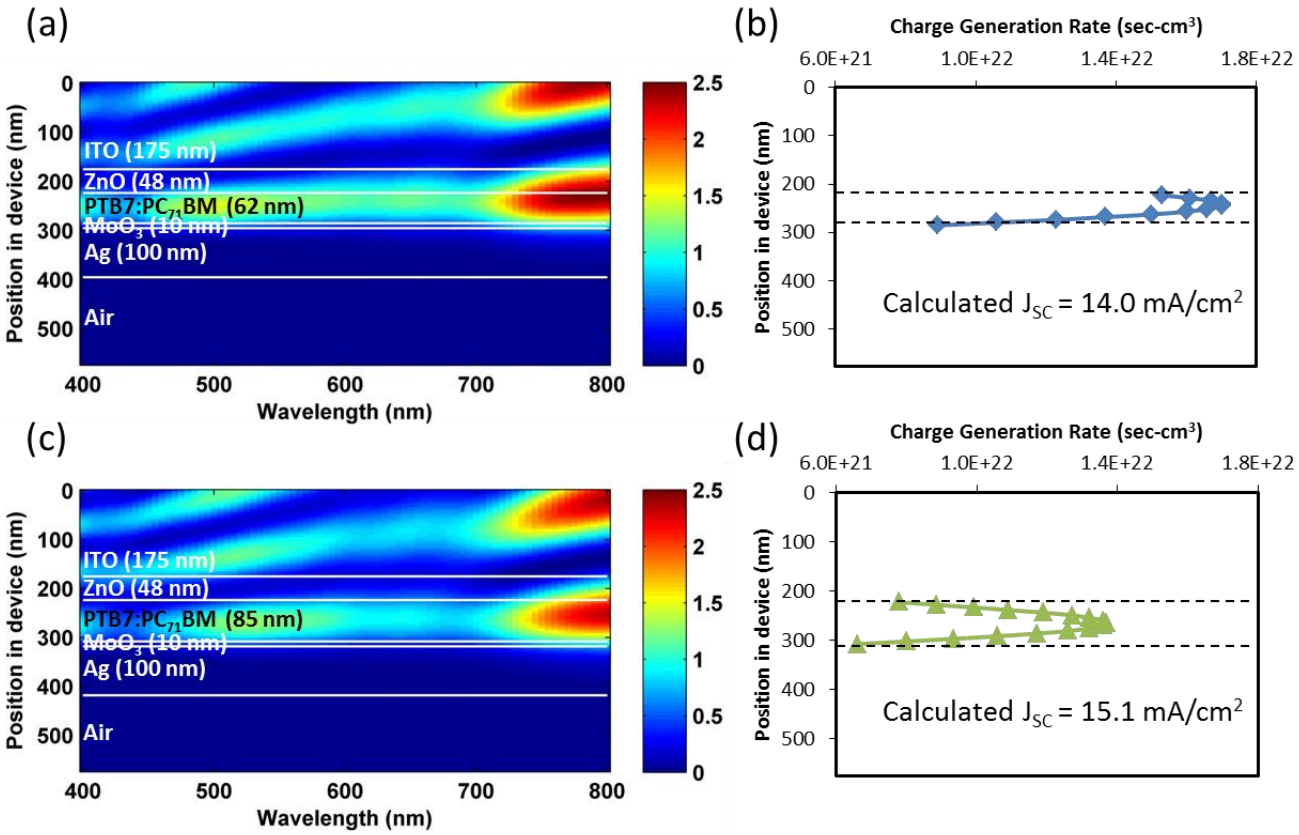

Figure 3-10. (a) The calculated electric field intensity profile versus wavelength and depth in the device for an inverted structure using the optical properties of the 2S ZnO film with an active layer thickness of 62 nm. (b) The calculated charge generation profile in the active layer for the device in (a). (c) The calculated electric field intensity profile similar to (a) but with an 85 nm active layer. (d) The calculated charge generation profile in the active layer for device (c).

3.4 Conclusions

In conclusion, we fabricated high efficiency inverted devices using the PTB7:$PC_{71}BM$ BHJ and studied the effects of varied ZnO ETL morphology and thickness on device performance. By statically and dynamically baking the ZnO, we created planar and nano-ridged structures, respectively. The optical properties of the various ZnO films were measured and also observed to change with morphology. Optical calculations showed that optical field distribution changes due to the different ZnO films could only account for small changes in J_{SC} in the range

of 0.3-0.5 mA/cm^2. In agreement with the models, devices fabricated with statically baked, planar ZnO films of varied conditions showed consistent J_{SC}'s ranging from 14.17-14.50 mA/cm^2. These devices were insensitive to the varied ZnO thickness and roughness and exhibited consistently high PCEs averaging 7.65-8.01% with a maximum PCE reaching 8.32%. The devices fabricated here also showed no significant difference in performance between those with planar versus nano-ridged ZnO ETLs which also exhibited high PCE's averaging 7.68-7.79% with a maximum PCE reaching 8.14%. The highly efficient photovoltaic function of the PTB7:PC_{71}BM BHJ provides consistently high FF's exceeding 70%, when the active layer thickness is optimized, effectively desensitizing this OPV system to the ZnO conditions probed here. However, the models and experiments highlight the sensitivity of these devices to active layer film thickness. Thus, maintaining the optimum active layer thickness when changing the underlying ETL conditions is critical for achieving high efficiency inverted OPVs.

CHAPTER 4. DESIGN AND DEVELOPMENT OF PLASMONIC NANOSTRUCTURES FOR ITO-FREE HIGH PERFOMANCE PTB7:PC_{71}BM-BASED PHOTOVOLTAIC CELLS

4.1 Introduction

Organic photovoltaics (OPVs) offer significant potential to lower the manufacturing costs of solar energy harvesting devices and enable large area, lightweight, and highly flexible photovoltaics. A central challenge for OPVs is the trade-off between an active layer of sufficient film thickness to absorb as much light as possible while minimizing charge recombination. This balance between absorption and recombination typically results in using thin active layers that do not take full advantage of the incident light. Developing light manipulation techniques to maximize absorption is a key component for pushing OPVs to their peak potential.

Integrating plasmonic nanostructures into these devices is one promising way to enhance absorption and is typically achieved by deploying Au or Ag nanoparticles in various layers of an OPV.[42, 43] LSPR-induced enhancements were observed when Au NPs of ~45 nm with a resonance peak at ~550 nm were deployed in the anodic buffer layer (~50 nm thick) of conventional devices with the structure glass/ITO/PEDOT:PSS/P3HT:PCBM/Ca/Al.[79] Increased light absorption was observed which significantly increased the exciton generation rate. Also, dynamic PL measurements revealed noticeably reduced exciton lifetimes suggesting that interplay between the LSPR-induced fields and photogenerated excitons facilitated charge transfer by reducing geminate recombination and increasing the probability of charge

dissociation. Accordingly, both J_{SC} and FF increased and V_{OC} remained constant resulting in a PCE increase from 3.57% to 4.24%.[79] In another study, conventional devices with the same structure but with the PTB7:PC_{71}BM active layer showed J_{SC} and FF enhancements when Au or Ag NPs were deployed in the PEDOT:PSS layer.[43] Interestingly, the best device used both Au and Ag NPs (40-50nm) with resonant peaks at ~529 nm and ~425 nm, respectively, creating a cooperative plasmonic effect to achieve a PCE as high as 8.67% compared to the control device at 7.25% due to enhanced J_{SC} and FF as well. The enhanced light absorption was in good agreement with the plasmonic resonance regions of both the Ag and Au NPs. This dual resonance enhancement of two different NPs also enhanced the exciton generation rate and dissociation efficiency, as well as increased the charge carrier density and lifetime.[43] These plasmonic NPs can also be placed inside the active layers of OPVs to exploit the strongly confined field of the LSPRs and to enhance light scattering in the layer. The metallic NPs placed within this layer can be used as sub-wavelength antennas where the enhanced near-field is coupled to the OPV active layer which increases its effective absorption cross-section.[8, 39] For example, size-controlled Ag NPs (40nm) with a maximum absorbance peak at 420 nm were deployed in the active layer of a conventional device with a PCDTBT:PC_{70}BM BHJ. The device with the NPs showed a PCE improvement from 6.3% to 7.1% due to an improved J_{SC} and FF stemming from enhanced light absorption and also a lower series resistance.[80] It is critical to fine tune the concentration, dispersion, and size of metal NPs when used inside an active layer in order to minimize loss mechanisms including non-radiative decay and non-geminate recombination.[8]

In addition to plasmonic NPs, 1D and 2D metallic nanostructures can be integrated into devices to provide similar light absorption enhancements. For example, an inverted device with

the structure ITO/ZnO NPs/PTB7:$PC_{71}BM$/MoO_3/Ag was fabricated with a 1D nanograting structure on the back Ag electrode.[44] This grating was made by imprinting the active layer with a polydimethylsiloxane (PDMS) stamp prior to depositing the MoO_3 and Ag layers. The grating width and height were approximately 700 nm and 40 nm, respectively, so that the MoO_3 and Ag layers both duplicated this imprinted grating structure forming the Ag metal nanostructure capable of supporting SPPs. The PCE was enhanced from 7.73% compared to a control device at 7.20% due to an improved J_{SC} from enhanced absorption which was attributed to local near field enhancement and scattering effects.[44] Another work used this 1D plasmonic grating as the back electrode combined with Au NPs incorporated into the active layer to reach a PCE as high as 8.79% from improved J_{SC} and FF due to enhanced absorption and a lower series resistance.[45]

However, 1D metallic nanostructures like these gratings are dependent on the polarization of incident light, which is generally a limitation for OPV applications, and the resonant wavelengths of SPP modes supported by optically thick metal films depends significantly on the incident light angle.[8] It is desirable to use metallic nanostructures that lead to broadband, polarization-independent, and angle-insensitive absorption enhancement. Periodic 2D nanostructures with high-order symmetries along different in-plane directions can provide these advantages. Large area, 2D nanotriangle arrays were fabricated on ITO by nanosphere lithography and used in conventional devices with a PCDTBT:$PC_{71}BM$ BHJ.[46] The PCE improved from 4.24% to 4.52% which was attributed an increase in exciton generation induced by the strong local E-field and scattering generated by LSPRs. Another work also used nanosphere lithography to place a 2D Au nanomesh on top of ITO in a conventional P3HT:PCBM device for a PCE enhancement from 1.9% to 3.2% due to improved absorption.[47]

The previous works mentioned added plasmonic nanostructures to devices to enhance absorption and PCE. It could be highly beneficial to integrate these nanostructures as the electrodes themselves to take advantage of plasmon-induced optical enhancements while also replacing ITO with a cheaper and more mechanically robust material. ITO is typically used as the transparent conducting electrode in most OPVs. The substrate cost is a primary factor in the manufacturing costs of OPVs and limited reserves of indium have led to escalating ITO prices making it a poor choice as an electrode for large-scale device production.[8, 81-83] ITO is also a poor match for use in flexible devices as it has low conductivity on flexible substrates and is brittle and cracks easily upon bending.[8, 82, 83] Various alternative electrode materials have been successfully used in OPVs such as Ag nanowire composites and ultrathin metal films.[78, 82, 84] One work has been seen where ITO was replaced by a plasmonic Au-nanohole array as the anode for conventional OPVs based on P3HT:PCBM BHJs on glass.[85] The plasmonic nanostructures improved light absorption and had lower sheet resistance than ITO which improved both the J_{SC} and FF to yield a PCE increase from 2.9% to 4.4%. Omnidirectional light absorption was improved in these devices over ITO as light coupling to the nanostructures was nearly independent of both light incident angle and polarization. Still, the use of alternative electrodes that replace ITO and exhibit plasmonic enhancement is not highly studied, especially with highly efficient OPV systems and flexible substrates, and offers significant potential to improve OPVs.[8, 85]

In this work, we designed and fabricated plasmonic nanohole arrays to serve as the bottom electrode to replace ITO for rigid and flexible high efficiency OPVs. We used Finite-Difference Time-Domain (FDTD) electromagnetic simulations to design the Au nanohole arrays and device structures to maximize both active layer absorption and the intensity of plasmon-

induced electric fields and minimize device reflectance. These nanostructured Au plasmonic electrodes with Cr "glue" layers were fabricated using nanoimprint lithography (NIL) in a process that is scalable to roll-to-roll manufacturing. Simulation results indicated that the Cr layer reduces active layer absorption so a new fabrication technique, i.e. solvent-assisted nanomolding (SAN), was also developed and used to make Au-only nanostructures. We used a PTB7:$PC_{71}BM$ BHJ active layer and made ITO-free inverted devices with these nanostructured electrodes. Plasmonic nanostructured electrodes were fabricated on bare glass, bare flexible PET and bare conformable Parylene substrates and compared to control devices on ITO-coated glass and ITO-coated PET. The effects of these plasmonic nanostructured electrodes, along with varied ZnO layer thickness/type, active layer thickness, nanohole size and other parameters, on device performance are discussed. To our knowledge, this is the first time nanopatterned plasmonic electrodes have been applied to high efficiency and flexible OPVs and the learnings presented here can be utilized to fabricate high performance electrodes for widespread photovoltaic systems.

4.2 Experimental

4.2.1 FDTD Simulations

The FDTD method (Lumerical Solutions, Inc. software) was used to calculate the reflectance, transmittance, various layer absorption spectra and electric field profiles of devices with and without nanostructures. The simulations were conducted using a single nanohole in Cr/Au (2 nm/23 nm) or Au (25 nm) layers on glass with layers of ZnO (varied thickness), PTB7:$PC_{71}BM$ (varied thickness), MoO_x (10 nm) and Ag (100 nm) stacked on top as a unit cell with periodic boundary conditions in the x and y directions. The nanohole was assumed to be filled with ZnO. A continuous wavelength plane wave light source (λ = 400-900 nm) was placed

in the glass layer 400 nm below the interface of glass and the first layer (i.e. ITO, Cr, or Au). A frequency-domain field and power monitor was placed 100 nm below the light source to collect the reflectance spectrum from the device. Other power monitors were placed at the various layer interfaces to calculate layer transmission and absorption. Field profile monitors were placed at the cross-sectional x–z plane at the center of the nanohole and over the x-y plane above the nanohole to obtain the near-field electric field profiles. The wavelength-dependent refractive indices of Cr, Au and Ag in the simulation wavelength range were provided in the software database from the CRC handbook. For Corning XG glass, ITO, ZnO, PTB7:$PC_{71}BM$ and MoO_x, the wavelength-dependent refractive indices and extinction coefficients were measured with spectroscopic ellipsometry (J.A. Woollam Co., Inc. α-SE Spectroscopic Ellipsometer, CompleteEASE software). The simulated background refractive index was 1 so the devices were considered to be exposed to air where no layer parameters were defined. Nanohole diameter, pitch and Au thickness were all varied to find the optimum conditions.

4.2.2 Nanoimprint Lithography

Nanoimprint lithography (Nanonex NX-B100, NIL) was used to fabricate the plasmonic Au-nanostructures at the Washington Nanofabrication Facility (WNF). All substrates were cleaned by ultrasonication in soapy deionized (DI) water, DI water, acetone, and isopropanol and plasma treated. Thermal imprint resist (Nanonex NXR-1025, 2.5%) was spin coated at 1000 rpm and baked at 150°C for 90 s for ~ 80 nm thick films. ETFE (DuPont Tefzel ETFE 1000LZ, 0.01" thick) pieces were cut with a razor blade and cleaned by ultrasonication in acetone and isopropanol. The silicon master mold was made using electron beam lithography (EBL) and reactive ion etching (RIE) methods by the WNF with 175 nm diameter nanopillars at a 225 nm pitch and 140 nm tall. The silicon master mold was initially oxygen plasma treated, cleaned via

ultrasonication steps and silanized with trichloro(1H,1H,2H,2H-perfluorooctyl)silane (TCPFOSi, Sigma Aldrich, 97%) in a vacuum desiccator under pumping for 30 minutes. To imprint ETFE from the Si master mold, NIL was done at 250˚C and 450 psi for 1 minute. The ETFE should release easily if silanization is effective and the master mold was used until ETFE started to stick. NIL from the ETFE to the resist was done at 120˚C and 200 psi for 1 minute. The ETFE was carefully peeled off and the imprinted substrates were dry etched with oxygen plasma in a barrel asher (Glow Research AutoGlow) at 25W for various times to find the best condition to remove the resist at the bottom of the nanopillars. Then the etched samples were placed in a vacuum chamber where 2 nm Cr and 23 nm Au were evaporated on to the etched films. An evaporator (Angstrom Engineering AMOD and EVOVAC, thermal and e-beam multisource) in the UW Photonics Research Center (UW Dept. of Chemistry) was used but showed significant shadowing of Au on the sides of the nanopillars. Thereafter, an evaporator (CHA Solution Process Development System) at the WNF was used with slightly improved results. After Cr/Au deposition, a solution lift-off step was performed by sonicating the films in 1:1:5 $NH_4OH(aq):H_2O_2(aq):H_2O$ solution for >30 min at >40˚C. As fabrication procedures developed, a "peel-off" step was added where the nanostructured substrates were covered with NOA-88 (Norland Products) optical adhesive after the solution lift-off. Tape was put on the backside to prevent sticking of the substrates to their holder. These substrates were then placed in a vacuum desiccator under vacuum for >30 min to release entrapped bubbles in the NOA-88. Then the NOA-88 was cured under UV light for >30 min. After curing, the NOA-88 could be peeled off carefully to remove the "Au-tops" while the nanohole films underneath remained. These nanostructured substrates were then plasma treated and cleaned by normal methods before use in OPV devices.

4.2.3 Alternative Techniques for Nanostructure Fabrication

Alternative nanofabrication techniques were explored to eliminate the need for the Cr "glue" layer and allow faster, cheaper and larger area nanostructure production. Methods such as microcontact printing (μCP), solvent-assisted micromolding (SAMIM) and nanotransfer printing (nTP) were adapted to fabricate our nanostructures.[86, 87] These methods require making a stamp with the nanopattern copied from the master silicon mold. The master silicon mold was first cleaned, oxygen plasma treated and silanized with TCPFOSi to turn the silicon surface hydrophobic to prevent cured PDMS from sticking. Hard polydimethylsiloxane (h-PDMS) is required for nanoscale resolution of the nanopillars in our master mold and was prepared by mixing 3.4 g of (7-8% vinylmethylsiloxane)-(dimethylsiloxane) copolymer (Gelest), 0.1 g of 1,3,5,7-tetramethylcyclotetrasiloxane modulator (Gelest), 18 μL of platinum divinyltetramethyldisiloxane catalyst (Gelest) and 1 g of (25–30% methylhydrosiloxane)–(dimethylsiloxane) copolymer (Gelest) using protocols according to the literature.[86, 88] A composite stamp of h-PDMS and PDMS was prepared by spin coating a thin layer of h-PDMS to cover the nanopattern, baking at 60°C for 10 min, pouring pre-made PDMS (10:1 weight ratio of Sylgard 184 silicone elastomer base to curing agent (Dow Corning)) over the top in small plastic petri dish, degassing for over 30 min and curing for over 2 h at 70°C.[86, 88] The composite PDMS/h-PDMS stamp can then be peeled off of the master mold and cut into a smaller stamp size.

Self-assembled monolayers (SAMs) of 3-mercaptopropyltrimethoxysilane (MPTMS) were formed on glass substrates as a molecular adhesive to replace the Cr "glue" layer. In order to form the SAMs, the substrates were first cleaned and treated with oxygen plasma to generate surface hydroxyl groups (-OH) and then placed under vacuum in a desiccator with 100 μL of

MPTMS for greater than 1 h. This procedure allows co-condensation of the methoxy (-OCH_3) groups of MPTMS with the surface hydroxyl groups of the substrate.[87, 89]

For the μCP method, Au was deposited after forming the MPTMS SAMs. The composite PDMS stamp was then coated with an alkanethiol molecules by swabbing with a Q-tip soaked in 2 mM Octadecanethiol (ODT, Aldrich) in ethanol, dried in a stream of nitrogen and then stamped onto the gold-coated substrate for 5-20 s. Contact was initiated with the stamp at an angle to avoid trapping air bubbles between the stamp and substrate. It is critical to leave the stamp and the substrate in contact for < 20 s, otherwise the thiol molecules may also be transferred from the recessed region of the stamp to the substrate through diffusion. The thiol molecules form a SAM on the Au surface that mirrors the nanopattern from the stamp. The thiol-coated Au substrates were then dipped in a ferricyanide etching solution (0.1 M $K_2S_2O_3$, 0.01 M $K_3Fe(CN)_6$, 0.001 M $K_4Fe(CN)_6$ trihydrate and 1.0 M KOH in water) to selectively remove the unprotected regions of gold under stirring at room temperature. Etching times were varied to find optimum conditions. Note that this etching solution can also be used to enlarge nanohole diamters in pre-made Au nanopatterns.

The SAMIM method was also adapted to our nanostructures and re-termed the solvent-assisted nanomolding (SAN) method. SAN can be used with substrates pre-coated with MPTMS/Au layers in a procedure similar to μCP or by forming the MPTMS SAM first then following the SAN procedures and depositing Au at the end. We observed better results with the second procedure. For this procedure, a 3% solution of PMMA in anisole was spin coated on top of glass substrates with pre-made MPTMS SAMs and baked at 180°C for 90 s. Next, these substrates were pre-heated to 60°C, 6μL of acetone were dropped onto the PDMS/h-PDMS stamp surface and the stamp was carefully brought in contact with the substrate with little to no

pressure and allowed to sit for 5 min. Next, the stamp was removed and the PMMA nanopatterns were etched in oxygen plasma to descum the residual PMMA at the bottom of the nanopillars. Then Au was deposited and the substrates were sonicated in acetone to lift off PMMA nanopillars with Au nanodisks on top to generate the Au nanohole array. The stamping pressure and angle, etching time and power, PMMA thickness and other parameters required optimization to achieve quality nanopatterns. MPTMS SAMs will also be destroyed by the oxygen plasma etching step so it is important to find the proper etching and film conditions to allow sufficient MPTMS survival for an effective molecular adhesive to Au. Master mold contamination by h-PDMS/PDMS and by undesired silane cross-linking was encountered and required cleaning in Pirahna solution and 10:1 buffered oxide etch solutions (i.e. buffered HF).[90]

4.2.4 Film and Device Fabrication

The ZnO sol-gel solution was prepared by dissolving zinc acetate dihydrate ($Zn(CH_3COO)_2 \cdot 2H_2O$, Sigma-Aldrich, >99.0%) and ethanolamine ($NH_2CH_2CH_2OH$, Sigma-Aldrich, >99.5%) in 2-methoxyethanol ($CH_3OCH_2CH_2OH$, Sigma-Aldrich, 99.8%, anhydrous) under vigorous stirring for greater than 12 h. Concentrations of 0.3 M, 0.44 M and 0.54M were used for varied film thicknesses. ZnO nanoparticles (NPs) purchased commercially (Sigma Aldrich, <100 nm particle size (DLS), <35 nm avg. part. size (APS), 50 wt. % in H_2O) were diluted in DI water to 5.22 vol%. The in-house synthesized ZnO NPs were made using procedures in the literature.[91] Parylene-coated glass substrates were prepared by vapor deposition using ~45 g of Parylene-C. ITO-coated glass, ITO-coated PET, bare glass, bare PET and parylene-coated glass substrates with nanostructured electrodes were cleaned by ultrasonication in soapy deionized (DI) water, DI water, acetone, and isopropanol. The ITO and nanostructured substrates were treated with oxygen plasma prior to depositing any films. The

ZnO sol-gel solutions were spin-cast on top of the pre-cleaned substrates at 2000 rpm or 4000 rpm for 60 s. These samples were then annealed at 200°C for 1 h under static conditions. The ZnO NPs purchased commercially were spin coated at 3000 rpm for 30 s and baked for 10 min at 140°C. The in-house synthesized ZnO NPs were sonicated for >5 min., filtered through a 0.45 µm PTFE filter, and spin coated 1-5 times at 3000 rpm for 30 s to build up the film in a layer by layer fashion of varied thicknesses. No baking was required for the synthesized NPs. A PTB7 solution (1-Material, Inc.; 20.7 mg/mL) and a $PC_{71}BM$ solution (Nano-C; 31.0 mg/mL) in chlorobenzene were each made in a N_2-filled glovebox and stirred overnight at 60°C. Then these solutions were mixed with a polymer:fullerene ratio of 1.5:1 with 3.0 vol% 1,8-diiodooctane and allowed to stir for >1 h. The mixed solution was then cooled to room temperature and filtered with a 0.2 µm PTFE filter. The cooled filtered solution was spin cast on top of the ZnO films at varied spin speeds for 60 s. Then, the active layer coated substrates were loaded in a vacuum chamber ($<10^{-6}$ Torr) where a 10 nm film of MoO_3 and 100 nm film of Ag was deposited through a shadow mask by thermal evaporation. Each substrate had 16 pixels with defined areas of 3.14 mm^2 each.

4.2.5 Film and Device Characterization

The reflectance spectra were measured via a laboratory setup. White light from a halogen lamp (Ocean optics, HL-2000) was guided via an optical fiber and then collimated and polarized. The light was reflected to 90˚ by a beam splitter to illuminate the device at normal incidence. The reflected light from the device was collected through an objective (4x, 0.1 NA, Nikon) into an optical fiber connected to a spectrometer (Ocean optics, S2000). All reflectance spectra were normalized to the spectrum collected from a flat mirror. Transmission spectra were obtained with the same set-up but with the objective and light source oriented in-line with no

beam splitter. Scanning electron microscopy (FEI Sirion SEM) images of the nanostructures were taken at the Nanotech User Facility, the UW site of the National Nanotechnology Infrastructure Network (NNIN) supported by the NSF. Normal and angular current-voltage measurements for all inverted devices were conducted in a glove box under nitrogen atmosphere using a Keithley 2400 Source Meter and a solar simulator with a Solar Light Co. Xenon lamp (16S-300W) and an AM 1.5 filter. The light intensity was calibrated to 100 mW/cm^2 using a calibrated silicon solar cell that had been previously standardized at the National Renewable Energy Laboratory. EQE measurements were gathered in air using an Oriel Xenon lamp (450W) with an AM1.5 filter, a monochromator (Oriel Cornerstone 130 1/8 m) and a lock-in amplifier (Stanford Research Systems).

4.3 Results and Discussion

4.3.1 Design of Plasmonic Nanohole Arrays Using FDTD Simulations

The plasmonic nanostructured electrodes were designed using FDTD simulation based on integration into an inverted OPV device with the structure glass/Au-nanopattern (25 nm)/ZnO (48 nm)/PTB7:$PC_{71}BM$ (90 nm)/MoO_3 (10 nm)/Ag (100 nm), shown in Figure 4-1(a). The design for the nanostructure is chosen to maximize active layer absorption (especially in the wavelength range corresponding to the bandgap of the active layer materials), minimize device reflection and maximize the electric field enhancements. Figure 4-1(b) shows the calculated absorption spectra of the PTB7:$PC_{71}BM$ active layer for devices using plasmonic nanohole electrodes with varied hole sizes from 100-200 nm in diameter while keeping a constant pitch of 225 nm. In the FDTD simulations, frequency-domain field and power monitors were placed at the interfaces of each layer and the difference in power transmission between any two monitors is equal to the absorption of the layer between them. With this pitch, the absorption over a broad

wavelength range increases as the hole size increases, i.e. from cold to warm colors in Fig. 4-1(b). The spectra of the structures with the 175 nm (red) and 200 nm (dark red) diameter holes show the highest active layer absorption overall, especially in the region from 600-700 nm which is approaching the optical band gap of PTB7. As the nanohole size and active layer absorption increase, Fig. 4-1(c) and (d) show that the Au layer absorption is relatively constant and the ZnO layer absorption is negligible, respectively, for the various cases. Thus, decreased light absorption in the Au layer is not the primary cause for the increased active layer absorption seen as the nanohole diameter enlarges.

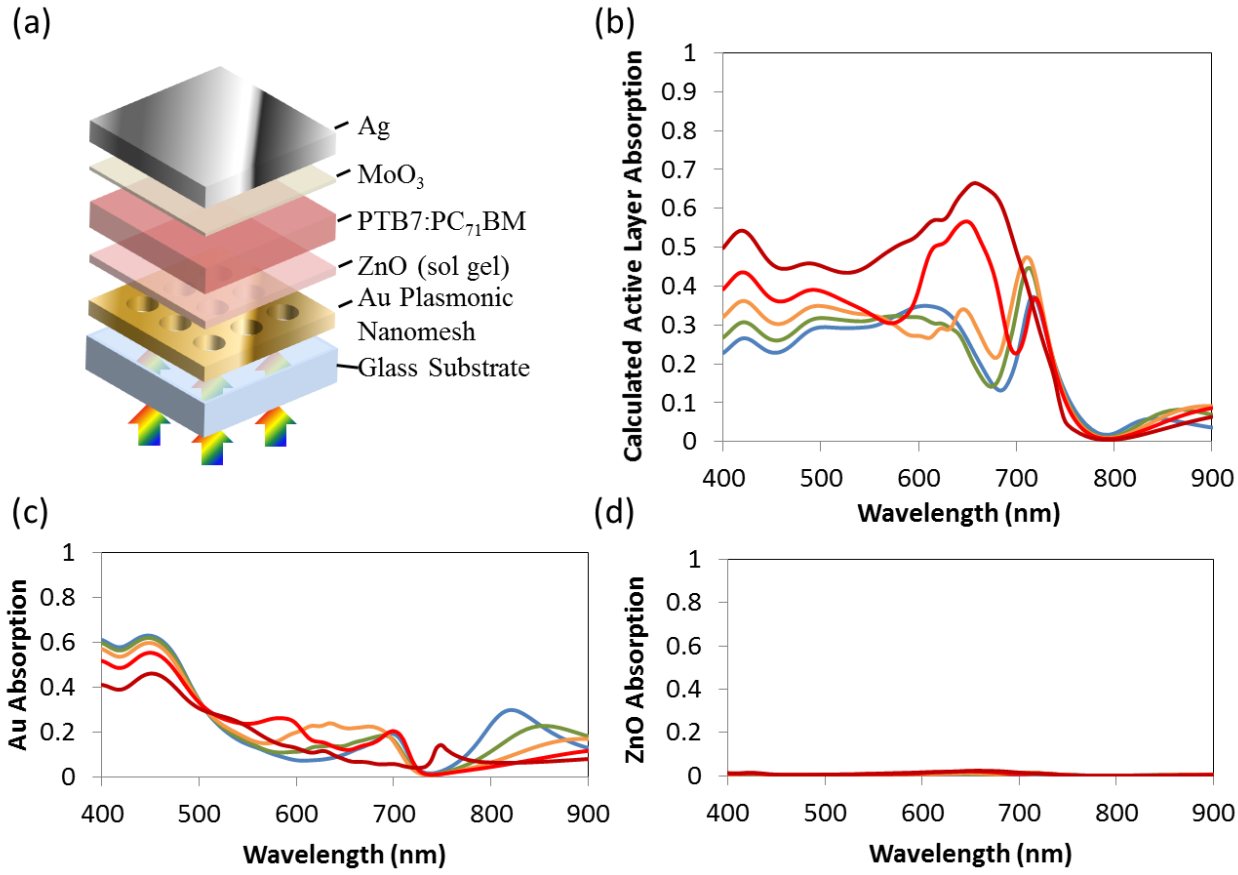

Figure 4-1. (a) Schematic of an inverted device with a plasmonic Au-nanostructured cathode. FDTD calculated (b) active layer absorption, (c) Au absorption and (d) ZnO absorption as a function of wavelength for an inverted OPV device with a Au-nanohole plasmonic electrode. The pitch was kept at 225 nm while the hole diameter was varied as follows: 100 nm (blue), 125 nm (green), 150 nm (orange), 175 nm (red) and 200 nm (dark red).

Figure 4-2(a) shows the calculated reflectance from these devices and clearly shows increasing nanohole size reduces light reflection away from the device. This is to be expected from a geometrical point of view as larger holes indicate less metal is present which would provide increased light transmittance into the device. However, depending on the nanostructure design, light transmission may not always follow this trend as surface plasmon resonance (SPR) plays a role in the light transmission and coupling through the structure. As seen in Fig. 4-2(b), the electric field intensity at the nanostructure interface of the 175 nm holes (red) and the 200 nm holes (dark red) shows large peaks centered around 573 nm and 533 nm, respectively. This peak in the electric field is significantly larger for the 175 nm and 200 nm holes than for any of the others. For these nanostructure designs, the local electric fields in the vicinity of the Au nanoholes are greatly enhanced due to localized surface plasmon resonances (LSPRs). Figure 4-2(c) shows the enhanced local electric field at the Au/ZnO interface at the wavelength of 573 nm, i.e. the peak observed in Fig. 4-2(b) for the nanohole diameter of 175 nm. Figure 4-2(d) shows the cross-sectional electric field intensity distribution of this device at the wavelength of 738 nm, i.e. the optical bandgap of PTB7. While LSPRs are bound to the interface of the metal and dielectric, their strong electric fields can further couple with light to enhance transmission into and trapping inside a device. For a nanohole array, the transmission can actually be greater than the percentage area occupied by the holes so that even light impinging on the metal between the holes is transmitted.[40] In other words, the periodic nanohole array can act like an antenna in the optical regime due to coupling with the fields of SPPs.

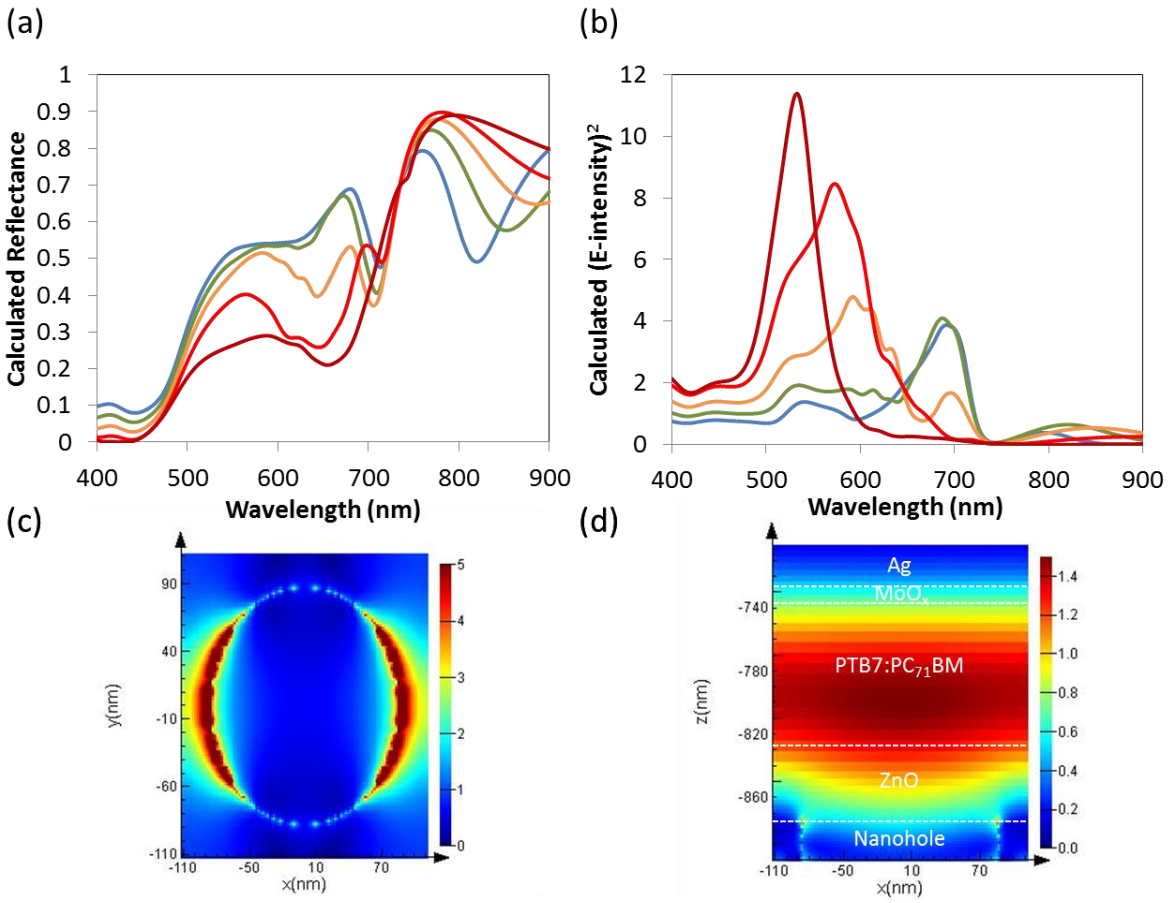

Figure 4-2. FDTD calculated (a) reflectance and (b) electric field intensities (V^2 m^{-2}) at the interface of gold/ZnO, respectively, as a function of wavelength for an inverted OPV device with a Au-nanohole plasmonic electrode. The pitch was kept at 225 nm while the hole diameter was varied as follows: 100 nm (blue), 125 nm (green), 150 nm (orange), 175 nm (red), 200 nm (dark red). (c) Top view of the electric field distribution profile at the gold/ZnO interface at 573 nm (i.e. the peak λ in (b)). (d) Side view of the electric field distribution profile in the device at 738 nm (i.e. the optical E_g of PTB7). Both (c) and (d) are for the plasmonic electrode with a nanohole diameter of 175 nm. The scale bars in (c) and (d) are for E-field (V m^{-1}).

In addition to the nanohole diameter, the pitch of the holes has a large impact on the light absorption in the device. Figure 4-3(a) shows the calculated active layer absorption for inverted devices with a nanohole diameter of 175 nm and varied pitch from 200-300 nm. For this nanohole diameter, the highest active layer absorption is achieved with the 225 nm and 200 nm pitches, i.e. red and dark red lines, respectively, in Fig. 4-3. The Au absorption is relatively

constant and the ZnO absorption is negligible for these cases also, as seen in Fig. 4-3(b). Figure 4-3(c) shows that the high reflectance of the structures with the larger pitch is the primary cause for lower active layer absorption. The electric field intensities shown in Fig. 4-3(d) show a similar trend to before with the higher intensities corresponding to the structures with lower reflectance. As mentioned in the previous discussion, the presence of less metal helps active layer absorption in these design cases.

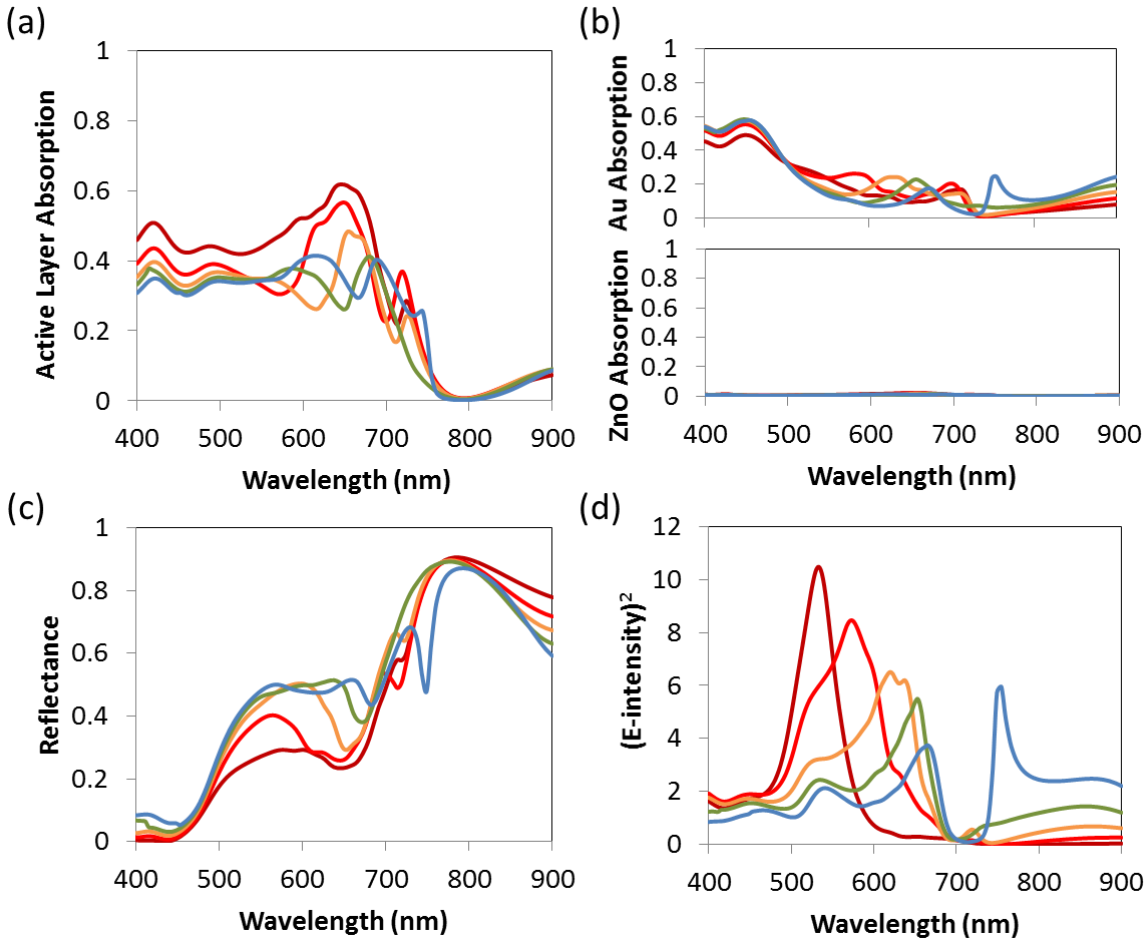

Figure 4-3. FDTD calculated (a) active layer absorption, (b) Au absorption (top) and ZnO absorption (bottom), (c) reflectance and (d) electric field intensity at the interface of gold/ZnO, respectively, as a function of wavelength for an inverted OPV device with a Au-nanohole plasmonic electrode. The nanohole diameter was kept at 175 nm while the pitch was varied as follows: 300 nm (blue), 275 nm (green), 250 nm (orange), 225 nm (red) and 200 nm (dark red).

The design goals are to maximize active layer absorption, minimize device reflectance and maximize the electric field enhancement. With a 225 nm pitch, a nanohole diameter of 175 nm corresponds to a metal "wall" between the nanoholes that is 50 nm thick and that for a 200 nm diameter hole is 25 nm thick. Similarly for 175 nm diameter holes, a 200 nm pitch provides 25 nm thick walls. Due to EBL equipment constraints, a nanopattern with a narrow wall thickness of 25 nm could not be fabricated. Based on these constraints and the simulation results, the nanostructure with the nanohole diameter of 175 nm and the pitch of 225 nm (i.e. 50 nm wall thickness; red lines in Fig. 4-1, 4-2, and 4-3; a.k.a. 175-225 nm) are chosen as the optimum design to be fabricated.

The calculations to design the Au nanostructure used an inverted device with thicknesses of the ZnO electron transport layer (ETL) (~48 nm) and PTB7:$PC_{71}BM$ (~90 nm) optimized on ITO in our previous work.[92] With the 175-225 nm diameter-pitch fixed, these layer thicknesses were varied to achieve a field distribution that maximizes light absorption in the active layer. The thicknesses of MoO_3 (10 nm) and Ag (100 nm) were held constant throughout the simulations. Figure 4-4(a) and (b) compare the simulated active layer absorption and reflectance, respectively, of inverted devices varying the ZnO layer thickness from 20-90 nm. The active layer absorption increases significantly as the ZnO layer is made thinner and the 20 nm thickness results in the highest absorption (see the purple line in Fig. 4-4 (a)). The thickest ZnO film (i.e. 90 nm; pink line in Fig. 4-4(a) and (b)) has the lowest active layer absorption but also the lowest overall device reflectance. This indicates that device reflectance is not the primary factor affecting PTB7:$PC_{71}BM$ absorption for these cases. Figure 4-5(a), (b) and (c) show the active layer, Au layer, ZnO layer and overall device absorption (i.e. calculated from 1-reflectance (R) – transmission (T)) for three inverted devices with 175-225-Au nanostructured

electrodes and ZnO thicknesses of 20, 48 and 70 nm, respectively. The ZnO layer absorption is negligible for each case even as its thickness changes which is expected at wavelengths greater than its band gap. However, the active layer and Au layers show large shifts in absorption as the ZnO thickness changes. The thinnest ZnO layers show increased PTB7:$PC_{71}BM$ absorption with decreased Au absorption. The top Ag electrode and the bottom 175-225-Au nanostructured electrode form a resonant cavity that traps light inside these devices.[48, 78, 82] The optical field distribution and intensity are sensitive to the thickness of the cavity and the thicker ZnO layers shift the peak field intensities closer to the Au nanostructure resulting in increased light absorption in this layer. This is observed in the calculated electric field distributions versus wavelength shown in Fig. 4-5(d), (e) and (f). At wavelengths below the PTB7 E_g, the peak field intensities decrease in the active layer while increasing near the Au nanohole.

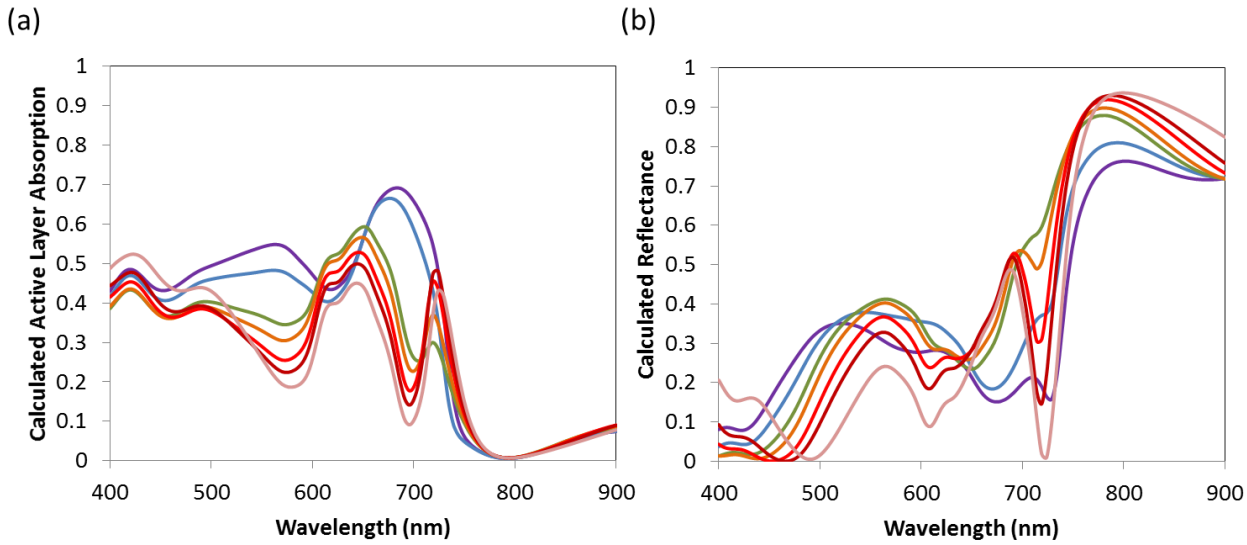

Figure 4-4. FDTD calculated (a) active layer absorption and (b) reflectance for inverted devices with a 175-225-Au (25 nm) (i.e., diameter-pitch Au (thickness)) electrode and the ZnO layer thicknesses varied as follows: 20 nm (purple), 30 nm (blue), 40 nm (green), 48 nm (orange), 60 nm (red), 70 nm (dark red) and 90 nm (pink).

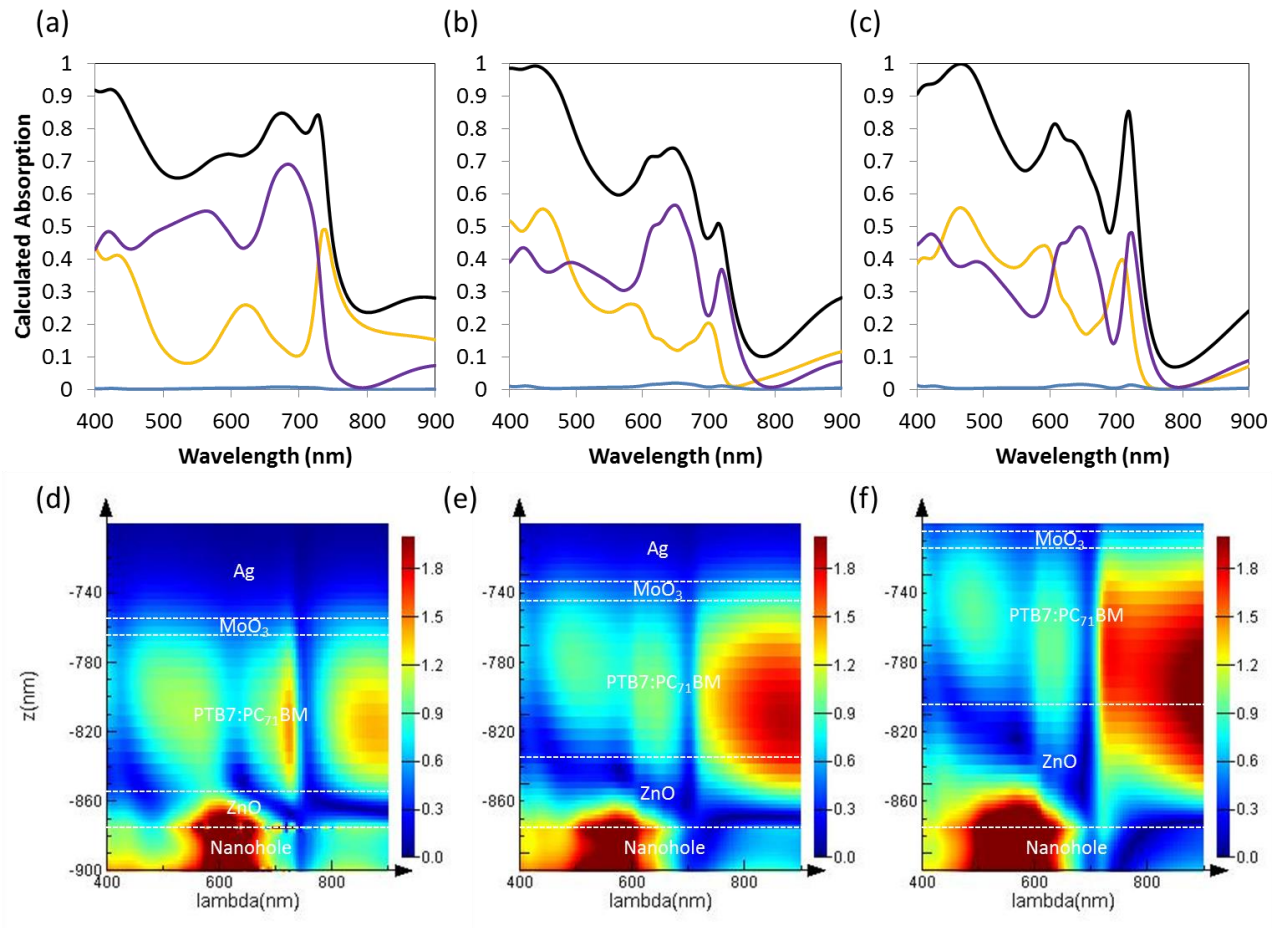

Figure 4-5. FDTD calculated absorption of the active layer (purple line), Au layer (gold line), ZnO layer (blue line) and overall device (A=1-R-T, black line) for inverted devices with 175-225-Au (25 nm) electrodes and ZnO thicknesses of (a) 20 nm, (b) 48 nm and (c) 70 nm. FDTD calculated electric field distribution profiles above the Au "wall" versus wavelength for inverted devices with (d) 20 nm, (e) 40 nm and (f) 70 nm ZnO layers.

Figure 4-6 compares the active layer absorption as the active layer thickness is varied for inverted devices on ITO (dotted lines) and 175-225-Au (25 nm) (solid lines) with thin 20 nm thick ZnO layers. For ITO-based devices using PTB7, the optimal active layer thickness is typically around ~85-95 nm for the optimal balance of maximized light absorption to minimized recombination.[92] The ITO-based devices show active layer absorption increases steadily with PTB7:$PC_{71}BM$ film thickness with a significant jump between the 40 nm and 70 nm conditions. The absorption at 90 nm and 110 nm is very similar and actual devices with these conditions

would be expected to exhibit similar J_{SC}'s with a slightly lower FF for the thicker BHJ due to increased recombination, thus designating the 90 nm thickness as approximately optimal. Optical calculations using the transfer matrix method also showed a sharp increase in J_{SC} as active layer thickness is increased from 40 to ~90 nm but little change when increased further to 110 nm.[92] For devices with the nanostructured electrodes, a similar jump in absorption is seen from 40 to 70 nm but the active layer absorption does not increase further as the BHJ thickness is raised to 90 and 110 nm. With thicker active layers, the ITO-based devices show higher active layer absorption than the devices with 175-225-Au (25 nm) nanostructured electrodes indicating that the J_{SC} for these ITO-free devices may only reach ~50-70% of the ITO controls. However, as the active layer thickness is decreased, the ITO-based devices show larger drops in absorption compared to those with nanostructured electrodes indicating their J_{SC} can approach that of the ITO control devices.

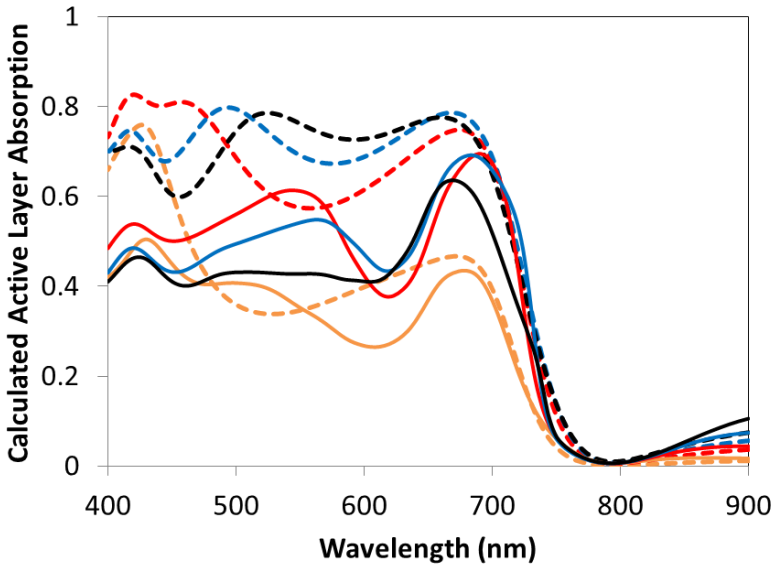

Figure 4-6. FDTD calculated absorption of inverted devices on ITO (dotted lines) and 175-225-Au (25 nm) (solid lines) with 20 nm ZnO and varied active layer thicknesses of 40 nm (orange), 70 nm (red), 90 nm (blue) and 110 nm (black).

Fabrication of Au nanostructures on glass and other substrates typically requires a "glue" layer like Cr or Ti. Figure 4-7 compares the active layer absorption of devices with varied active layer thicknesses on ITO, Cr (2 nm)/Au (23 nm) and Au-only (25 nm) nanostructured electrodes with the 175-225 nanopatterns. It is clear that the addition of the Cr glue layer impacts the properties of the plasmonic cavity and appears to significantly reduce absorption in the region around ~700 nm. In order for devices with the nanostructured electrodes designed here to approach the performance of ITO-based OPVs, finding alternatives to the Cr glue layer may be necessary.

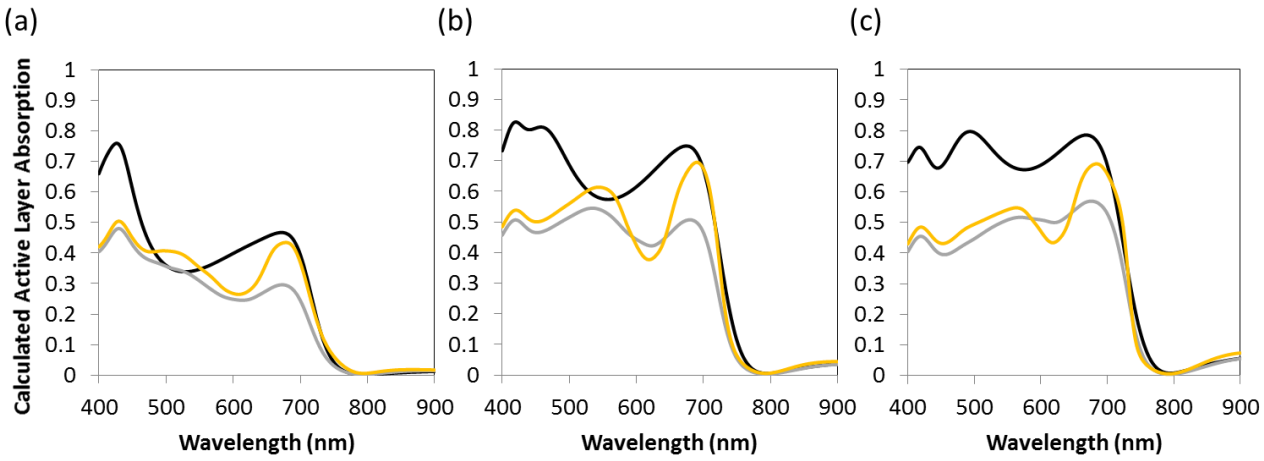

Figure 4-7. FDTD calculated active layer absorption on ITO (black lines), Cr (2 nm)/Au (23 nm) (grey lines), and Au (25 nm) (gold lines) substrates with active layer thicknesses of (a) 40 nm, (b) 70 nm and (c) 90 nm. All have 20 nm thick ZnO.

Based on the simulations described above, Au nanostructures with the 175-225 nm design and 25 nm thickness were targeted for ITO-free OPVs. Once these nanostructured electrodes are fabricated, careful control of the layer thicknesses within each device are important to take advantage of resonant cavity effects and maximize active layer absorption to achieve J_{SC}'s and overall PCEs approaching the ITO-based control devices. Fabrication of Au-

only nanostructures with alternative "glue" layers to Cr will also improve performance and require new fabrication techniques that will be discussed later.

4.3.2. Fabrication of Plasmonic Nanostructured Electrodes

The FDTD simulation results provided the initial design for the nanostructured electrodes. A silicon master mold with 175 nm diameter and 225 nm pitch nanopillars was made using electron beam lithography (EBL) and reactive ion etching (RIE) methods. Using this master mold, we performed a multi-step procedure involving nanoimprint lithography (NIL) to fabricate the actual electrodes for devices. Figure 4-8 shows the primary fabrication steps. The basic steps include NIL of an ETFE sub-mold from the silicon master, NIL of resist on glass from the ETFE, etching, metal deposition, and lift-off to leave the final pattern. Fabrication details are included in the experimental section.

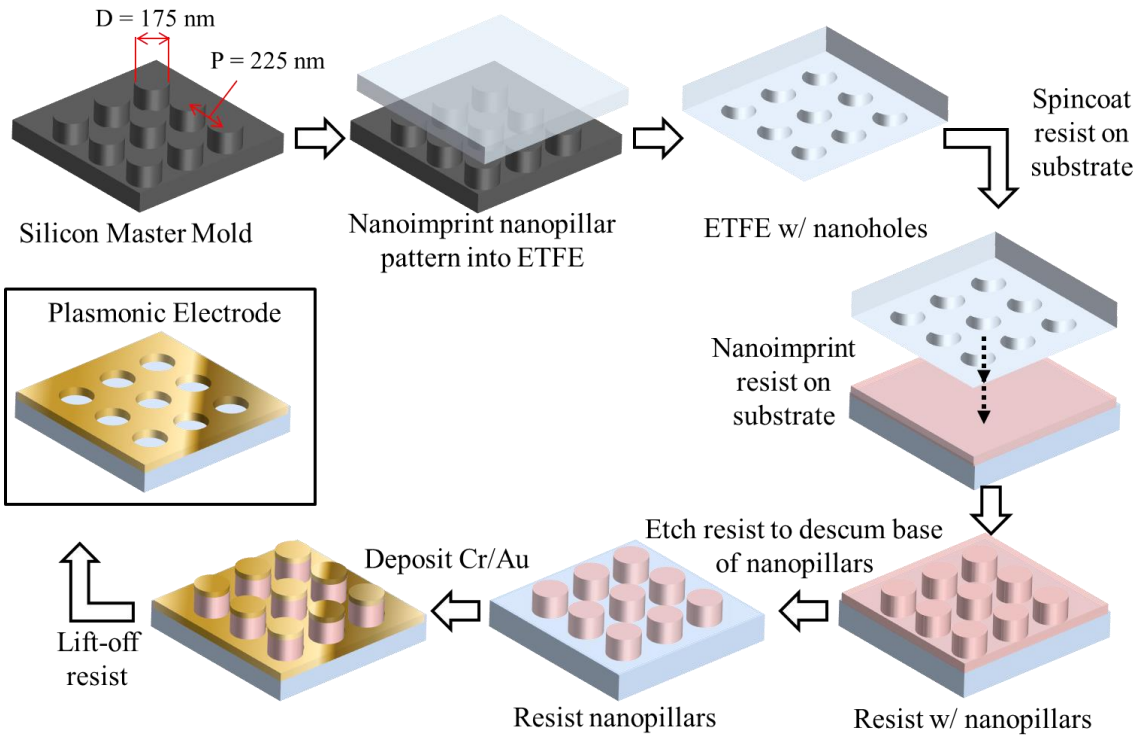

Figure 4-8. The basic fabrication process using nanoimprint lithography to make substrates with plasmonic nanohole array electrodes.

The fabrication procedure shown in Fig. 4-8 may appear straight forward; however, several processing challenges were encountered before quality nanopatterns could be achieved. Significant effort was put forth on procedural tuning and troubleshooting steps to solve these challenges. For instance, the concentration and spin coating speed of the resist were varied to find an optimal film thickness that had enough material present to mold sufficiently to the silicon master while also keeping the film thickness around the pillars thin enough to eliminate overly long dry etching times that damaged the pillars. The dry-etching time was also varied in conjunction with these parameters to find the optimal balance. Initially, only Au was deposited on the structures but the solution lift-off steps were harsh enough to remove the resist and the Au requiring the addition of a Cr "glue" layer. Figure 4-9(a-c) show SEM pictures of the nanopillars on the silicon master mold, the imprinted nanoholes on the ETFE sub-mold, and the imprinted nanopillars in resist on glass after Cr (2 nm) /Au (28 nm) deposition, respectively. The pattern from the silicon master mold transfers nicely to the ETFE and on to the resist sample. However, as shown in Fig. 4-4(d), the nanopillars and Au disks on top of them appear to be intact and relatively unaffected by the solution lift-off process. The lift-off procedure is designed to dissolve the leftover resist essentially lifting off the nanopillars along with the top Au disks leaving behind only the Au nanohole pattern. Note that some areas of the film had exposed nanoholes without the "Au-tops" but much of the film looked as shown in the figure.

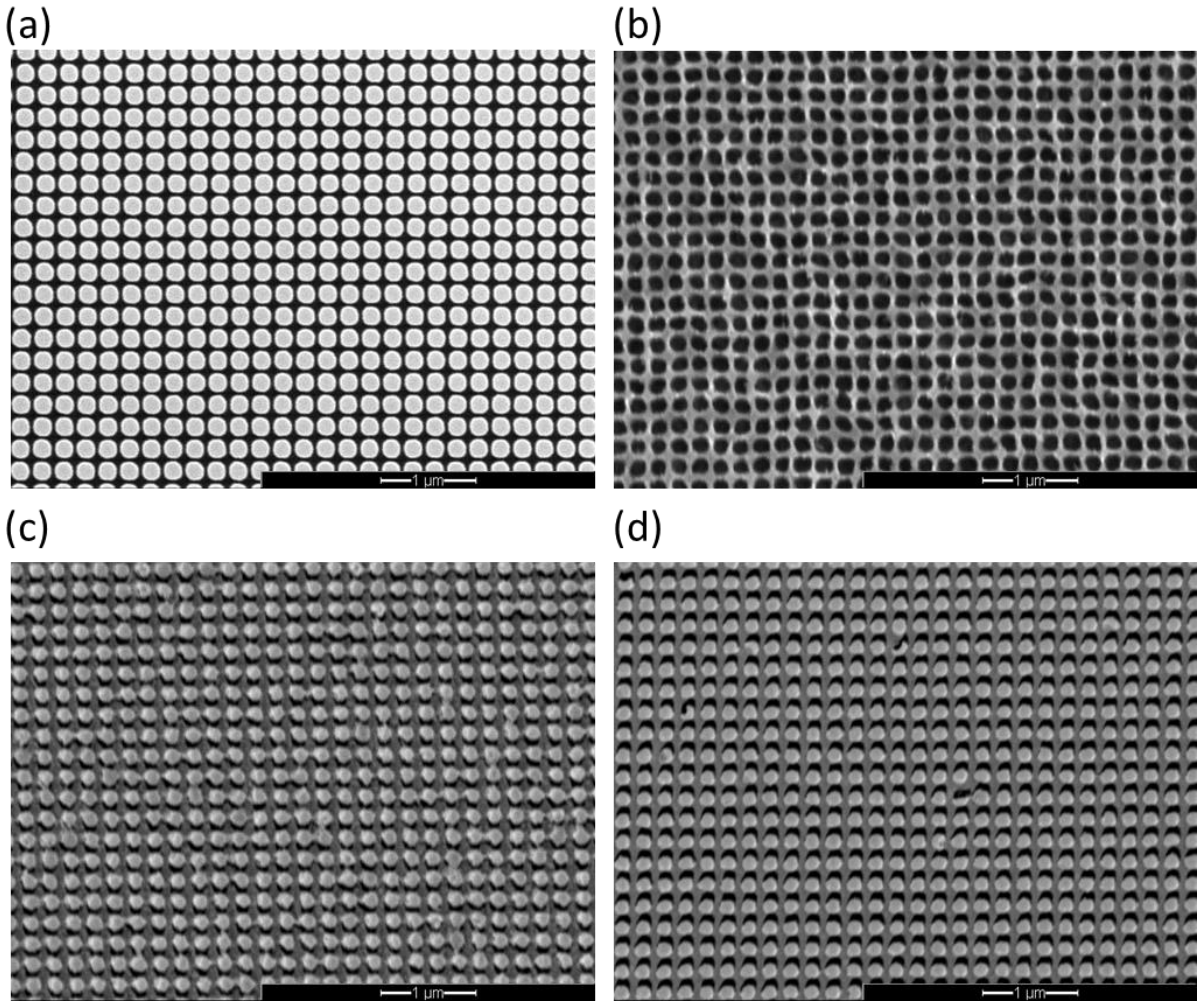

Figure 4-9. SEM images with x20k magnification of (a) the silicon master mold, (b) the imprinted ETFE sub mold, (c) an imprinted resist sample after Cr/Au evaporation and (d) after solution lift-off.

Upon closer inspection, it was observed that the resist does appear to have dissolved away in the lift-off process but the "Au-tops" were left in place. Figure 4-10 (a-b) show tilted views of the nanopattern to reveal apparent bridging elements connecting the "Au-tops" to the Au-nanohole pattern underneath. For clarity, this bridging effect is depicted in the schematic in Fig. 4-10(c). Intuitively, this structure would seem to reduce light transmission through the nanostructure as the "Au-tops" block and scatter light coming through the holes underneath. Further troubleshooting was required to fabricate the open Au-nanohole structure.

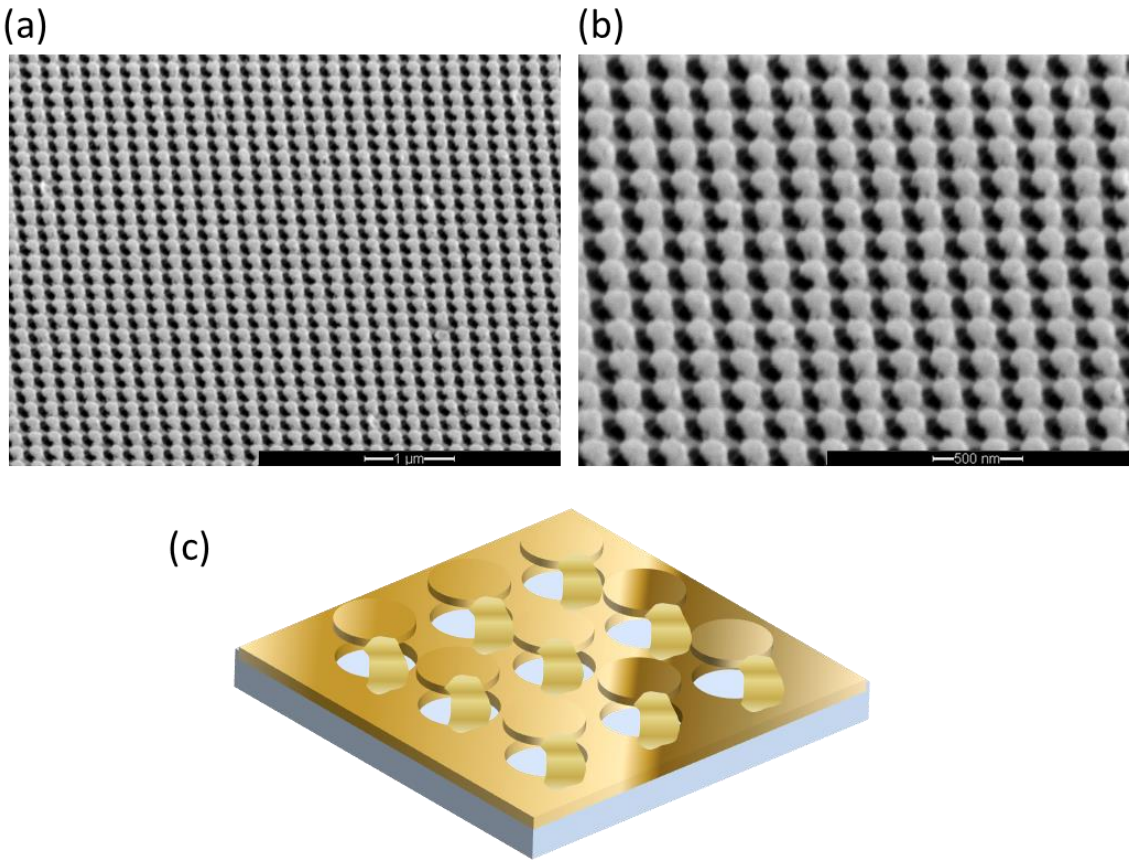

Figure 4-10. Tilted SEM images of (a) an imprinted resist sample after Cr/Au evaporation and solution lift-off (x20k) and (b) a zoom in view (x40k) of (a). (c) A schematic of the effect seen in (a) and (b) where the Au-disks on top of the resist nanopillars are bridged to the Au-nanohole array below. This prevents removal of many of the Au-disks even after solution lift-off to dissolve the resist.

Additional steps were taken to fabricate the desired nanohole structure and included altering the Au evaporation procedure and developing a peel-off procedure. To reduce the effect of shadowing during evaporation, a different evaporation machine with more precise sample alignment was used and the Au layer thickness was reduced from 28 to 23 nm with a Cr thickness of 2 nm. This helped reduce the bridging but did not solve the problem alone. Next, a peel-off procedure was added after the solution lift-off step. This peel-off procedure had to be optimized itself and involved covering the nanopatterns in an optical adhesive, UV-curing the

adhesive, and carefully peeling off the cured material. This peel-off essentially removed the more loosely held "Au-tops" while leaving the Au nanohole structure in place. The combined processing steps and peel-off procedure greatly improved the final nanopattern quality, as shown in Fig. 4-11 (a-d). Also, varying the dry etching time for resist nanopillars allowed for nanoholes of different sizes to be made. Figure 4-11 (a-b) show the nanopattern with a 30 s etch time and average hole diameter of ~172 nm. Figures 4-11 (c) and (d) show the nanopatterns with etch times of 60 and 72 s giving slightly smaller nanoholes with average diameters of ~159 and ~152 nm, respectively. This is a valuable tool to experimentally examine the effects of hole size with constant pitch.

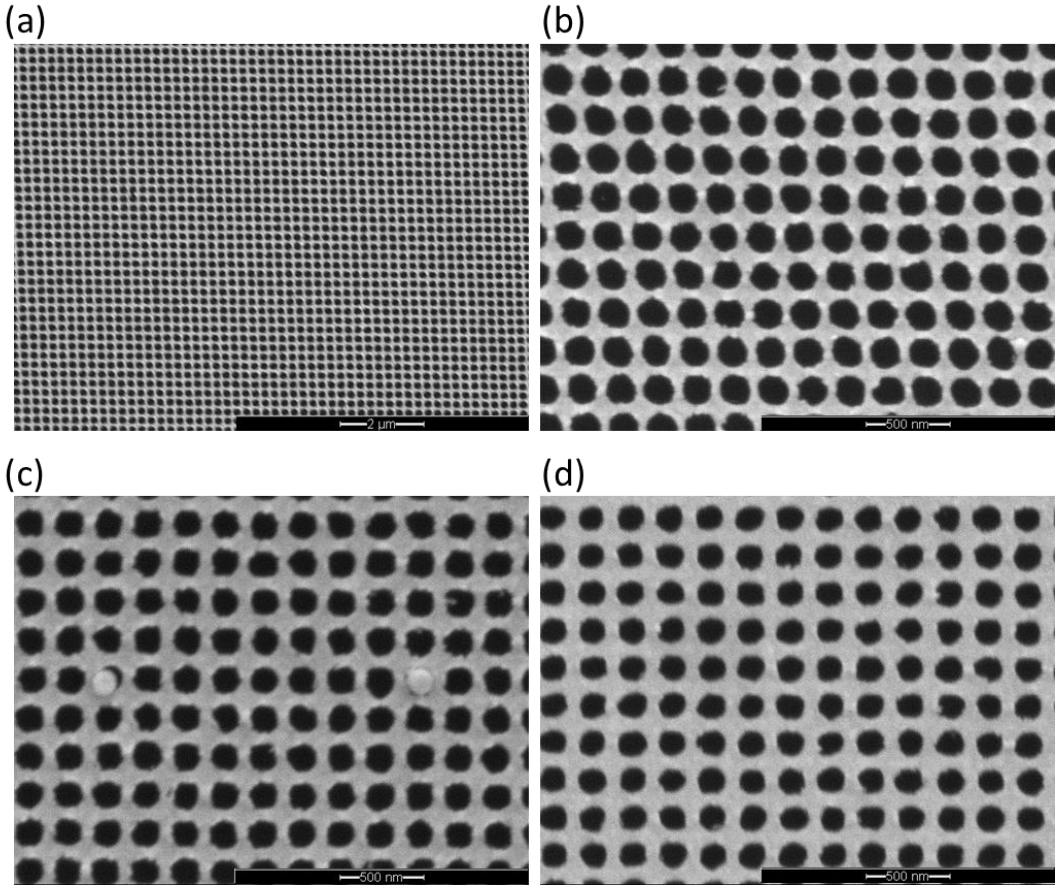

Figure 4-11. SEM images of Au nanoholes on glass made with different spans of oxygen plasma etching followed by metal deposition, solution lift-off and peel-off. Etch time and average diameter are (a,b) 30 s (~172 nm), (c) 60 s (~159 nm) and (d) 72 s (~152 nm).

As mentioned previously, simulation results suggest that device performance would benefit from eliminating the Cr "glue" layer. Thus, we deployed a self-assembled monolayer (SAM) of 3-mercaptopropyltrimethoxysilane (MPTMS) as a molecular adhesive to bond Au to our substrates without the need for Cr.[89] In order to form the SAMs, the substrates were first cleaned and treated with oxygen plasma to generate surface hydroxyl groups (-OH) and then placed under vacuum in a desiccator with a small volume of MPTMS for several hours. This procedure allows co-condensation of the methoxy ($-OCH_3$) groups of MPTMS with the surface hydroxyl groups of the substrate.[87, 89] The NIL process described previously works well to make quality nanopatterns using Cr as the "glue" layer. However, the use of MPTMS SAMs was combined with the NIL procedures under various fabrication pathways but did not produce patterns of sufficient quality.

As an alternative to NIL, we explored a method known as microcontact printing (μCP) which may also be better suited to increase nanostructured electrode area with our current silicon mold.[86] This method allows a composite polydimethylsiloxane (PDMS)/hard-polydimethylsiloxane (h-PDMS) stamp to be made from the silicon master mold. Figure 4-12 shows SEM images of nanopatterns transferred to a composite PDMS/h-PDMS stamp. Note that these stamps are quite robust as this one had been used greater than 20 times when these images were captured. The composite PDMS stamp is coated with alkanethiol molecules and then stamped onto the gold-coated substrate. The thiol molecules form a SAM on the Au surface that mirrors the nanopattern from the stamp. The SAM protects the Au layer so that when the substrate is etched only the unprotected areas are removed. This method allows for the nanopattern to be easily stamped onto a substrate of any size at the desired locations. Adaptation of this method to our procedures and materials system required testing and optimization of

numerous conditions. For example, the stamp time needed to be tuned so that enough alkanethiols transfer to the Au to protect the metal while not oversaturating the surface causing loss of nanopattern resolution. Additionally, the etching time required tuning to find the condition to fully develop the nanopattern without damaging it. The thiol and etching solution concentrations also required testing and careful control. Nanopattern transfer was achieved with μCP, however, the nanohole patterns lacked fine resolution and it was determined that this method is not practical or reliable for use with nano-features as small as ours. One possible reason for this is that the alkanethiol molecules inside the nanoholes on the PDMS stamp migrate down to the substrate due to the small nanohole depth (less than ~140 nm). Other methods related to μCP were also explored, including nanotransfer printing (nTP) and solvent-assisted nanomolding (SAN).[86, 87]

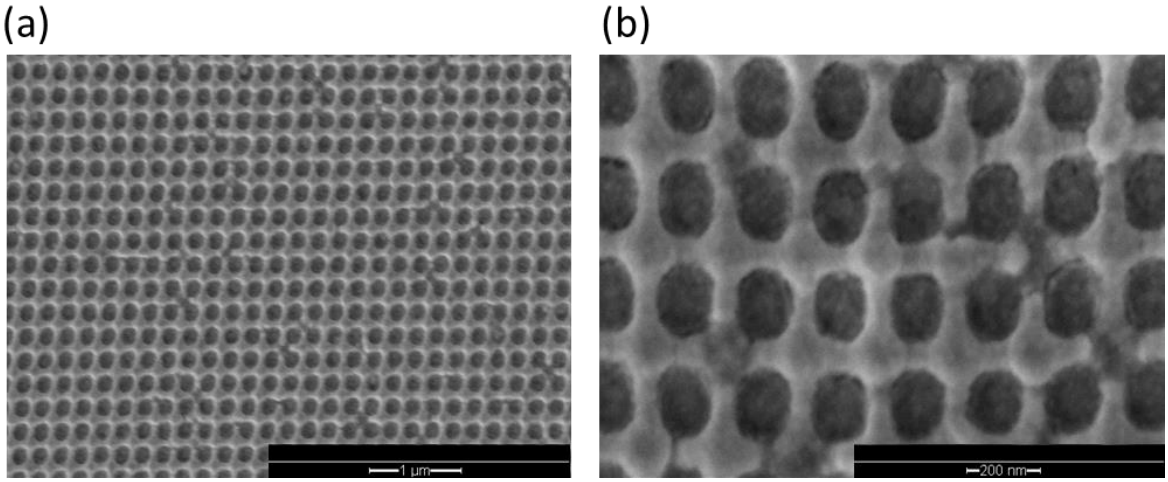

Figure 4-12. SEM images of nanopatterns transferred into a composite PDMS/h-PMDS stamp at magnifications of (a) 20kX and (b) 80kX.

The SAN method is similar to μCP in that it uses a composite PMDS/h-PDMS stamp to transfer the nanopattern from the silicon master mold to the desired substrate. However, SAN

does not use alkanthiols on the stamp as the transfer medium. Instead, the substrate is silanized with MPTMS and then spin coated with poly(methyl methacrylate) (PMMA) which is used as a resist. The stamp is coated with a small drop of acetone and placed on the heated PMMA-coated substrate allowing the PMMA to soften and mold around the nano-features of the stamp. The stamp is left in place for several minutes with heating to evaporate the acetone and cure the PMMA. Then the stamp is removed leaving behind PMMA nanopillars. The residual PMMA at the foot of the pillars is removed by etching in oxygen plasma followed by deposition of Au and lift-off of the nanopillars in acetone to leave behind the final nanohole array. Figure 4-13 summarizes the fabrication steps using SAN. Similar to the μCP method, much work was required to tune the procedure for our nanopatterns including finding the optimal PMMA thickness, etching time and power.

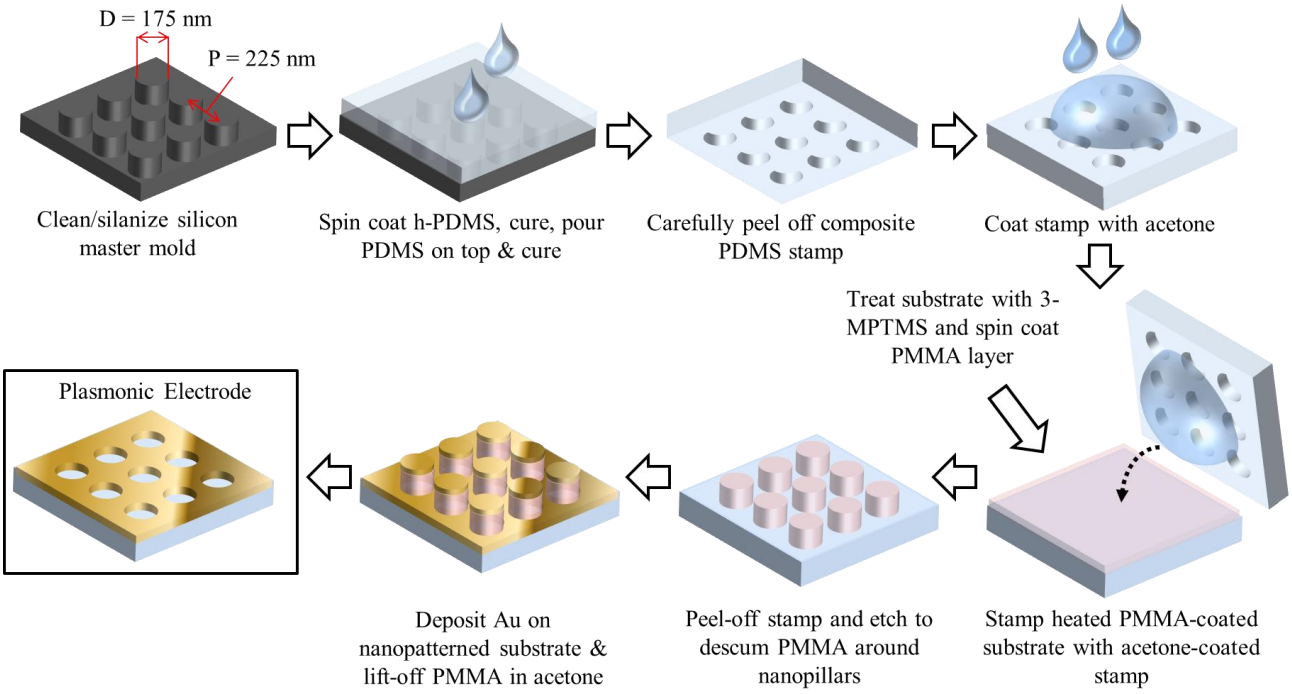

Figure 4-13. The basic fabrication process using solvent-assisted nanomolding (SAN) to make substrates with plasmonic nanohole array electrodes with an MPTMS SAM to replace the Cr "glue" layer.

High quality, Au-only nanostructures were achieved with the SAN method as seen in Figure 4-14(a-d). However, only small areas of open nanoholes are seen after the solution lift-off process in acetone as shown in Fig. 4-14(a,b). Most of the nanopatterned area is still covered by the "Au-tops" as seen in Fig. 4-4(c, d), similar to what is observed with the NIL method. This problem may be solved by a peel-off procedure as used in the NIL method. However, the peel-off method used with NIL was performed with these glass/MPTMS/Au nanostructures and the entire nanopatterns were removed. This is likely due to weaker bonding of the MPTMS SAMs to the substrates compared to Cr which may stem from less dense MPTMS coverage compared to the 2 nm thick evaporated Cr layers used with NIL. A new peel-off procedure is being developed by exploring alternatives to the optical epoxy normally used. It is also clear from Fig. 4-14 that the nanoholes fabricated from SAN are smaller compared to those from NIL (see Fig. 4-11(b)). Further tuning of the SAN procedure is required to produce nanoholes of the target diameter of ~175 nm and reduce bridging of these "Au-tops" to the underlying nanohole array.

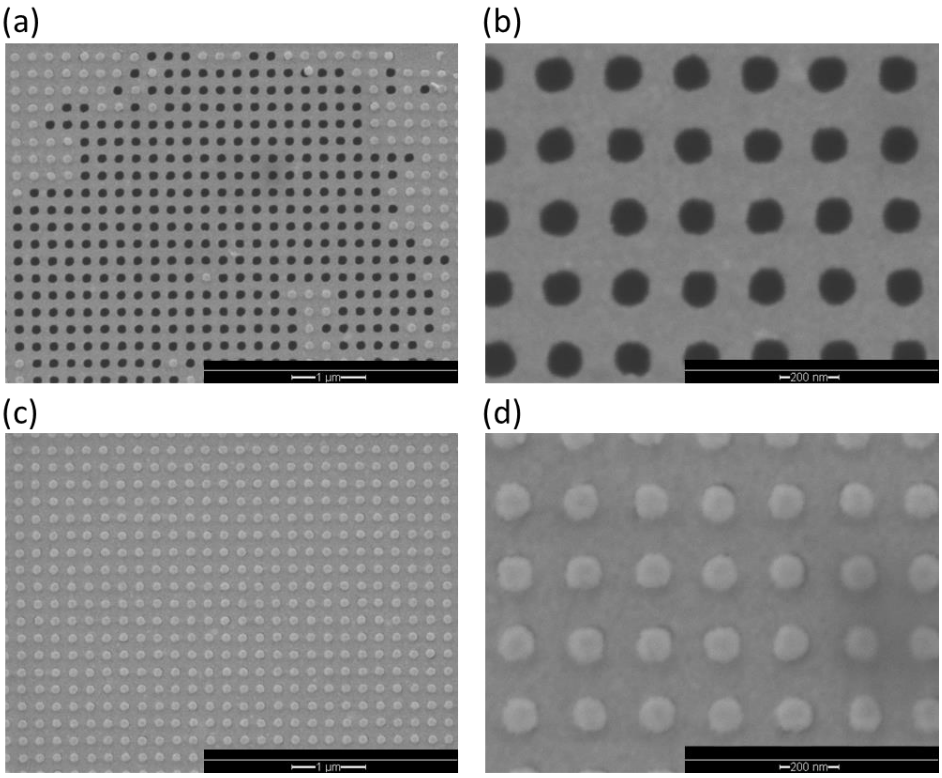

Figure 4-14. SEM images of Au-only nanostructures on glass fabricated with SAN showing an area with (a, b) open nanoholes and (c, d) nanoholes covered by "Au-tops" at magnifications of (a, c) x20k and (b, d) x80k.

The transmission spectra of various substrates were measured and calculated using FDTD simulations as shown in Figure 4-15. The measured transmission of bare glass substrates (light blue solid line) shows broad spectrum transmission of greater than 90% and the measured and simulated spectra for glass/ITO substrates (blue solid and dashed lines, respectively) show reasonable agreement with greater than 80-90% transmission. Measured and simulated spectra of unpatterned Au films on glass (gold solid and dashed lines, respectively) show good agreement and transmission less than 40%. Once a 175-225 nanostructure is put into a Au-only film on glass, the simulated spectra (gold dot-dashed line) shows increased transmission to 50-60% from 400-580 nm with a pronounced dip due to plasmonic absorption at ~610 nm and

greatly increased transmission of 70-90% from ~630-900 nm. However, once a thin Cr "glue" layer is put in place, the simulated transmission of a 175-225 nanostructured substrate (grey dashed line) dampens out to ~40% across the spectrum. The measured transmission of a glass/Cr/Au 175-225 nanostructured substrate shows similar spectra with broad transmission of 40-60%. The Cr layer appears to lower the plasmonic absorption and character of the nanostructure which will dampen the high intensity electric fields of SPPs that act to couple light into the device. This explains the trends seen in Fig. 4-7 that devices with Au-only nanopatterns can have enhanced active layer absorption compared to those with Cr/Au nanostructures. However, even with lower light transmission of these nanostructures compared to ITO, light trapping inside the device by the resonant cavity effect can still yield active layer absorption that is comparable to ITO-based devices. Additionally, these spectra are for bare substrates before they are made into full devices. The properties of plasmonic nanostructures are highly sensitive to the surrounding materials and it has been observed that light reflection and absorption by a bare plasmonic nanostructure reduced 2 to 6 fold when the structures were formed into a complete device.[48] Unlike ITO where the substrate transmission is directly correlated to active layer absorption, the plasmonic properties and resonant cavity effects of these nanostructured electrodes in completed-OPV devices have significant impacts on device performance that are not made evident by bare substrate transmission alone.

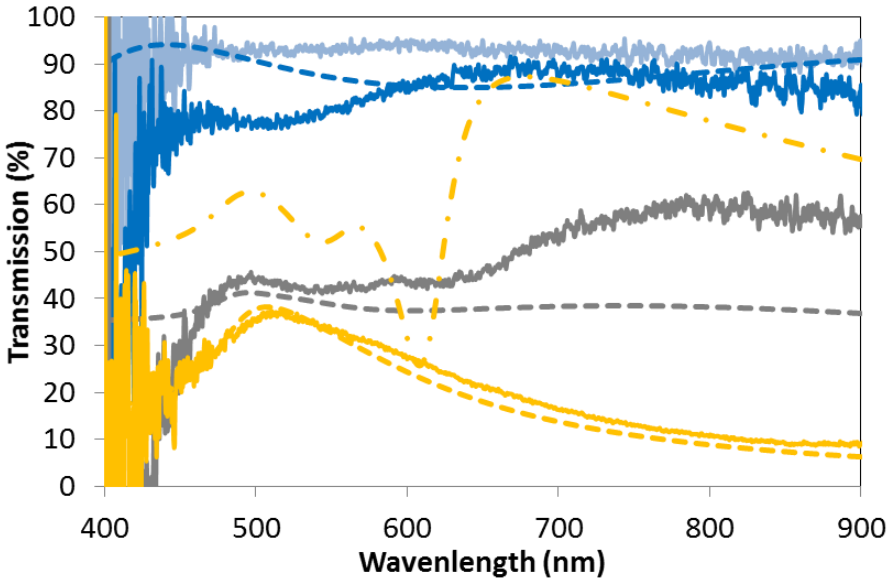

Figure 4-15. Measured (solid lines) and FDTD simulated (dashed lines) transmission spectra of bare glass (light blue solid), glass/ITO (blue solid and dashed), glass/Au unpatterned film (gold solid and dashed), glass/ 2 nm Cr/ 23 nm Au 175-225 nanostructure (grey solid and dashed) and glass/25 nm Au-only 175-225 nanostructure (gold dot-dashed).

4.3.3. Plasmonic Nanostructured Electrodes Deployed in OPVs on Glass Substrates

High quality plasmonic Au-nanostructures with Cr "glue" layers were fabricated using NIL and tuned lift-off/peel-off procedures. These Cr/Au nanostructures, as seen in Fig. 4-11(a,b), were deployed on bare glass substrates as cathodes in ITO-free inverted devices with the structure shown in Figure 4-16(a). ITO-free OPV devices with a power conversion efficiency (PCE) as high as 5.70% were achieved. Figure 4-16(b) shows the current-voltage curves of devices on ITO versus those on Cr/Au nanostructures with ~32 nm thick ZnO ETLs and varied active layer thicknesses. These ZnO ETLs were formed using the sol gel method with a 0.3 M precursor solution spun at 2000 rpm and baked under static conditions. For each active layer thickness, the ITO and Cr/Au nanostructure-based devices had approximately equal V_{OC}'s and FF's, shown in Table 4-1, indicating that the electrical characteristics of these two types of

electrodes are very similar in these OPVs. The primary difference in PCE between these two cathodes was due to a lower J_{SC} for devices with Cr/Au nanostructures. For a thicker active layer of ~122 nm, both types of devices show lower FF's due to increased recombination as compared to the devices with thinner active layers. The J_{SC} of the nanostructured device is 61% of the ITO-based devices (i.e. 9.82 vs. 15.98 mA/cm^2). As the active layer thickness decreases closer to the optimum at ~93 nm, the J_{SC}'s of the devices increase to 11.80 mA/cm^2 and 17.43 mA/cm^2 for Cr/Au and ITO, respectively. The nanostructured device J_{SC} increased to 68% of that of the ITO control at the optimal active layer thickness. When the active layer thickness is decreased further down to ~77 nm, the J_{SC} of the ITO device drops to 15.90 mA/cm^2 while that of the Cr/Au device remained approximately the same at 11.39 mA/cm^2, which is now 72% of the ITO device. As seen in our previous work, the J_{SC} of these ITO-based devices is very sensitive to active layer thickness with decreased photocurrent observed as the thickness varies above or below the optimum.[92] However, due to the resonant cavity effect created by the nanostructured electrodes, the J_{SC}'s of these ITO-free devices is retained as the active layer becomes optically thin. These performance trends agree with those in the FDTD calculated active layer absorption spectra shown in Fig. 4-6 and Fig. 4-7.

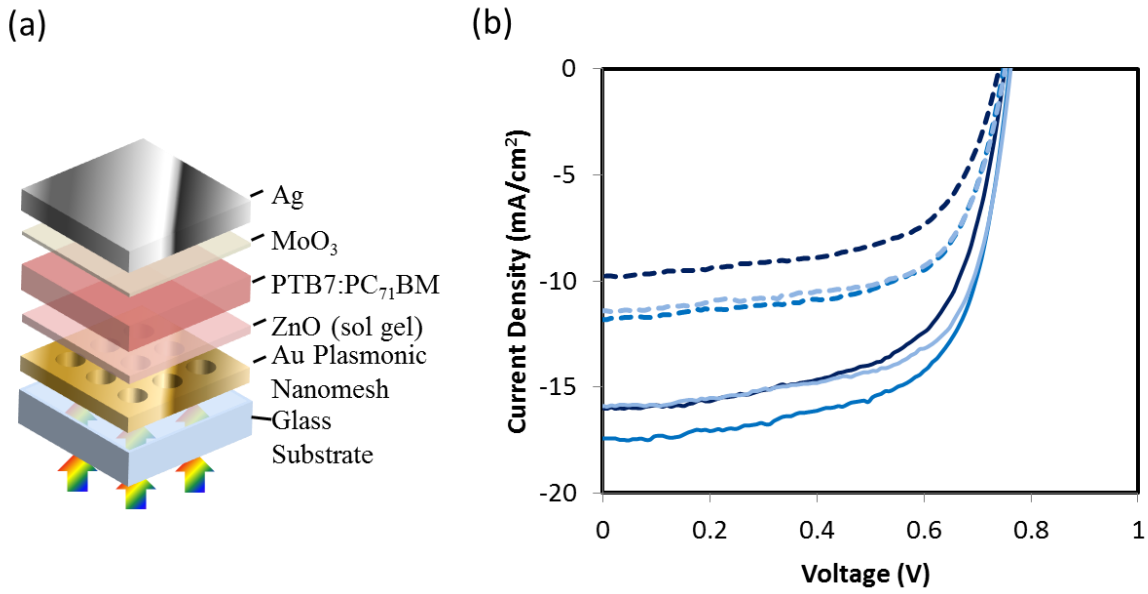

Figure 4-16. (a) Schematic of an inverted device with a plasmonic Au-nanostructured cathode. (b) Current-voltage curves for inverted devices with ITO (solid lines) and Cr/Au nanostructured (dotted lines) cathodes with sol-gel derived ZnO ETLs of ~32 nm thickness and varied active layer thicknesses of ~122 nm (dark blue), ~93 nm (blue) and ~77 nm (light blue).

Table 4-1. The performance parameters corresponding to the J-V curves in Fig. 4-16 for inverted devices on ITO and Cr/Au nanostructured cathodes with ~32 nm thick sol-gel derived ZnO ETLs and varied active layer thicknesses. Active layer film thickness measurements are from profilometry of films on bare glass/ITO.

Substrate	ZnO Thickness (nm)	Active Layer Thickness (nm)	V_{OC} (V)	FF (%)	J_{SC} (mA/cm^2)	PCE (%)
ITO	~32	122 +/- 6	0.75	62.2	15.98	7.46
ITO	~32	93 +/- 16	0.76	64.5	17.43	8.55
ITO	~32	77 +/- 7	0.76	65.9	15.90	7.98
Cr(2nm)/Au(23nm)	~32	122 +/- 6	0.74	61.2	9.82	4.45
Cr(2nm)/Au(23nm)	~32	93 +/- 16	0.75	64.5	11.80	5.70
Cr(2nm)/Au(23nm)	~32	77 +/- 7	0.75	65.2	11.39	5.59

Despite these effects, the Cr/Au-based devices show lower J_{SC}'s and PCE's compared to the ITO controls. The external quantum efficiency (EQE) of a Cr/Au versus ITO device with ~32 nm ZnO ETLs and ~77 nm active layers is shown in Fig. 4-17. The EQE of the devices with

nanostructured electrodes is over 20% lower than the ITO control at wavelengths of ~460-680 nm, in agreement with the simulation results discussed previously. To maximize J_{SC} and EQE, it is important to ensure that the ZnO thickness is optimal for the resonant cavity and to eliminate the need for the Cr "glue" layer which can interfere with the plasmonic properties of the Au film and reduce active layer absorption as mentioned before.

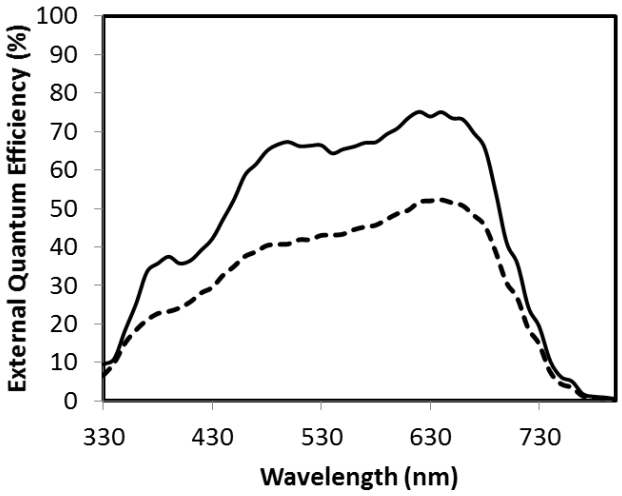

Figure 4-17. External quantum efficiency (EQE) spectra of inverted devices on ITO (solid line) and Cr/Au nanostructured (dotted line) cathodes with ~32 nm thick ZnO and ~77 nm thick active layers.

The reflectance spectra of the ITO and Cr/Au-based devices with ~32 nm ZnO ETLs and ~77 nm thick active layers were measured and compared to spectra of FDTD-simulated devices with similar thicknesses in Figure 4-18. The measured reflectance (solid lines) of ITO and the nanostructured based devices is very close between 550-700 nm averaging ~12%. Despite similar reflectance, the Cr/Au nanostructured device showed a J_{SC} that is ~28% lower than the ITO device. This shows that the difference in active layer absorption between these devices is not due to higher reflectance but likely due to parasitic Au-layer absorption that is not offset by light trapping effects of the resonant cavity. The FDTD-simulated spectra (dashed lines) have similar trends to the measured data but deviate in some wavelength ranges likely due to error in

film thickness and refractive index as well as imperfect nanohole patterns in the experimental devices.

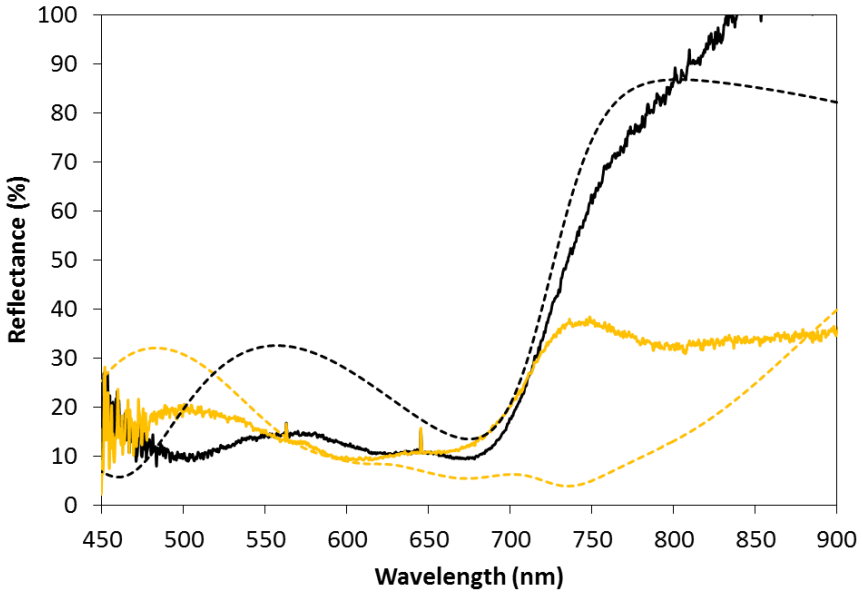

Figure 4-18. Measured reflectance spectra of the ITO (black solid) and Cr/Au-based (gold solid) devices with ~32 nm ZnO ETLs and ~77 nm active layers shown in Table 4-1. The dashed lines show the FDTD-simulated spectra of ITO (black dashed) and Cr/Au-based (gold dashed) devices with similar thicknesses.

In addition, any damage to the nanostructures could adversely affect light transmission and trapping in these OPVs. The ZnO sol gel films made here use a baking temperature of 200°C which can lead to damage of nanometer scale features in thin Au films. However, when baked with the sol gel layer on top, these nanostructures appear intact and unchanged as seen in the SEM images in Figure 4-19.

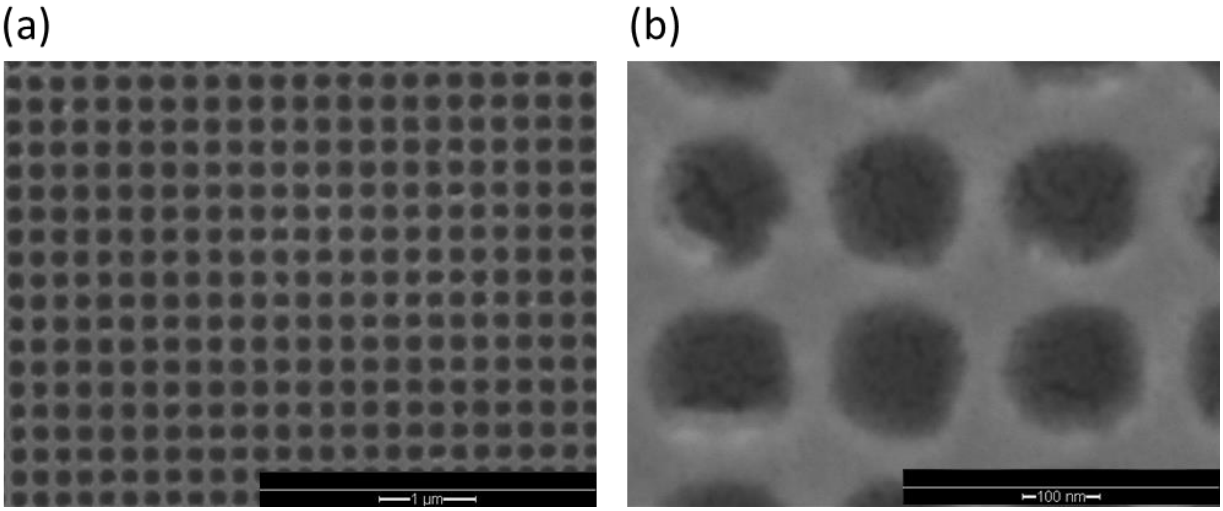

Figure 4-19. SEM images of Cr/Au nanostructures on glass coated with a ZnO sol gel film after baking at 200°C at magnifications of (a) x20k and (b) x160k.

FDTD calculations suggest that minimizing ZnO thickness is ideal for maximizing active layer absorption. The ZnO ETLs in the previously discussed devices were ~32 nm thick and so the thickness was reduced to determine if performance could be improved. Figure 4-20 shows the current-voltage curves and Table 4-2 shows the performance parameters for devices with ~24 nm thick ZnO ETLs. Similar to the devices with ~32 nm thick ZnO, the V_{OC}'s and FF's are approximately constant between the ITO and Cr/Au nanostructured devices at each active layer thickness. However, in this case the J_{SC}'s remain fairly constant for the nanostructured devices as active layer thickness is decreased and are significantly lower than the previous devices with ~32 nm ZnO with values ranging from 8.39-8.86 mA/cm^2. One possible reason for this difference in behavior is that the Cr/Au nanostructures have a total thickness of 25 nm, i.e. the nanoholes are ~25 nm deep. The ZnO thickness of ~24 nm is based on measurements taken from bare glass/ITO substrates. The ZnO sol gel solution appears to fill the nanoholes, as seen in Fig. 4-19, which means that the ZnO thickness on top of the nanostructure itself may be non-uniform and much thinner than 20 nm. In addition to this, small variations in nanopattern quality may also lead to these unpredicted trends.

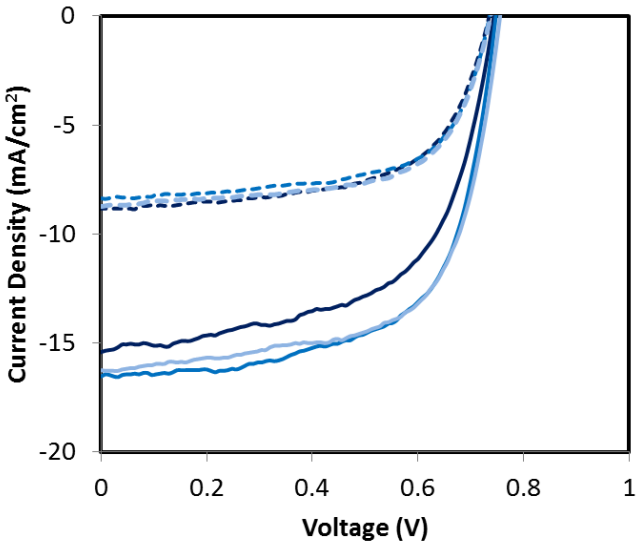

Figure 4-20. Current-voltage curves for inverted devices with ITO (solid lines) and Cr/Au nanostructured (dotted lines) cathodes with ZnO ETLs of ~24 nm thickness and varied active layer thicknesses of ~122 nm (dark blue), ~93 nm (blue) and ~77 nm (light blue).

Table 4-2. The performance parameters corresponding to the J-V curves in Fig. 4-20 for inverted devices on ITO and Cr/Au nanostructured cathodes with ~24 nm thick sol-gel derived ZnO ETLs and varied active layer thicknesses.

Substrate	ZnO Thickness (nm)	Active Layer Thickness (nm)	V_{OC} (V)	FF (%)	J_{SC} (mA/cm^2)	PCE (%)
ITO	~24	122 +/- 6	0.74	58.9	15.41	6.75
ITO	~24	93 +/- 16	0.75	63.9	16.52	7.89
ITO	~24	77 +/- 7	0.76	64.4	16.25	7.91
Cr(2nm)/Au(23nm)	~24	122 +/- 6	0.74	60.9	8.86	3.97
Cr(2nm)/Au(23nm)	~24	93 +/- 16	0.74	63.9	8.39	3.95
Cr(2nm)/Au(23nm)	~24	77 +/- 7	0.74	63.2	8.73	4.07

Nanopatterns with varied nanohole diameters were fabricated using NIL by varying the resist etching time after imprinting yielding sizes of ~172 nm, ~168 nm, ~159 nm and ~152 nm with etching times of 30 s, 48 s, 60 s and 72 s, respectively. These Cr/Au nanostructures were used in inverted devices with thicker ZnO ETLs of ~48 nm. The current-voltage curves and

performance parameters of these devices are shown in Fig. 4-21(a) and Table 4-3, respectively. The nanostructured device etched for 30 s (i.e. the same condition for all previous Cr/Au devices mentioned) shows a V_{OC} and FF that are approximately the same compared to the ITO device but the J_{SC} is 51% lower (see Table 4-3). This device's J_{SC} of 7.52 mA/cm^2 is lower than those of the devices with thinner ZnO ETLs in agreement with FDTD simulations. The EQE spectra in Fig. 4-21(b) clearly show this lower absorption across a broad wavelength range. Also, decreasing the nanohole diameter generally decreased the J_{SC} while it increased the FF. This is in agreement with the calculations mentioned previously and with what we expect intuitively. Decreasing the nanohole size blocks more light from entering the device while the increased metal electrode area from thicker "walls" between nanoholes decreases the series resistance of the electrode. The primary impact of a decreased series resistance is to increase the device FF as we observe. Therefore, electrode sheet resistance and optical transmission, along with the various layer thicknesses, need to be balanced for peak performance.

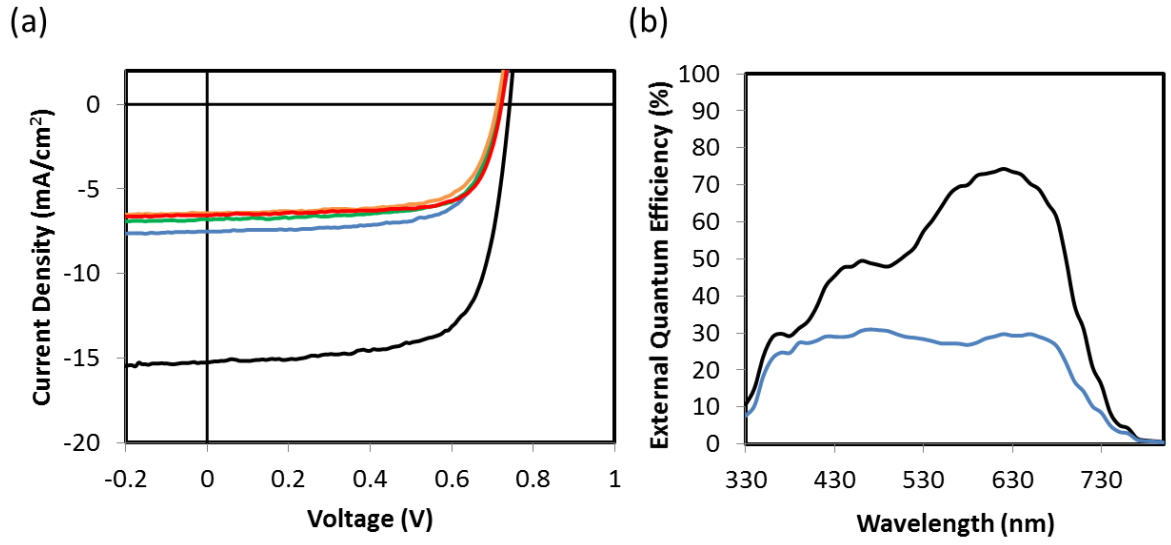

Figure 4-21. (a) Current-voltage curves for inverted devices with thicker 48 nm ZnO ETLs on ITO (black) and Cr/Au nanostructures with varying nanohole diameters of ~172 nm (blue), ~168 nm (green), ~159 nm (orange) and ~152 nm (red). (b) EQE spectra for the ITO device (black) and Cr/Au device with ~172 nm nanoholes (blue) shown in (a).

Table 4-3. The performance parameters corresponding to the J-V curves in Fig. 4-21(a) for inverted devices with sol-gel derived thicker 48 nm ZnO ETLs on ITO and Cr/Au nanostructures with varying nanohole diameters by changing the resist etching time.

Substrate	Etch Time (s)	Avg. Hole Diameter (nm)	V_{OC} (V)	FF (%)	J_{SC} (mA/cm^2)	PCE (%)
ITO	n/a	n/a	0.74	69.8	15.24	7.89
Cr(2nm)/Au(23nm)	30	~172	0.72	68.3	7.52	3.70
Cr(2nm)/Au(23nm)	48	~168	0.72	71.1	6.79	3.47
Cr(2nm)/Au(23nm)	60	~159	0.71	69.9	6.44	3.21
Cr(2nm)/Au(23nm)	72	~152	0.72	72.2	6.57	3.43

The reflectance spectra were measured for the ITO and Cr/Au-based devices with ~48 nm thicknesses shown above and compared to the FDTD-simulated spectra in Figure 4-22. Similar to the devices with the thinner ZnO thicknesses shown previously, these devices show measured reflectance spectra that are close to ~10% from ~550-680 nm. The Cr/Au device shows lower reflectance than ITO from 450-550 nm and from 700 nm to the PTB7 E_g. Yet the Cr/Au device's J_{SC} is ~51% lower than the ITO device indicating that device reflectance is not the primary source of lost active layer absorption between the two cases. The FDTD-simulated reflectance (dashed lines) follows the same general trends as the experimental devices with differences likely due to error in film thickness and refractive index as well as imperfect nanohole patterns in the experimental devices.

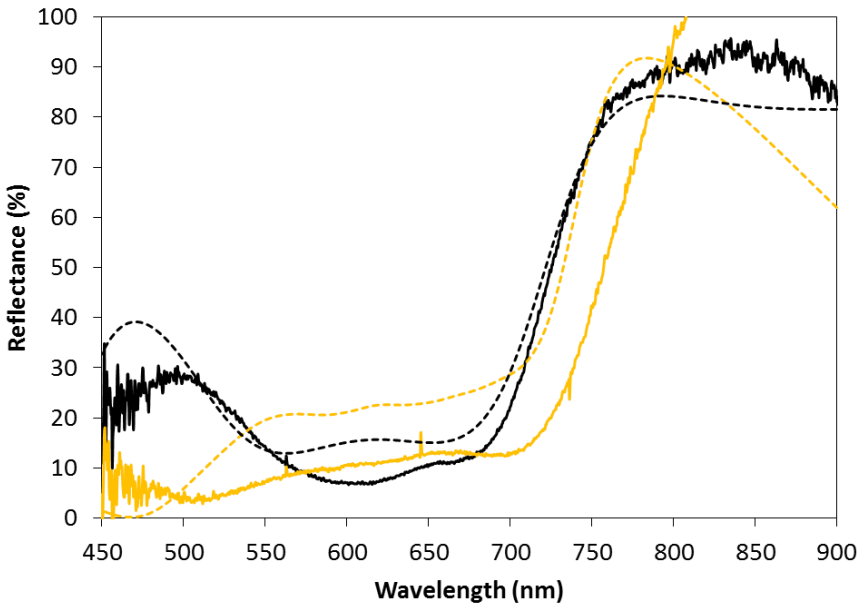

Figure 4-22. Measured reflectance spectra of the ITO (black solid) and Cr/Au-based (gold solid) devices with ~48 nm ZnO ETLs shown in Table 4-3. The dashed lines show the FDTD-simulated spectra of ITO (black dashed) and Cr/Au-based (gold dashed) devices with similar thicknesses.

ZnO films fabricated with the sol gel method typically require baking at 200°C which is not compatible with many flexible substrates. Therefore, we fabricated devices with ZnO NPs synthesized in our lab that do not require a baking step and are formed via a layer-by-layer spin coating method.[91] More detailed discussion of these ZnO NP films will follow in the next section when used with flexible substrates. The current-voltage curves and performance parameters of inverted devices with ~44 nm thick ZnO NP ETLs and active layer thickness of ~103 nm are shown in Figure 4-23(a) and Table 4-4. These devices performed similarly to devices with ZnO sol gel ETLs with a similar thickness of ~48 nm. The V_{OC} and FF are close to the ITO control devices while the J_{SC} is 46% of ITO's. Based on simulation, the ZnO film should be thinner to increase the active layer absorption in these devices as discussed previously. Figure 4-23(b) shows an SEM image of a ZnO NP film coating a Cr/Au nanopatterned electrode.

This film was fabricated by spin coating three sequential layers of the filtered stock ZnO NP solution at 3000 rpm to build up the film that measures ~44 nm on bare glass/ITO substrates. The SEM image shows how the NP coverage is non-uniform with areas of thinner and thicker coverage. Regardless, this condition appears to adequately coat the nanostructure as seen by the normal V_{OC} and FF. However, devices with thinner ZnO NP films (e.g. only one layer spun), were fabricated and measured at ~32 nm on bare glass/ITO substrates (not shown). The control ITO devices at this condition showed typical performance with a PCE as high as 7.06%, however, the devices on Cr/Au nanostructures were shorted and showed no V_{OC}. This is possibly due to a combination of inadequate NP film coverage over the nanostructured electrode with nanostructure defects that penetrate the overlying layers to make contact with the top anode. Devices with thicker ZnO NP ETLs of ~66 nm were also made (not shown) and both the ITO and Cr/Au nanostructure-based devices showed diminished FFs of 58% and 48%, respectively, and lower J_{SC}'s leading to low PCEs of only 5.26% and 2.09%, respectively. Recall that ITO-based devices with ZnO sol gel films showed no sensitivity to thicknesses in this range. The ZnO NP films are more porous with less densely-packed crystalline character compared to the sol gel films leading to higher series resistance for these thick films.

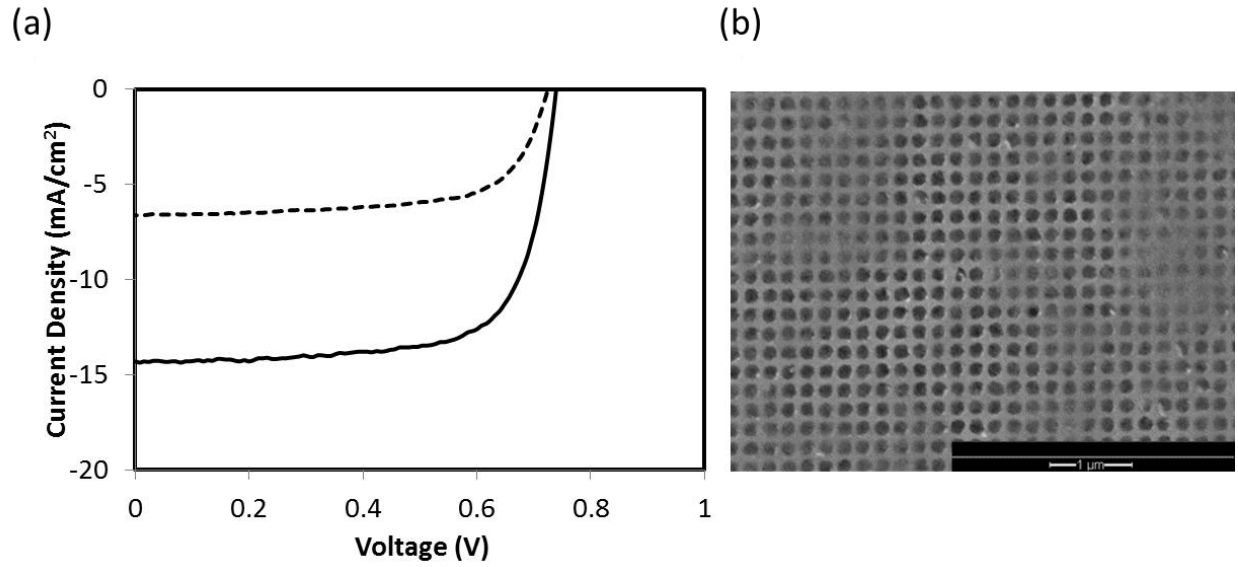

Figure 4-23. (a) Current-voltage curves for inverted devices with ~44 nm ZnO NP ETLs on ITO (solid line) and Cr/Au nanostructured (dotted line) electrodes. (b) SEM image of a Cr/Au nanostructure covered with a ZnO NP film that measured ~44 nm on a bare glass/ITO substrate.

Table 4-4. The performance parameters corresponding to the J-V curves in Fig. 4-23(a) for inverted devices with ZnO NP ETLs on ITO and Cr/Au electrodes.

Substrate	ZnO NP Thickness (nm)	Active Layer Thickness (nm)	V_{OC} (V)	FF (%)	J_{SC} (mA/cm^2)	PCE (%)
ITO	44 +/- 8	103 +/- 15	0.74	71.7	14.31	7.58
Cr(2nm)/Au(23nm)	44 +/- 8	103 +/- 15	0.72	68.0	6.60	3.25

In addition to controlling the ZnO layer thickness, simulation results suggest that eliminating the Cr "glue" layer in the nanostructured electrodes can further enhance active layer absorption in these devices. A new fabrication technique, i.e. SAN, was used to make Au-only nanostructures as seen in Fig. 4-14. As discussed, these Au-only nanostructures have small areas of open nanoholes but are largely composed of nanoholes still covered by "Au-tops" and new procedures are being developed to resolve this issue. Still, these preliminary Au-only

nanostructured electrodes were deployed in inverted devices and the current-voltage curves and performance parameters are shown in Figure 4-24 and Table 4-5, respectively. These devices show similar V_{OC} to the ITO and Cr/Au-based devices and a higher FF likely due to smaller nanohole diameters and the presence of more Au area. The J_{SC} of the Au-only device is 6.11 mA/cm^2 which is only 38% of that of the ITO device. Still, even with diminished transmission into the device due to the non-ideal nanostructure, the PCE reached 3.14% showing promise for making high efficiency devices with optimized Au-only nanostructures.

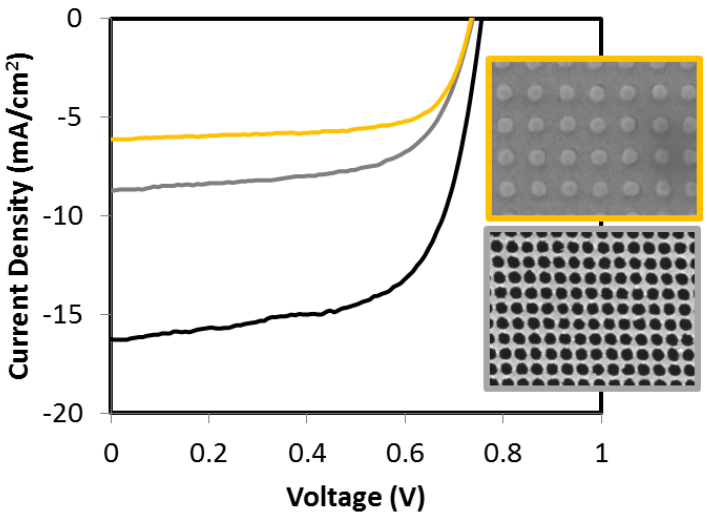

Figure 4-24. Current-voltage curves for inverted devices with ITO (black), Cr/Au (grey) and Au-only (gold) nanostructured electrodes with ~24 nm ZnO ETLs and ~77 nm thick active layers. The top inset is an SEM image of a Au-only nanostructure with smaller holes and large areas covered with unlifted Au disks and the bottom inset is that of a Cr/Au nanostructure.

Table 4-5. The performance parameters corresponding to the J-V curves in Fig. 4-24 for inverted devices on ITO, Cr/Au and Au-only nanostructured electrodes.

Substrate	ZnO Thickness (nm)	Active Layer Thickness (nm)	V_{OC} (V)	FF (%)	J_{SC} (mA/cm^2)	PCE (%)
ITO	~24	77 +/- 7	0.76	64.4	16.25	7.91
Cr(2nm)/Au(23nm)	~24	77 +/- 7	0.74	63.2	8.73	4.07
Au (25nm)	~24	77 +/- 7	0.73	69.8	6.11	3.14

It has been observed that plasmonic nanostructures can enhance light coupling into a device over a broad range of light incident angles and wavelengths.[48] This is an obvious advantage for PV devices to help improve PCE by harvesting more diffuse light and possibly eliminating the need for expensive solar-tracking systems. We tested the performance of inverted devices with ~48 nm ZnO ETLs on ITO and Cr/Au nanostructured electrodes with the incident light angle varied from 0° to 60°. The photocurrent ratio (i.e. ratio of J_{SC} at an angle to the J_{SC} at 0° or normal to device surface) at various incident angles for these devices is shown in Figure 4-25. The photocurrent ratios for both types of devices drops below ~90% past a 30° incident angle to 47% and 45% for ITO and Cr/Au, respectively, at 60°. Both devices retain V_{OC} and FF over the various incident angles but show very similar decreases in J_{SC} as shown in Table 4-6. The lack of any observed absorption enhancement at different angles of incidence for the Cr/Au nanostructures is possibly due, in part, to the presence of the 2 nm thick Cr layer. Simulation has shown that this layer dampens the plasmonic absorption which creates the strong fields associated with SPPs that couple to light at various angles. Improvements in Au-only nanostructure fabrication are on-going and the angular dependence of these nanostructures requires further investigation.

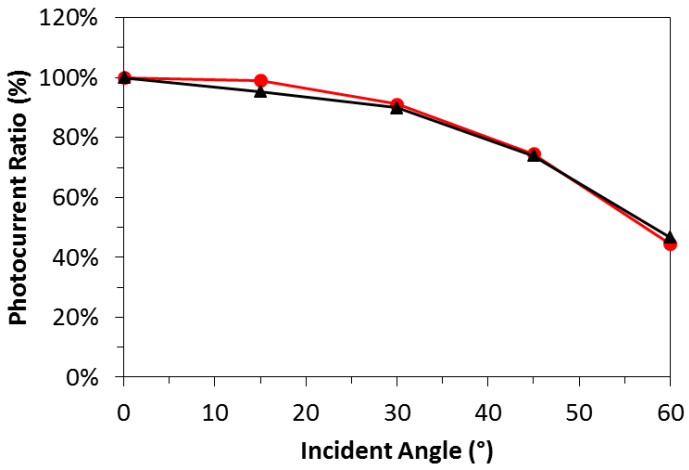

Figure 4-25. Photocurrent ratio versus incident light angle for inverted devices on ITO (black) and Cr/Au nanostructured electrodes (red).

Table 4-6. The performance parameters corresponding to devices tested under varied light incident angle.

Substrate	Angle of Incidence	V_{OC} (V)	FF (%)	J_{SC} (mA/cm^2)	PCE (%)	J_{SC} Ratio
ITO	0°	0.73	0.69	12.84	6.45	100%
	15°	0.73	0.69	12.25	6.18	95%
	30°	0.73	0.68	11.55	5.73	90%
	45°	0.72	0.69	9.50	4.73	74%
	60°	0.71	0.69	6.00	2.92	47%
Cr/Au	0°	0.70	0.69	6.52	3.14	100%
	15°	0.70	0.68	6.46	3.09	99%
	30°	0.70	0.68	5.95	2.83	91%
	45°	0.69	0.68	4.87	2.31	75%
	60°	0.68	0.66	2.91	1.29	45%

4.3.4. Plasmonic Nanostructured Electrodes Deployed in OPVs on Flexible Substrates

Compatibility with flexible substrates is a big advantage of OPVs as high through-put R2R processes require flexibility and devices made on these materials bring the possibility of unique and widespread usage cases. As mentioned, replacing ITO as a transparent electrode is an important requirement for these devices to be produced on a large scale and plasmonic electrodes are a prime candidate for replacement as they are mechanically robust which is essential for flexible solar cells.

Before making flexible devices with plasmonic electrodes, we fabricated PET/ITO based devices to optimize our inverted structure with this new substrate. We typically use the sol gel method to deposit high quality ZnO electron transport layers. However, the sol gel method uses a high baking temperature of 200˚C which will warp and damage the PET/ITO substrates. Alternate methods for making ZnO films include using pre-synthesized ZnO nanoparticles (NPs) which require lower baking temperatures.

We compared devices with glass and PET substrates and also with different types of ZnO NPs. ZnO NPs are commercially available and can be an easy and relatively cheap option for making ZnO films. We deposited ZnO NPs from Sigma Aldrich and baked the films at 140˚C which worked reasonably well with the PET substrates. These NPs have a silane-based ligand and are dispersed in water requiring a baking step for sufficient drying. We also synthesized ZnO NPs in-house which have a much smaller –OH group ligand and are dispersed in a mixture of n-butanol, methanol and chloroform according to procedures in the literature.[91] The mixture of solvents for these NPs dries very quickly while spin coating and a baking step is not required which is advantageous. These ZnO NP films are very stable and can be formed by spin coating in a layer-by-layer fashion while the purchased NPs can be rinsed off with water. Also, it is

expected that these in-house synthesized, bake-free NPs will form higher quality films with a smoother surface and lower sheet resistance brought about by less insulating ligands.

We compared devices using both types of ZnO films on glass and PET to find an optimal device design for use with plasmonic electrodes. Figure 4-26(a) and (b) show some photos of typical devices on PET and the J-V curves for devices using these different NP films on glass (dotted lines) versus PET (solid lines), respectively. The black lines in Fig. 4-26(b) correspond to devices using the ZnO NPs purchased from Sigma-Aldrich and used with both glass and PET substrates. It is interesting to see that the average PCE of the PET device at 6.00% was comparable and even slightly higher than that of the glass device at 5.87% (see Table 4-7). The FF was slightly lower for the PET device as expected because the PET/ITO sheet resistance is lower than that of glass/ITO. The slight increase in PCE stemmed from an increase in J_{SC} for the PET device which may be due to an optical change, however, the standard deviation in the J_{SC} for these devices was relatively high making it comparable to the glass device.

When comparing the glass devices with the purchased ZnO NPs (black dotted line) versus the synthesized NPs (red dotted line), there is a clear increase in both FF and J_{SC} which boosts the average PCE from 5.87% to 6.72%, respectively, with a PCE as high as 7.03%, when using the synthesized NPs. This agrees with our expectation that the synthesized NPs provide a higher quality ZnO film.

However, when comparing these different ZnO NPs on flexible PET/ITO substrates, the FF and J_{SC} dropped lowering the average PCE from 6.00% to 5.36% with the synthesized NPs. This trend is opposite to what was seen with the glass devices leading us to check the active layer optimization with this new ZnO film. Using the purchased ZnO NPs, it was previously

determined that a spin speed around 1400 was optimal. Indeed, the PET devices with synthesized ZnO NPs showed improved FF and J_{SC} with a PCE as high as 6.91% when the active layer was made thicker by lowering the spin speed from 1400 rpm to 1200 rpm (see Fig. 4-26(c) and Table 4-7). Similar to earlier work, the change in ZnO film conditions and morphology requires re-optimization of the active layer. It is also noteworthy that these flexible PET devices showed performance comparable to the glass devices and approached 7% PCE.

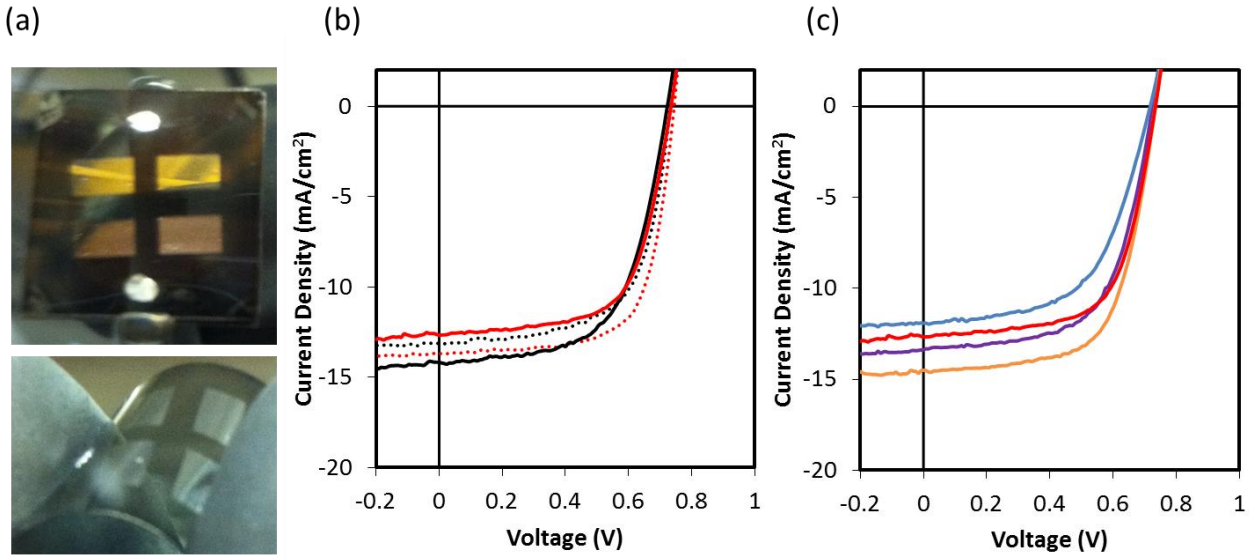

Figure 4-26. (a) Photos of typical inverted devices on flexible PET/ITO substrates. (b) Current-voltage curves of inverted devices on glass/ITO (dotted lines) and on PET/ITO (solid lines) comparing ZnO films from NPs synthesized in-house (red) and purchased from Sigma-Aldrich (black). (c) Current-voltage curves of devices on PET/ITO with in-house synthesized ZnO NPs but with varied active layer spin speeds of 800 rpm (purple), 1000 rpm (blue), 1200 rpm (orange) and 1400 rpm (red) for re-optimization.

Table 4-7. Performance parameters for inverted devices with varied substrate, ZnO NP film, and active layer spin speed corresponding to the J-V curves shown in Fig. 4-26.

Substrate	ZnO Layer	Active Layer Spin Speed (rpm)	Avg. V_{OC} (V)	Avg. FF (%)	Avg. J_{SC} (mA/cm^2)	Avg. PCE (%)	Max. PCE (%)
Glass/ITO	NP (SA)	1400	0.73 +/- 0.00	62.9 +/- 1.1	12.86 +/- 0.19	5.87 +/- 0.19	6.16
Glass/ITO	NP (Synth)	1400	0.74 +/- 0.00	67.9 +/- 0.6	13.42 +/- 0.27	6.72 +/- 0.16	7.03
PET/ITO	NP (SA)	1400	0.72 +/- 0.00	60.6 +/- 1.0	13.71 +/- 0.79	6.00 +/- 0.30	6.25
PET/ITO	NP (Synth)	800	0.72 +/- 0.01	56.5 +/- 4.7	13.43 +/- 0.58	5.45 +/- 0.70	6.01
PET/ITO	NP (Synth)	1000	0.64 +/- 0.07	44.6 +/- 10.8	12.15 +/- 0.54	3.55 +/- 1.17	4.89
PET/ITO	NP (Synth)	1200	0.73 +/- 0.00	63.2 +/- 1.7	13.98 +/- 0.59	6.45 +/- 0.27	6.91
PET/ITO	NP (Synth)	1400	0.73 +/- 0.01	56.9 +/- 6.4	13.01 +/- 0.42	5.36 +/- 0.50	6.00

The optimized inverted structure using the bake-free synthesized ZnO NPs and the flexible PET substrates was then deployed to make the first ITO-free flexible devices with Cr/Au nanostructured electrodes. The nanostructured electrodes on bare PET were made with the same procedures used for the rigid glass substrates. Figure 4-27(a) and (b) show a photograph of the nanopatterns on PET and the current-voltage curves for the device with the nanostructured electrode (red) versus a control on PET/ITO (black). The PET/Cr/Au nanostructured device shows a PCE of 1.82% which is much lower compared to the control device at 5.93%. Note that even the control device in this experiment did not show peak performance which was due to non-optimal active layer thickness. The primary cause for the lower PCE was a ~67% decrease in J_{SC}. This is most certainly due to lower light transmission because of the nanopatten quality. Similarly to the rigid devices, these nanopatterns on PET have "Au-tops" remaining after the solution lift-off step that block the nanoholes underneath. For the glass substrates, this was remedied by using the peel-off procedure described previously. However, this peel-off process did not work with these PET substrates and a new procedure is being developed. Therefore, the Cr/Au nanostructured electrode shown in Fig. 4-27(a) and the device using this electrode in Fig.

4-27(b) did not have the "Au-tops" removed. Work is ongoing to tailor the fabrication procedure for these PET substrates to make quality flexible nanopatterns. To the best of our knowledge, this is the first report of flexible and ITO-free devices using plasmonic nanostructured electrodes.

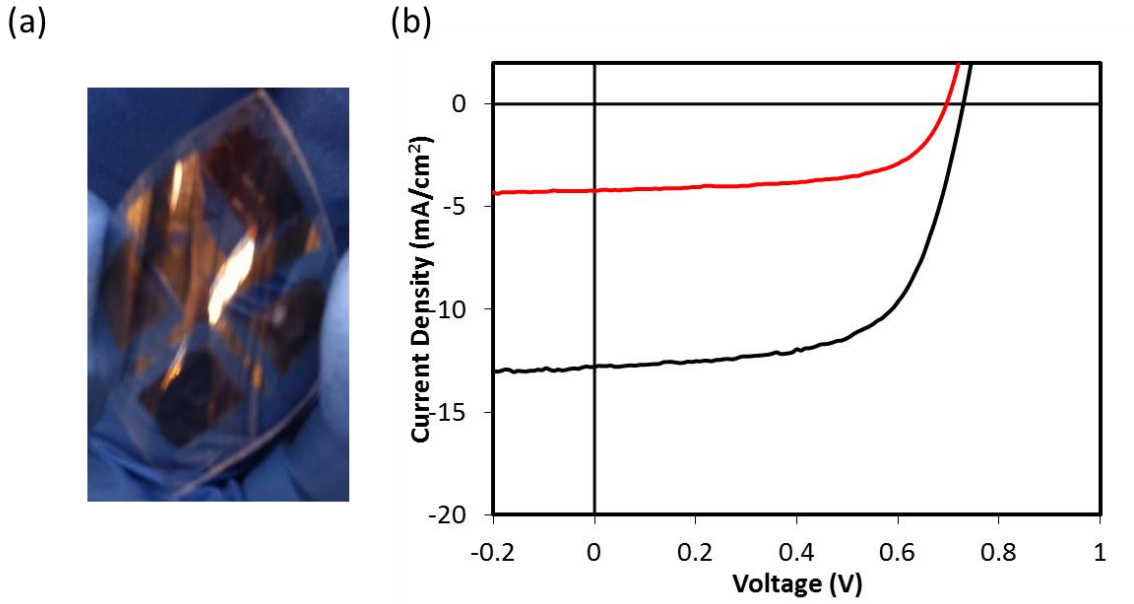

Figure 4-27. (a) Photograph of a bare PET substrate with Cr/Au nanostructures fabricated by NIL. (b) Current-voltage curves of a control device on PET/ITO (black) and an ITO-free device with a Cr/Au nanostructured electrode on PET (red).

Table 4-8. Performance parameters for a control device and a device with a Cr/Au nanostructured electrode on bare PET corresponding to the J-V curves in Fig. 4-27.

Substrate	V_{OC} (V)	FF (%)	J_{SC} (mA/cm^2)	PCE (%)
PET/ITO	0.73	63.6	12.79	5.93
PET/Cr/Au	0.70	62.0	4.22	1.82

OPVs offer compatibility with ultrathin and conformable substrates which can lead to a wide range of potential products and uses for solar energy harvesting devices, such as solar powered clothing and gear for ubiquitous energy generation in remote areas or non-obtrusive,

low-power applications for hidden sensors and the "internet of things". As mentioned, ITO is not suitable for such substrates while the nanostructured electrodes discussed in this work have great potential as an alternative. Figure 4-28 shows the current-voltage curve of an ITO-free inverted device using Cr/Au nanostructured electrodes on a thin (~100 μm) parylene substrate. This substrate is highly flexible and conformable in that it can be wrapped around an object like plastic wrap. The inset to Fig. 4-28 shows the substrate wrapped over the end of a pen. The device shows a relatively low V_{OC}, FF and J_{SC} yielding a PCE of ~1%. However, this performance is in spite of several conditions that have yet to be optimized. The Cr/Au nanopatterns used in these devices have the "Au-tops" covering the nanoholes because the peel-off procedure used for glass substrates is not compatible. These devices also used a new amorphous ZnO sol gel condition with a baking step at 100°C. This new sol gel procedure has not been optimized yet and the ZnO film quality at this condition requires further study. This device also has a thicker ZnO film which should be made thinner as discussed before. Therefore, these conformable devices have several conditions requiring optimization and show promise for increased efficiencies in new conformable OPV devices.

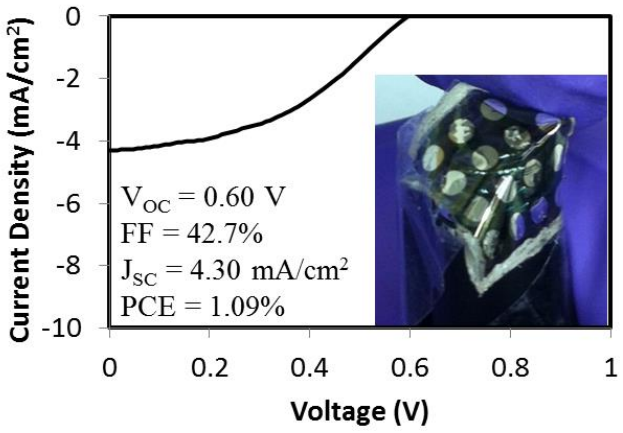

Figure 4-28. Current-voltage curve for an inverted ITO-free device on a conformable Parylene substrate with Cr/Au nanostructured electrodes. The device performance parameters and a photo of the device wrapped around the end of a pen are included in the inset.

4.4 Conclusions

In conclusion, we designed and fabricated plasmonic nanostructures and deployed them as electrodes to replace ITO in OPV devices. The Au-nanohole arrays were designed using FDTD simulations to maximize both active layer light absorption and plasmon-induced electric field enhancements while minimizing device reflectance and showed nanopatterns consisting of 175 nm nanoholes with a 225 nm pitch were optimal. We found that active layer absorption is significantly impacted by the ZnO thickness which affects the optical field distribution inside the resonant cavity formed between the plasmonic nanostructured electrode and the top Ag electrode. High quality Cr/Au nanostructured electrodes were fabricated by nanoimprint lithography and deployed in ITO-free inverted devices on glass. Devices with thinner ~32 nm ZnO ETLs showed a PCE as high as 5.70% and higher J_{SC}'s than devices on thicker ZnO, in agreement with simulation. In addition, as the active layer was made optically thin, ITO-based devices showed a diminished J_{SC} while the resonant cavity effect from plasmonic nanostructured electrodes retained the J_{SC}. Simulation also indicates that the Cr "glue" layer dampens the plasmonic properties of the nanostructures limiting active layer absorption. A new method, i.e. solvent-assisted nanomolding, was used to fabricate Au-only nanostructures eliminating the Cr "glue" layer and is still under development. Initial devices fabricated with these Au-only nanostructures showed PCEs as high as 3.14%, even with nanoholes mostly covered by "Au-tops" and non-optimal layer thicknesses, showing promise for improved ITO-free devices. Nanostructured electrodes were used in ITO-free inverted OPVs on flexible substrates which required different ZnO films with lower temperature treatments. Bake-free, in-house synthesized ZnO NPs made higher quality films than purchased NPs and produced devices on glass/ITO with a PCE as high as 7.03% and on PET/ITO with a PCE as high as 6.91%, which is noteworthy for

a flexible device. Preliminary ITO-free, flexible devices on PET showed a PCE of 1.82%. ITO-free devices were also fabricated on highly flexible, ultrathin and conformable Parylene substrates yielding an initial PCE of over 1%. Further fabrication development is required to improve the large area quality of these nanopatterns on each type of substrate in order to increase light transmission and device performance. To our knowledge, this is the first time nanopatterned plasmonic electrodes have been applied to highly flexible ITO-free OPVs.

CHAPTER 5. CONCLUSIONS AND OUTLOOK

5.1. Conclusions

My work in the field of organic and hybrid PVs has contributed understanding and valuable insights for an understudied semiconductor, i.e. pyrite FeS_2, and a new type of electrode, i.e. plasmonic nanostructures, whose continued development would be highly beneficial for realizing low cost and large area PV production. In addition, my investigation into ZnO nanostructures led to surprising results for a well-known material that are directly applicable to fabricating high efficiency OPVs. Throughout all of these works, I have studied chemical, morphological, optical and electrical properties of these OPV systems that can be used to guide future device design.

I synthesized pyrite FeS_2 NCs with a trioctylphosphine oxide (TOPO) additive because it was hypothesized that TOPO stabilizes the pyrite FeS_2 NC surface in air by passivating both Fe and S sites. TOPO surface ligands may alter the optoelectronic properties of the NCs so I performed cyclic voltammetry (CV) and UV-Vis absorption measurements to determine that the E_g of the pyrite FeS_2 NCs was indeed higher than typically reported. This was primarily due to a lifted conduction band edge, according to the CV measurements. The elevated E_g is likely due to oxygen alloying or the formation of Fe(II)–O with TOPO capping ligands which is supported by the increase in oxidized iron species observed with x-ray photoelectron spectroscopy (XPS) measurements. When deploying these NCs into hybrid OPV devices, I intentionally chose the inverted architecture because sandwiching the active layer between two interfacial layers could reduce current leakage for increased FeS_2 loading. Additionally, the inverted architecture is more stable in air than the conventional structure. Inverted hybrid ternary BHJ solar cells

incorporating pyrite FeS_2 NCs demonstrated enhanced J_{SC} but also increased leakage current. The devices showed good air-stability and ageing the hybrid devices in air for 28 days actually caused significant improvement in FF, V_{OC} and J_{SC}. This improvement likely stems from the formation of silver oxide at the interface between the top electrode and the PEDOT:PSS layer which improves the electronic coherence between these two layers and reduces the leakage current initially caused by the pyrite NC aggregates. The highest PCE of 2.89% was shown by the inverted ternary device with 0.3 wt% FeS_2 NCs after aging in air compared to a maximum PCE of 2.37% exhibited by the control P3HT:PCBM device. The increased photocurrent observed in the inverted ternary devices with low concentrations of pyrite NCs was consistently obtained as the NCs enhanced the molecular packing and morphology of the film increasing charge generation and transport in the organic phases or via pyrite NCs. The photocurrent enhancement and air-stability demonstrated by this inverted design offer a promising architecture for future FeS_2 NC-based devices. Furthermore, the investigation of the NC structure, chemical state and band edges presented provides insight to advance the development of pyrite FeS_2 NCs as a cheap, non-toxic PV material for sustainable energy.

In the previous work, ZnO NP electron transport layers (ETLs) were used. Next, I explored using higher quality sol-gel derived ZnO ETLs in high efficiency inverted OPVs using the PTB7:PC_{71}BM BHJ. Upon varying the film fabrication conditions, we noticed the formation of nano-ridged versus planar ZnO nanostructures and found observations in the literature that these structures significantly impacted the P3HT:PC_{61}BM OPV system. A detailed optical study of devices with these varied ETL nanostructures did not exist so I measured the optical properties of the various ZnO films with spectroscopic ellipsometry and observed that they do change with morphology. Transfer matrix method calculations showed that optical field

distribution changes due to the different ZnO films could only account for small changes in J_{SC} in the range of 0.3-0.5 mA/cm^2. In agreement with the models, devices fabricated with statically baked, planar ZnO films of varied conditions showed consistent J_{SC}'s ranging from 14.17-14.50 mA/cm^2. These devices were insensitive to the varied ZnO thickness and roughness and exhibited consistently high PCEs averaging 7.65-8.01% with a maximum PCE reaching 8.32%. In contrast to the P3HT:PC_{61}BM system, the devices fabricated here also showed no significant difference in performance between those with planar versus nano-ridged ZnO ETLs which also exhibited high PCE's averaging 7.68-7.79% with a maximum PCE reaching 8.14%. The highly efficient photovoltaic function of the PTB7:PC_{71}BM BHJ provides consistently high FF's exceeding 70%, when the active layer thickness is optimized, effectively desensitizing this OPV system to the ZnO conditions probed here. However, this work highlights the importance of maintaining an optimal active layer thickness when changing underlying ETL conditions.

Building on this work studying a highly efficient inverted system, we aimed to develop a new type of electrode for ITO-free OPVs with high PCEs. Replacing ITO is an important problem to solve for low cost, large area OPV production and for novel devices requiring high flexibility and mechanical robustness. Our research group also has expertise in using plasmonic nanostructures in surface-enhanced Raman spectroscopy (SERS) for biological applications which provided valuable perspectives for the design of new plasmonic nanostructured electrodes. I performed FDTD simulations to design nanostructured electrodes that maximize both active layer light absorption and plasmon-induced electric field enhancements while minimizing device reflectance. Nanostructures with 175 nm diameter nanoholes at a 225 nm pitch were found to be optimal and were fabricated by nanoimprint lithography (NIL) which is a method that is compatible with roll-to-roll processing. High quality Au nanostructured electrodes with Cr

"glue" layers were fabricated with NIL and deployed in ITO-free inverted OPVs on glass. ITO electrodes allow light to pass through the active layer once upon initial transmission and again when reflected off of the opaque top electrode. In contrast, plasmonic nanostructured electrodes form a resonant cavity with the top electrode that significantly enhances light trapping inside these devices. We found that active layer absorption is significantly impacted by the ZnO thickness which affects the optical field distribution inside the resonant cavity. Devices with thinner ~32 nm ZnO ETLs showed a PCE as high as 5.70% and higher J_{SC}'s than devices on thicker ZnO, in agreement with simulation. In addition, as the active layer was made optically thin, ITO-based devices showed a diminished J_{SC} while the resonant cavity effect from plasmonic nanostructured electrodes retained the J_{SC}.

Simulation also indicates that the Cr "glue" layer dampens the plasmonic properties of the nanostructures limiting active layer absorption. Thus, I investigated various new nanofabrication methods, such as microcontact printing, nanotransfer printing and solvent-assisted nanomolding (SAN) to fabricate Au-only nanostructures eliminating the Cr "glue" layer. These nanofabrication techniques are compatible with large area, roll-to-roll production and may offer several advantages over NIL for scale-up. Initial devices fabricated with these Au-only nanostructures showed PCEs as high as 3.14%, even with nanoholes mostly covered by "Au-tops" and non-optimal layer thicknesses, showing promise for improved ITO-free devices. This fabrication method requires further development to remove these "Au-tops" and allow these ITO-free devices to reach peak performance.

I also fabricated nanostructured electrodes on several different substrates for flexible ITO-free OPVs. These flexible substrates are not compatible with high temperature processes so I synthesized ZnO NPs that require no baking and optimized them on PET/ITO devices to

achieve a PCE as high as 6.91%, which is noteworthy for a flexible device. Preliminary ITO-free, flexible devices on bare PET showed a PCE of 1.82% and those on novel, highly flexible, ultrathin and conformable Parylene substrates yielded an initial PCE of over 1%. These results show promise with further customization of the nanofabrication techniques to achieve high quality nanopatterns on new flexible substrates. In addition, these new substrates require updated simulation work to tune the optical fields. To our knowledge, this is the first time nanopatterned plasmonic electrodes have been applied to highly flexible ITO-free OPVs.

5.2. Outlook

My studies exploring a new semiconductor and novel device electrodes contribute to the broader field of identifying cheap, abundant and non-toxic materials and new device components to develop the potential of PVs as a renewable and ubiquitous energy source. Substantial progress in OPV device performance via materials, interface and device engineering has led to PCEs exceeding 10%. Maximizing efficiency while minimizing cost are the key components to commercializing solar energy technologies, especially for utility scale power generation. While the efficiencies of OPVs are lower than conventional PV technologies, the solution processability and compatibility with large-area printing processes offer potentially lower cost per kilowatt-hour of energy produced.

An almost endless number of molecular and polymeric material combinations will continue leading to new organic and hybrid semiconductors pushing PCEs even higher. However, challenges other than low efficiencies must be overcome to reach large scale viability. Organic active layers are often sensitive to ambient conditions causing short device lifetimes. Existing commercial encapsulants can prolong lifetimes to 2-3 years but significant strides in materials stability are required to improve them up to 20 years, i.e. a typical PV manufacturers'

warranty. Organic semiconductors are still primarily produced in low-volume and thus command high prices. Production of these materials can be scaled up but will require solving challenges such as quality control and developing green chemistries to eliminate industrial scale use of toxic solvents and reagents.

Despite these challenges, OPVs can enable new niche markets where conventional technologies cannot go. Highly flexible and lightweight OPVs enable the possibility of conformable and mobile ubiquitous power generation from curved and wrinkled surfaces, such as textiles and ultrathin plastic films or wraps. An excellent form factor and relatively good performance under indoor lighting conditions could be especially useful for lower power applications to replace batteries in applications like the "internet of things" that rely on ultra-low power wireless, sensors and beacons. At the 2015 IDTechEx Printed Elecronics Conference, potential markets for OPV were highlighted including advertising, automotive, apparel, building integrated PV and off-grid applications for the developing world. Even in the face of many obstacles, OPV-based companies are forming and a diverse range of exciting applications are eager to take advantage of OPV technologies.

REFERENCES

1. Administration, U. S. E. I., INTERNATIONAL ENERGY OUTLOOK 2013. 2013.

2. Agency, I. E., Energy Technology Perspectives 2014. 2014.

3. Morton, O., Solar energy: A new day dawning?: Silicon Valley sunrise. *Nature* **2006,** *443* (7107), 19-22.

4. U.S. Department of Energy - Sunshot Initiative.

5. Nelson, J., *The Physics of Solar Cells*. Imperial College Press: 2003; p 363.

6. Wu, C.; Murata, H., Thinking small for solar. *Mrs Bulletin* **2012,** *37* (3), 194-195.

7. Li, G.; Zhu, R.; Yang, Y., Polymer solar cells. *Nat. Photonics* **2012,** *6* (3), 153-161.

8. Gan, Q. Q.; Bartoli, F. J.; Kafafi, Z. H., Plasmonic-Enhanced Organic Photovoltaics: Breaking the 10% Efficiency Barrier. *Adv. Mater.* **2013,** *25* (17), 2385-2396.

9. Nelson, J., Polymer: fullerene bulk heterojunction solar cells. *Materials Today* **2011,** *14* (10), 462-470.

10. Espinosa, N.; Garcia-Valverde, R.; Urbina, A.; Krebs, F. C., A life cycle analysis of polymer solar cell modules prepared using roll-to-roll methods under ambient conditions. *Sol Energ Mat Sol C* **2011,** *95* (5), 1293-1302; Espinosa, N.; Garcia-Valverde, R.; Urbina, A.; Lenzmann, F.; Manceau, M.; Angmo, D.; Krebs, F. C., Life cycle assessment of ITO-free flexible polymer solar cells prepared by roll-to-roll coating and printing. *Sol Energ Mat Sol C* **2012,** *97*, 3-13.

11. Forrest, S. R., The path to ubiquitous and low-cost organic electronic appliances on plastic. *Nature* **2004,** *428* (6986), 911-918; Gregg, B. A.; Hanna, M. C., Comparing organic to inorganic photovoltaic cells: Theory, experiment, and simulation. *J Appl Phys* **2003,** *93* (6), 3605-3614.

12. Ma, W. L.; Yang, C. Y.; Gong, X.; Lee, K.; Heeger, A. J., Thermally stable, efficient polymer solar cells with nanoscale control of the interpenetrating network morphology. *Advanced Functional Materials* **2005,** *15* (10), 1617-1622.

13. Green, M. A.; Emery, K.; Hishikawa, Y.; Warta, W.; Dunlop, E. D., Solar cell efficiency tables (version 43). *Progress in Photovoltaics* **2014,** *22* (1), 1-9.

14. He, Z. C.; Zhong, C. M.; Su, S. J.; Xu, M.; Wu, H. B.; Cao, Y., Enhanced power-conversion efficiency in polymer solar cells using an inverted device structure. *Nat. Photonics* **2012,** *6* (9), 591-595.

15. Helgesen, M.; Sondergaard, R.; Krebs, F. C., Advanced materials and processes for polymer solar cell devices. *J. Mater. Chem.* **2010,** *20* (1), 36-60.

16. Saunders, B. R., Hybrid polymer/nanoparticle solar cells: Preparation, principles and challenges. *J. Colloid Interface Sci.* **2012,** *369*, 1-15.

17. Saunders, B. R.; Turner, M. L., Nanoparticle-polymer photovoltaic cells. *Advances in Colloid and Interface Science* **2008,** *138* (1), 1-23; Greaney, M. J.; Das, S.; Webber, D. H.; Bradforth, S. E.; Brutchey, R. L., Improving Open Circuit Potential in Hybrid P3HT:CdSe Bulk Heterojunction Solar Cells via Colloidal tert-Butylthiol Ligand Exchange. *Acs Nano* **2012,** *6* (5), 4222-4230; Liao, H. C.; Tsao, C. S.; Lin, T. H.; Jao, M. H.; Chuang, C. M.; Chang, S. Y.; Huang, Y. C.; Shao, Y. T.; Chen, C. Y.; Su, C. J.; Jeng, U. S.; Chen, Y. F.; Su, W. F., Nanoparticle-Tuned Self-Organization of a Bulk Heterojunction Hybrid Solar Cell with Enhanced Performance. *Acs Nano* **2012,** *6* (2), 1657-1666.

18. Sun, B. Q.; Greenham, N. C., Improved effciency of photovoltaics based on CdSe nanorods and poly(3-hexylthiophene) nanofibers. *Physical Chemistry Chemical Physics* **2006,** *8* (30), 3557-3560; Dowland, S.; Lutz, T.; Ward, A.; King, S. P.; Sudlow, A.; Hill, M. S.; Molloy,

K. C.; Haque, S. A., Direct Growth of Metal Sulfide Nanoparticle Networks in Solid-State Polymer Films for Hybrid Inorganic-Organic Solar Cells. *Adv. Mater.* **2011,** *23* (24), 2739-2744.

19. Dayal, S.; Kopidakis, N.; Olson, D. C.; Ginley, D. S.; Rumbles, G., Photovoltaic Devices with a Low Band Gap Polymer and CdSe Nanostructures Exceeding 3% Efficiency. *Nano Letters* **2010,** *10* (1), 239-242.

20. Seo, J.; Cho, M. J.; Lee, D.; Cartwright, A. N.; Prasad, P. N., Efficient Heterojunction Photovoltaic Cell Utilizing Nanocomposites of Lead Sulfide Nanocrystals and a Low-Bandgap Polymer. *Adv. Mater.* **2011,** *23* (34), 3984-+.

21. Wadia, C.; Alivisatos, A. P.; Kammen, D. M., Materials Availability Expands the Opportunity for Large-Scale Photovoltaics Deployment. *Environmental Science & Technology* **2009,** *43* (6), 2072-2077.

22. Ennaoui, A.; Tributsch, H., Iron Sulfide Solar-Cells. *Solar Cells* **1984,** *13* (2), 197-200.

23. Ennaoui, A.; Fiechter, S.; Pettenkofer, C.; Alonsovante, N.; Buker, K.; Bronold, M.; Hopfner, C.; Tributsch, H., IRON DISULFIDE FOR SOLAR-ENERGY CONVERSION. *Sol Energ Mat Sol C* **1993,** *29* (4), 289-370.

24. Hau, S. K.; Yip, H. L.; Baek, N. S.; Zou, J. Y.; O'Malley, K.; Jen, A. K. Y., Air-stable inverted flexible polymer solar cells using zinc oxide nanoparticles as an electron selective layer. *Appl Phys Lett* **2008,** *92* (25).

25. Yang, T. B.; Cai, W. Z.; Qin, D. H.; Wang, E. G.; Lan, L. F.; Gong, X.; Peng, J. B.; Cao, Y., Solution-Processed Zinc Oxide Thin Film as a Buffer Layer for Polymer Solar Cells with an Inverted Device Structure. *Journal of Physical Chemistry C* **2010,** *114* (14), 6849-6853.

26. Sun, Y. M.; Seo, J. H.; Takacs, C. J.; Seifter, J.; Heeger, A. J., Inverted Polymer Solar Cells Integrated with a Low-Temperature-Annealed Sol-Gel-Derived ZnO Film as an Electron Transport Layer. *Advanced Materials* **2011,** *23* (14), 1679-+.

27. Hau, S. K.; O'Malley, K. M.; Cheng, Y. J.; Yip, H. L.; Ma, H.; Jen, A. K. Y., Optimization of Active Layer and Anode Electrode for High-Performance Inverted Bulk-Heterojunction Solar Cells. *IEEE Journal of Selected Topics in Quantum Electronics* **2010,** *16* (6), 1665-1675.

28. Park, H. Y.; Lim, D.; Kim, K. D.; Jang, S. Y., Performance optimization of low-temperature-annealed solution-processable ZnO buffer layers for inverted polymer solar cells. *Journal of Materials Chemistry A* **2013,** *1* (21), 6327-6334.

29. Tan, Z. A.; Zhang, W. Q.; Zhang, Z. G.; Qian, D. P.; Huang, Y.; Hou, J. H.; Li, Y. F., High-Performance Inverted Polymer Solar Cells with Solution-Processed Titanium Chelate as Electron-Collecting Layer on ITO Electrode. *Adv. Mater.* **2012,** *24* (11), 1476-1481.

30. Yoon, S. M.; Lou, S. J.; Loser, S.; Smith, J.; Chen, L. X.; Facchetti, A.; Marks, T. J., Fluorinated Copper Phthalocyanine Nanowires for Enhancing Interfacial Electron Transport in Organic Solar Cells. *Nano Letters* **2012,** *12* (12), 6315-6321.

31. Hau, S. K.; Yip, H. L.; Ma, H.; Jen, A. K. Y., High performance ambient processed inverted polymer solar cells through interfacial modification with a fullerene self-assembled monolayer. *Appl Phys Lett* **2008,** *93* (233304), 233304.

32. Hau, S. K.; Yip, H. L.; Acton, O.; Baek, N. S.; Ma, H.; Jen, A. K. Y., Interfacial modification to improve inverted polymer solar cells. *Journal of Materials Chemistry* **2008,** *18* (42), 5113-5119.

33. Sekine, N.; Chou, C. H.; Kwan, W. L.; Yang, Y., ZnO nano-ridge structure and its application in inverted polymer solar cell. *Organic Electronics* **2009,** *10* (8), 1473-1477.

34. Aprilia, A.; Wulandari, P.; Suendo, V.; Herman; Hidayat, R.; Fujii, A.; Ozaki, M., Influences of dopant concentration in sol-gel derived AZO layer on the performance of P3HT:PCBM based inverted solar cell. *Sol Energ Mat Sol C* **2013,** *111*, 181-188.

35. Park, B.; Shin, J. C.; Huh, Y. H., Interface-engineering additives for inverted BHJ polymer solar cells. *Sol Energ Mat Sol C* **2013,** *110*, 15-23.

36. Hsieh, C. H.; Cheng, Y. J.; Li, P. J.; Chen, C. H.; Dubosc, M.; Liang, R. M.; Hsu, C. S., Highly Efficient and Stable Inverted Polymer Solar Cells Integrated with a Cross-Linked Fullerene Material as an Interlayer. *Journal of the American Chemical Society* **2010,** *132* (13), 4887-4893.

37. Cheng, G.; Tong, W. Y.; Low, K. H.; Che, C. M., Thermal-annealing-free inverted polymer solar cells using ZnO/Cs2CO3 bilayer as electron-selective layer. *Sol Energ Mat Sol C* **2012,** *103*, 164-170.

38. Liang, Y. Y.; Xu, Z.; Xia, J. B.; Tsai, S. T.; Wu, Y.; Li, G.; Ray, C.; Yu, L. P., For the Bright Future-Bulk Heterojunction Polymer Solar Cells with Power Conversion Efficiency of 7.4%. *Adv. Mater.* **2010,** *22* (20), E135-+.

39. Atwater, H. A.; Polman, A., Plasmonics for improved photovoltaic devices. *Nat Mater* **2010,** *9* (3), 205-213.

40. Barnes, W. L.; Dereux, A.; Ebbesen, T. W., Surface plasmon subwavelength optics. *Nature* **2003,** *424* (6950), 824-830.

41. Wang, D. Q.; Yu, X. L.; Yu, Q. M., X-shaped quasi-3D plasmonic nanostructure arrays for enhancing electric field and Raman scattering. *Nanotechnology* **2012,** *23* (40), 9.

42. Stratakis, E.; Kymakis, E., Nanoparticle-based plasmonic organic photovoltaic devices. *Materials Today* **2013,** *16* (4), 133-146; Li, X. H.; Choy, W. C. H.; Lu, H. F.; Sha, W. E. I.; Ho, A. H. P., Efficiency Enhancement of Organic Solar Cells by Using Shape-Dependent Broadband Plasmonic Absorption in Metallic Nanoparticles. *Advanced Functional Materials* **2013,** *23* (21), 2728-2735; Baek, S. W.; Noh, J.; Lee, C. H.; Kim, B.; Seo, M. K.; Lee, J. Y., Plasmonic Forward Scattering Effect in Organic Solar Cells: A Powerful Optical Engineering Method. *Scientific Reports* **2013,** *3*; Baek, S. W.; Park, G.; Noh, J.; Cho, C.; Lee, C. H.; Seo, M. K.; Song, H.; Lee, J. Y., Au@Ag Core-Shell Nanocubes for Efficient Plasmonic Light Scattering Effect in Low Bandgap Organic Solar Cells. *Acs Nano* **2014,** *8* (4), 3302-3312.

43. Lu, L. Y.; Luo, Z. Q.; Xu, T.; Yu, L. P., Cooperative Plasmonic Effect of Ag and Au Nanoparticles on Enhancing Performance of Polymer Solar Cells. *Nano Letters* **2013,** *13* (1), 59-64.

44. You, J. B.; Li, X. H.; Xie, F. X.; Sha, W. E. I.; Kwong, J. H. W.; Li, G.; Choy, W. C. H.; Yang, Y., Surface Plasmon and Scattering-Enhanced Low-Bandgap Polymer Solar Cell by a Metal Grating Back Electrode. *Advanced Energy Materials* **2012,** *2* (10), 1203-1207.

45. Li, X. H.; Choy, W. C. H.; Huo, L. J.; Xie, F. X.; Sha, W. E. I.; Ding, B. F.; Guo, X.; Li, Y. F.; Hou, J. H.; You, J. B.; Yang, Y., Dual Plasmonic Nanostructures for High Performance Inverted Organic Solar Cells. *Adv. Mater.* **2012,** *24* (22), 3046-3052.

46. Wu, B.; Oo, T. Z.; Li, X. L.; Liu, X. F.; Wu, X. Y.; Yeow, E. K. L.; Fan, H. J.; Mathews, N.; Sum, T. C., Efficiency Enhancement in Bulk-Heterojunction Solar Cells Integrated with Large-Area Ag Nanotriangle Arrays. *Journal of Physical Chemistry C* **2012,** *116* (28), 14820-14825.

47. Devi, B. P.; Wu, K. C.; Pei, Z., Gold nanomesh induced surface plasmon for photocurrent enhancement in a polymer solar cell. *Sol Energ Mat Sol C* **2011,** *95* (8), 2102-2106.

48. Chou, S. Y.; Ding, W., Ultrathin, high-efficiency, broad-band, omni-acceptance, organic solar cells enhanced by plasmonic cavity with subwavelength hole array. *Optics Express* **2013,** *21* (1), A60-A76.

49. Buker, K.; Alonsovante, N.; Tributsch, H., PHOTOVOLTAIC OUTPUT LIMITATION OF N-FES2 (PYRITE) SCHOTTKY BARRIERS - A TEMPERATURE-DEPENDENT CHARACTERIZATION. *J Appl Phys* **1992,** *72* (12), 5721-5728.

50. Lin, Y. Y.; Wang, D. Y.; Yen, H. C.; Chen, H. L.; Chen, C. C.; Chen, C. M.; Tang, C. Y.; Chen, C. W., Extended red light harvesting in a poly(3-hexylthiophene)/iron disulfide nanocrystal hybrid solar cell. *Nanotechnology* **2009,** *20* (40).

51. Puthussery, J.; Seefeld, S.; Berry, N.; Gibbs, M.; Law, M., Colloidal Iron Pyrite (FeS(2)) Nanocrystal Inks for Thin-Film Photovoltaics. *Journal of the American Chemical Society* **2011,** *133* (4), 716-719.

52. Lin, C. W.; Wang, D. Y.; Wang, Y. T.; Chen, C. C.; Yang, Y. J.; Chen, Y. F., Increased photocurrent in bulk-heterojunction solar cells mediated by FeS2 nanocrystals. *Sol Energ Mat Sol C* **2011,** *95* (4), 1107-1110.

53. Bi, Y.; Yuan, Y. B.; Exstrom, C. L.; Darveau, S. A.; Huang, J. S., Air Stable, Photosensitive, Phase Pure Iron Pyrite Nanocrystal Thin Films for Photovoltaic Application. *Nano Letters* **2011,** *11* (11), 4953-4957.

54. Wang, D. Y.; Jiang, Y. T.; Lin, C. C.; Li, S. S.; Wang, Y. T.; Chen, C. C.; Chen, C. W., Solution-Processable Pyrite FeS2 Nanocrystals for the Fabrication of Heterojunction Photodiodes with Visible to NIR Photodetection. *Adv. Mater.* **2012,** *24* (25), 3415-3420.

55. Wadia, C.; Wu, Y.; Gul, S.; Volkman, S. K.; Guo, J. H.; Alivisatos, A. P., Surfactant-Assisted Hydrothermal Synthesis of Single phase Pyrite FeS(2) Nanocrystals. *Chemistry of Materials* **2009,** *21* (13), 2568-2570.

56. Yu, L. P.; Lany, S.; Kykyneshi, R.; Jieratum, V.; Ravichandran, R.; Pelatt, B.; Altschul, E.; Platt, H. A. S.; Wager, J. F.; Keszler, D. A.; Zunger, A., Iron Chalcogenide Photovoltaic Absorbers. *Advanced Energy Materials* **2011,** *1* (5), 748-753.

57. Steinhagen, C.; Harvey, T. B.; Stolle, C. J.; Harris, J.; Korgel, B. A., Pyrite Nanocrystal Solar Cells: Promising, or Fool's Gold? *The Journal of Physical Chemistry Letters* **2012,** *3* (17), 2352-2356.

58. Kirkeminde, A.; Scott, R.; Ren, S., All Inorganic Iron Pyrite Nano-Heterojunction Solar Cells. *Nanoscale* **2012**.

59. Hu, J.; Zhang, Y. N.; Law, M.; Wu, R. Q., Increasing the Band Gap of Iron Pyrite by Alloying with Oxygen. *Journal of the American Chemical Society* **2012,** *134* (32), 13216-13219.

60. Castner, D. G.; Hinds, K.; Grainger, D. W., X-ray photoelectron spectroscopy sulfur 2p study of organic thiol and disulfide binding interactions with gold surfaces. *Langmuir* **1996,** *12* (21), 5083-5086.

61. Agrawal, A. K.; Jenekhe, S. A., Electrochemical properties and electronic structures of conjugated polyquinolines and polyanthrazolines. *Chemistry of Materials* **1996,** *8* (2), 579-589.

62. Schaufuss, A. G.; Nesbitt, H. W.; Kartio, I.; Laajalehto, K.; Bancroft, G. M.; Szargan, R., Incipient oxidation of fractured pyrite surfaces in air. *Journal of Electron Spectroscopy and Related Phenomena* **1998,** *96* (1-3), 69-82.

63. Li, W.; Doblinger, M.; Vaneski, A.; Rogach, A. L.; Jackel, F.; Feldmann, J., Pyrite nanocrystals: shape-controlled synthesis and tunable optical properties via reversible self-assembly. *J. Mater. Chem.* **2011,** *21* (44), 17946-17952.

64. Macpherson, H. A.; Stoldt, C. R., Iron Pyrite Nanocubes: Size and Shape Considerations for Photovoltaic Application. *Acs Nano* **2012,** *6* (10), 8940-8949.

65. Yang, L. Q.; Zhou, H. X.; Price, S. C.; You, W., Parallel-like Bulk Heterojunction Polymer Solar Cells. *Journal of the American Chemical Society* **2012,** *134* (12), 5432-5435.

66. Kuo, S. Y.; Chen, W. C.; Cheng, C. P., Investigation of annealing-treatment on the optical and electrical properties of sol-gel-derived zinc oxide thin films. *Superlattices and Microstructures* **2006,** *39* (1-4), 162-170.

67. Ohyama, M.; Kozuka, H.; Yoko, T., Sol-gel preparation of ZnO films with extremely preferred orientation along (002) plane from zinc acetate solution. *Thin Solid Films* **1997,** *306* (1), 78-85.

68. Jagadamma, L. K.; Abdelsamie, M.; El Labban, A.; Aresu, E.; Ndjawa, G. O. N.; Anjum, D. H.; Cha, D.; Beaujuge, P. M.; Amassian, A., Efficient inverted bulk-heterojunction solar cells from low-temperature processing of amorphous ZnO buffer layers. *Journal of Materials Chemistry A* **2014,** *2* (33), 13321-13331.

69. Liang, Z. Q.; Zhang, Q. F.; Wiranwetchayan, O.; Xi, J. T.; Yang, Z.; Park, K.; Li, C. D.; Cao, G. Z., Effects of the Morphology of a ZnO Buffer Layer on the Photovoltaic Performance of Inverted Polymer Solar Cells. *Advanced Functional Materials* **2012,** *22* (10), 2194-2201.

70. Lin, Y. J.; Tsai, C. L., Changes in surface band bending, surface work function, and sheet resistance of undoped ZnO films due to (NH4)(2)S-x treatment. *J Appl Phys* **2006,** *100* (11), 4.

71. Richardson, B. J.; Zhu, L. Z.; Yu, Q. M., Inverted hybrid solar cells based on pyrite FeS2 nanocrystals in P3HT: PCBM with enhanced photocurrent and air-stability. *Sol Energ Mat Sol C* **2013,** *116*, 252-261.

72. Castanedo-Perez, R.; Jimenez-Sandoval, O.; Jimenez-Sandoval, S.; Marquez-Marin, J.; Mendoza-Galvan, A.; Torres-Delgado, G.; Maldonado-Alvarez, A., Influence of annealing temperature on the formation and characteristics of sol-gel prepared ZnO films. *Journal of Vacuum Science & Technology a-Vacuum Surfaces and Films* **1999,** *17* (4), 1811-1816.

73. Thambidurai, M.; Kim, J. Y.; Song, J.; Ko, Y.; Song, H. J.; Kang, C. M.; Muthukumarasamy, N.; Velauthapillai, D.; Lee, C., High performance inverted organic solar cells with solution processed Ga-doped ZnO as an interfacial electron transport layer. *Journal of Materials Chemistry C* **2013,** *1* (48), 8161-8166.

74. Burkhard, G. F.; Hoke, E. T.; McGehee, M. D., Accounting for Interference, Scattering, and Electrode Absorption to Make Accurate Internal Quantum Efficiency Measurements in Organic and Other Thin Solar Cells. *Adv. Mater.* **2010,** *22* (30), 3293-+.

75. Khoshman, J. M.; Kordesch, M. E., Optical constants and band edge of amorphous zinc oxide thin films. *Thin Solid Films* **2007,** *515* (18), 7393-7399.

76. Yoldas, B. E.; Partlow, D. P., FORMATION OF BROAD-BAND ANTIREFLECTIVE COATINGS ON FUSED-SILICA FOR HIGH-POWER LASER APPLICATIONS. *Thin Solid Films* **1985,** *129* (1-2), 1-14.

77. Szarko, J. M.; Rolczynski, B. S.; Lou, S. J.; Xu, T.; Strzalka, J.; Marks, T. J.; Yu, L. P.; Chen, L. X., Photovoltaic Function and Exciton/Charge Transfer Dynamics in a Highly Efficient Semiconducting Copolymer. *Advanced Functional Materials* **2014,** *24* (1), 10-26.

78. Chen, K. S.; Yip, H. L.; Salinas, J. F.; Xu, Y. X.; Chueh, C. C.; Jen, A. K. Y., Strong Photocurrent Enhancements in Highly Efficient Flexible Organic Solar Cells by Adopting a Microcavity Configuration. *Advanced Materials* **2014,** *26* (20), 3349-+.

79. Wu, J. L.; Chen, F. C.; Hsiao, Y. S.; Chien, F. C.; Chen, P. L.; Kuo, C. H.; Huang, M. H.; Hsu, C. S., Surface Plasmonic Effects of Metallic Nanoparticles on the Performance of Polymer Bulk Heterojunction Solar Cells. *Acs Nano* **2011,** *5* (2), 959-967.

80. Wang, D. H.; Park, K. H.; Seo, J. H.; Seifter, J.; Jeon, J. H.; Kim, J. K.; Park, J. H.; Park, O. O.; Heeger, A. J., Enhanced Power Conversion Efficiency in PCDTBT/PC(70)BM Bulk Heterojunction Photovoltaic Devices with Embedded Silver Nanoparticle Clusters. *Advanced Energy Materials* **2011,** *1* (5), 766-770.

81. Kalowekamo, J.; Baker, E., Estimating the manufacturing cost of purely organic solar cells. *Solar Energy* **2009,** *83* (8), 1224-1231.

82. Zou, J.; Li, C.-Z.; Chang, C.-Y.; Yip, H.-L.; Jen, A. K. Y., Interfacial Engineering of Ultrathin Metal Film Transparent Electrode for Flexible Organic Photovoltaic Cells. *Adv. Mater.* **2014,** *26* (22), 3618-3623.

83. Inganas, O., ORGANIC PHOTOVOLTAICS Avoiding indium. *Nat. Photonics* **2011,** *5* (4), 201-202.

84. Guo, F.; Zhu, X. D.; Forberich, K.; Krantz, J.; Stubhan, T.; Salinas, M.; Halik, M.; Spallek, S.; Butz, B.; Spiecker, E.; Ameri, T.; Li, N.; Kubis, P.; Guldi, D. M.; Matt, G. J.; Brabec, C. J., ITO-Free and Fully Solution-Processed Semitransparent Organic Solar Cells with High Fill Factors. *Advanced Energy Materials* **2013,** *3* (8), 1062-1067; Yim, J. H.; Joe, S. Y.; Pang, C.; Lee, K. M.; Jeong, H.; Park, J. Y.; Ahn, Y. H.; de Mello, J. C.; Lee, S., Fully Solution-

Processed Semitransparent Organic Solar Cells with a Silver Nanowire Cathode and a Conducting Polymer Anode. *Acs Nano* **2014,** *8* (3), 2857-2863.

85. Chou, C.-H.; Chen, F.-C., Plasmonic nanostructures for light trapping in organic photovoltaic devices. *Nanoscale* **2014,** *6* (15), 8444-8458.

86. Qin, D.; Xia, Y. N.; Whitesides, G. M., Soft lithography for micro- and nanoscale patterning. *Nature Protocols* **2010,** *5* (3), 491-502.

87. Loo, Y.; Willett, R.; Baldwin, K.; Rogers, J., Interfacial chemistries for nanoscale transfer printing. *Journal of the American Chemical Society* **2002,** *124* (26), 7654-7655.

88. Deng, Y.; Idso, M. N.; Galvan, D. D.; Yu, Q., Optofluidic microsystem with quasi-3 dimensional gold plasmonic nanostructure arrays for online sensitive and reproducible SERS detection. *Analytica Chimica Acta* **2015,** *863*, 41-48.

89. Byun, I.; Coleman, A.; Kim, B., Transfer of thin Au films to polydimethylsiloxane (PDMS) with reliable bonding using (3-mercaptopropyl) trimethoxysilane (MPTMS) as a molecular adhesive. *Journal of Micromechanics and Microengineering* **2013,** *23* (8).

90. Brzoska, J. B.; Benazouz, I.; Rondelez, F., SILANIZATION OF SOLID SUBSTRATES - A STEP TOWARD REPRODUCIBILITY. *Langmuir* **1994,** *10* (11), 4367-4373.

91. Liu, D. Y.; Kelly, T. L., Perovskite solar cells with a planar heterojunction structure prepared using room-temperature solution processing techniques. *Nat. Photonics* **2014,** *8* (2), 133-138.

92. Richardson, B. J.; Wang, X.; Almutairi, A.; Yu, Q., High efficiency PTB7-based inverted organic photovoltaics on nano-ridged and planar zinc oxide electron transport layers. *Journal of Materials Chemistry A* **2015,** *3* (10), 5563-5571.